2mif

SU-SEL-73-014

Low Frequency Gyro-Synchrotron Radio Noise from the Earth's Outer Radiation Belt

DRA

by

Michael S Frankel

May 1973

Scientific Report No. 1

Prepared under

National Aeronautics and Space Administration
Contracts NAS 5-11387 and NAS 5-23205

RADIOSCIENCE LABORATORY

STANFORD ELECTRONICS LABORATORIES

STANFORD UNIVERSITY • STANFORD, CALIFORNIA

(SU-SEL-73-014) LOW FREQUENCY GYRO-SYNCHROTRON RADIO NOISE FROM THE EARTH'S OUTER RADIATION BELT Scientific Report (Stanford Univ.) 168 p HC $10.50 CSCL 03B G3/29 Unclas 15353

N74-14459

SU-SEL-73-014

LOW FREQUENCY GYRO-SYNCHROTRON RADIO NOISE FROM THE EARTH'S OUTER RADIATION BELT

by

Michael S Frankel

May 1973

Scientific Report No. 1

Prepared under

National Aeronautics and Space Administration
Contract Numbers NAS 5-11387 and NAS 5-23205

Radioscience Laboratory
Stanford Electronics Laboratories
Stanford University Stanford, California

ABSTRACT

Electrons spiraling along magnetic field lines emit electromagnetic radiation at radio wavelengths via the cyclotron and synchrotron emission processes. Consequently, with the discovery of the Van Allen radiation belts, the possibility of detecting synchrotron radiation from superthermal electrons trapped in these regions has become an important topic of research. Studies, which to the present have been limited to frequencies above 2 MHz, show that the radio noise from these electrons is not easily detected as it is less than the noise generated by galactic and extragalactic sources.

In this study, the problem of detecting cyclotron and synchrotron noise from these superthermal electrons is analyzed for the frequency range 30 kHz to 300 kHz. Due to the earth's ionosphere, ground based observation of this noise is improbable. Therefore, the calculations are made for an observer in the interplanetary medium. In particular, the location is chosen in the geomagnetic equatorial plane at a geocentric distance of 32 earth radii. This position of the observer allows the theoretical results to be compared directly with data obtained from the Goddard Space Flight Center (GSFC) radio astronomy experiment aboard the IMP-6 spacecraft.

The energy, radiated by the trapped electrons and propagated to 32 earth radii, is calculated using the equation of radiative transfer. To solve this equation, models for the thermal and superthermal electron densities, throughout the earth's magnetosphere, are derived from in situ and indirect measurements made of these particle populations.

 PRECEDING PAGE BLANK NOT FILMED

The analysis shows that appreciable radio noise in the LF range is emitted by electrons in the earth's outer radiation belt. The inner belt does not contribute power at these frequencies since it is located in the plasmasphere, a region of high thermal electron density, which inhibits radiation at these low frequencies. The intensity of the radio noise from the outer radiation belt is positively correlated with K_p (the planetary three-hour-range index). This correlation is due to the enhancement of the stably trapped electrons during periods of sustained geomagnetic activity. For a frequency f in Hz (30 kHz $\leq$ f $\leq$ 150 kHz), the average calculated brightness, I(f), is given by a constant, M, times the frequency raised to the (-a) power, where both M and (a) vary with K_p as follows: $1^- \leq K_p \leq 2$, log (M) = -12.82, a = 1.66; $3 \leq K_p \leq 4$, log (M) = -11.50, a = 1.71; $5 \leq K_p \leq 6^+$, log (M) = -10.13 a = 1.82. The units of I(f) are watts m^{-2} Hz^{-1} $steradian^{-1}$.

These theoretical results were compared with data from the GSFC experiment aboard the IMP-6, which detected radio noise in the LF range emanating from the earth. The predicted increases in M and (a) with K_p were found in the experimental data. Furthermore, the calculated increases in these quantities are within 10% of those seen in the IMP-6 data, and the experimental and theoretical values of (a) are within 9% for each K_p range.

The theoretical model, however, underestimates the noise intensity observed on the IMP-6 by a consistent factor of 5. This factor is felt to be within modeling and experimental errors. Consequently, it is

concluded that detectable cyclotron-synchrotron noise in the LF range is generated by electrons trapped in the earth's outer radiation belt, and the intensity of this noise increases with increasing geomagnetic activity.

Based on this conclusion, three applications of the results of this study are suggested. First, the radio noise can be used to determine the spatially integrated flux spectrum for the electrons trapped in the earth's outer radiation belt. Second, the noise can be used to obtain an estimate of the maximum interplanetary electron density between the observer and the earth. (An example of this application is given in the study.) Finally, the ray path calculations in the analysis show that a radio occultation experiment between two satellites can be used to determine the location of the plasmapause as a function of K_p and/or time.

CONTENTS

		Page
I.	GYRO-SYNCHROTRON RADIATION MODELS	1
	A. Introduction	1
	B. Initial Assumptions	3
	C. An Overall View of the Problem	14
	D. Gyro-Synchrotron Radiation from a Single Electron	18
	1. Radiation from a Superthermal Electron in Free-Space with $\alpha = 90°$	18
	2. Radiation from a Superthermal Electron in Free-Space with $\alpha \neq 90°$	24
	3. Radiation from a Superthermal Electron in an Isotropic, Refractive Medium	29
	4. Radiation from a Superthermal Electron in a Cold, Anisotropic Plasma	37
	E. The Power Spectral Density Emitted from a Single Electron	46
	F. The Gyro-Synchrotron Emission Coefficient from an Ensemble of Superthermal Electrons	50
	G. Absorption Mechanisms and the Absorption Coefficient	52
II.	MAGNETOSPHERIC MODELS AND RAY PATH CALCULATIONS	55
	A. Introduction	55
	B. The Superthermal Electron Population	56
	1. The OGO-5 Electron Spectrometer	57
	2. Differential Electron Flux Spectrums for $1 \leq K_p \leq 2$ in the Geomagnetic Equatorial Plane	58
	3. Differential Electron Flux Spectrums for $3 \leq K_p \leq 4$ in the Geomagnetic Equatorial Plane	64
	4. Differential Electron Flux Spectrums for $5 \leq K_p \leq 6^+$ in the Geomagnetic Equatorial Plane during the Early Recovery Phase of a Geomagnetic Storm	67
	5. Pitch Angle Distributions	70
	C. The Thermal Electron Population	72
	1. Response of the Thermal Plasma at the Geomagnetic Equator to Variations in K_p	74
	D. The Electron Plasma and Gyrofrequencies as a Function of K_p and L in the Geomagnetic Equatorial Plane	76

PRECEDING PAGE BLANK NOT FILMED

Page

E. Extension of the Particle Models to Regions off the Geomagnetic Equator 80

1. Thermal Electron Density in (B, L) Space 80

2. The Energetic Electron Population in (B, L) Space 81

F. Stratification of the Magnetosphere 85

G. The Refractive Indices in (B, L) Space 86

H. Ray Path Calculations 91

III. THEORETICAL CALCULATIONS 99

A. Introduction 99

B. The Emission Coefficient, J(f) 99

C. Path Lengths as a Function of Look Angle, ϵ 101

D. The Absorption Coefficient, K(f) 103

E. Brightness of the Outer Radiation Belt as a Function of K_p 105

F. The Range of Electron Energies and Harmonic Numbers which Contribute Radiation at a Given Observation Frequency 108

G. The Brightness Observed along Ray Paths off the Geomagnetic Equatorial Plane 112

H. The Average Calculated Spectrums of the Radio Noise Generated in the Earth's Outer Radiation Belt 119

IV. EXPERIMENTAL DATA 123

A. The Spacecraft 123

B. The Radio Astronomy Experiment 123

C. Initial Data Reduction 124

D. Correlation between the Radio Noise Generated at the Earth and Geomagnetic Activity 127

E. Determining the Solid Angle Subtended by the Source Observed by the IMP-6 131

V. COMPARISON OF THEORETICAL AND FINAL RESULTS, FINAL CONCLUSIONS, AND APPLICATIONS 137

A. Comparison of Results 137

B. Summary and Conclusion 142

C. Applications 143

ILLUSTRATIONS

Figure		Page
1.1	Segment of the magnetosphere in which low frequency gyro-synchrotron radio noise is generated and propagated	5
1.2	Complex refractive indices for a medium in which $Y < 1$ [Ratcliffe, 1962]	7
1.3	Geometry for the position and velocity of a charged particle spiraling along a static magnetic field line	9
1.4	Geometry for the radiation emitted by the charged particle of Figure 1.3	10
1.5	An example of a ray path in the geomagnetic equatorial plane along which Equation (1.11) is to be calculated	16
1.6	Envelopes of $P_s(f,E,B,\theta)$ versus harmonic number for electrons of various energies when $\theta = 90°$ and $B = 5.36 \times 10^{-3}$ Gauss (i.e., $f_e = 15$ kHz)	21
1.7a-c	$P_s(f,E,B,\theta)$ versus theta for various harmonic numbers and the values of the parameters given in each figure	23
1.8a-c	$P_s(f,E,B,\theta,\alpha)$ versus theta for various harmonic numbers and the values of the parameters given in each figure	26
1.9a-c	$P_s(f,E,B,\theta,\alpha)$ versus theta for various harmonic numbers and the values of the parameters given in each figure	27
1.10	Envelopes of $P_s(f,E,B,\theta,\alpha)$ versus harmonic number	28
1.11a-c	$P_s(f,E,B,\theta,\alpha,n^*)$ versus theta for an electron radiating in an isotropic medium where it was assumed $n^*(f) = 0.7$	31
1.12a-c	$P_s(f,E,B,\theta,\alpha,n^*)$ versus theta for an electron radiating in an isotropic medium where n^* is a function of frequency and $f_p = 15$ kHz	33
1.13	Envelope of the refractive index, n^*, versus harmonic number for various electron energies	35

ILLUSTRATIONS (Cont)

Figure		Page
1.14a-c	$P_s(f, E, B, \theta, \alpha, n^*)$ versus theta for various harmonic numbers and the values of the parameters given in each figure	36
1.15a-f	$P_s(f, E, B, \theta, \alpha, n_\pm)$ versus theta for an electron in an anisotropic medium where f_p = 6 kHz and f_e = 6 kHz	41
1.16a-f	$P_s(f, E, B, \theta, \alpha, n_\pm)$ versus theta for an electron in an anisotropic medium where f_p = 20 kHz and f_e = 20 kHz	43
2.1	Differential electron flux spectrums for particles with $\alpha = 90°$ in the geomagnetic equatorial plane . . .	60
2.2a-b	Differential electron flux spectrums for particles with $\alpha = 90°$ measured near the geomagnetic equatorial plane	61
2.3a-b	Differential electron flux spectrums for particles in the morning magnetosphere during moderate geomagnetic activity	66
2.4	The response of the electron fluxes in the slot region, L = 3.5, to a moderate geomagnetic storm	69
2.5	The response of the electron fluxes in the outer radiation belt, L = 4.5, to a moderate geomagnetic storm	69
2.6	Electron flux pitch angle data taken concurrently with the data given in Figures 2.3a-b	71
2.7	Radiation of frequency less than or equal to f_1 in region one is shielded from the observer by region two where $n_\pm(f \leq f_1) = 0$	73
2.8	Thermal electron density in the geomagnetic equatorial plane as a function of L for three K_p ranges	77
2.9a-c	Electron plasma and gyro frequencies in the geomagnetic equatorial plane as a function of L for three K_p ranges	79
2.10	Extension of the electron fluxes of Figure 2.2a to regions off the geomagnetic equatorial plane	84

ILLUSTRATIONS (Cont)

Figure		Page
2.11a-f	Refractive indices ($n_{\pm}$) versus frequency L, K_p and theta in the geomagnetic equatorial plane . . .	87
2.12	Ray path geometry in the geomagnetic equatorial plane for an observer whose geocentric distance is 32 earth radii (not drawn to scale)	92
2.13	Expanded version of Figure 2.12	92
2.14	Ray paths calculated in the O-A plane (defined in the text) and the geomagnetic equatorial plane for geomagnetically quiet days (drawn to scale)	96
2.15	Ray paths calculated in the O-A plane (defined in the text) and the geomagnetic equatorial plane during sustained geomagnetic activity resulting in $3 \leq K_p \leq 4$ (drawn to scale)	97
2.16	Ray paths calculated in the O-A plane (defined in the text) and the geomagnetic equatorial plane during geomagnetic activity resulting in $5 \leq K_p \leq 6^+$ (drawn to scale)	98
3.1a-c	The emission coefficient J(f) in the geomagnetic equatorial plane as a function of frequency for various L and K_p values	100
3.2	Path lengths in the geomagnetic equatorial plane (within a given L shell) as a function of the observer look angle	102
3.3	The absorption coefficient K(f) in the geomagnetic equatorial plane as a function of L for f = 30 kHz and various K_p values	104
3.4a-c	Brightness observed along ray paths passing through the earth's magnetosphere, in the geomagnetic equatorial plane	106
3.5a-c	Percent of the total emission coefficient J(f) (for given frequencies) as a function of electron energy for various L values	110
3.6a-c	Percent of the total emission coefficient J(f) (for given frequencies) as a function of harmonic number for various L values	111

ILLUSTRATIONS (Cont)

Figure		Page
3.7a-c	Theoretical spectrums for the gyro-synchrotron radio noise generated in the earth's outer radiation belt	120
4.1	Average background radiation observed by the IMP-6 during April-August 1971	126
4.2	Morphology of the geomagnetic storm occurring on 16-18 May 1971	128
4.3a-c	Brightness spectrums for the source located at the Earth	129
4.4a-c	Scatter plot of the brightness of the earth (calculated from IMP-6 under the assumption stated in the caption of Figure 4.3) as a function of the spacecraft geocentric distance	133
4.5a-c	Corrected IMP-6 brightness spectrums (compare to Figures 4.3a-c) when the source solid angle $\Omega_s(f,K_p)$ is accounted for	135
5.1a-c	Average theoretical and experimental spectrums for the radio noise emanating from the earth's outer radiation belt	139
5.2	Correct IMP-6 brightness spectrum for the noise emanating from the earth's outer radiation belt during the main phase of the 16-18 May 1971 geomagnetic storm	144

UNITS

Aside from the exceptions noted here, rationalized MKS units are employed throughout the study. In the field of geomagnetism it is common to refer to the geomagnetic field intensity (H) and flux density (B) in gaussian units of oersteds and gauss, respectively. Consequently, B is expressed in gauss to conform to common usage in the literature. Similarly, in electron physics, electron energies are commonly given in units of electron volts (ev), kilo electron volts (kev = 10^3 ev) and mega electron volts (Mev = 10^6 ev). Thus electron energies are referred to in electron volts rather than in joules. It will also prove convenient to measure large distances in units of earth radii. To make conversions: 1 gauss = 10^{-4} weber/meter^2; 1 electron volt = 1.60×10^{-19} joules; and 1 earth radius = 6.38×10^6 meters. In all formulae MKS units are used unless specifically noted to the contrary.

SYMBOLS

The symbols most frequently used are defined below. Other symbols are defined as they occur in the text.

$A_e(f)$ . . . . effective antenna area as a function of frequency

B . . . . . magnetic flux density

(B, L) . . . . coordinates used in mapping trapped particles

c . . . . . velocity of electromagnetic waves in a vacuum

D_o . . . . . geocentric distance to an observer in the geomagnetic equatorial plane

e . . . . . charge of an electron, 1.6×10^{-9} Coulomb

E . . . . . kinetic energy

E_o . . . . . rest energy of an electron, 5.11×10^5 ev

E_T . . . . . total energy of an electron, $E + E_o$

$\hat{\underline{E}}$ . . . . . electric field vector

f . . . . . electromagnetic wave frequency

f_e . . . . . nonrelativistic electron gyrofrequency, $eB/2\pi m_e$

f_g . . . . . relativistic electron gyrofrequency, f_e/γ

f_i . . . . . nonrelativistic ion gyrofrequency

f_p . . . . . plasma frequency, $(e/2\pi)\ (B_e/\epsilon_o m_e)^{1/2}$

f_u . . . . . upper hybrid frequency, $(f_p^2 + f_e^2)^{1/2}$

H . . . . . magnetic field intensity

I . . . . . brightness, i.e., the flux of energy per unit bandwidth per unit area within a unit solid angle

I(o) . . . . . total brightness at the observation point along a given ray path

$I(\infty)$ . . . . . brightness of the galactic and extragalactic background

I(f) . . . . . brightness as a function of frequency

I_{act}(source) . actual brightness of a given source

PRECEDING PAGE BLANK NOT FILMED

I_m(source) . . measured brightness of a source

J_s . . . . . s^{th} order Bessel function

J'_s . . . . . first derivative of the s^{th} order Bessel function with respect to its argument

$J(\ell)$ . . . . . emission coefficient as a function of path length

$J_p, J_\perp, J_o$ . . . electron flux intensity

$\bar{K}_\pm$ . . . . . wave propagation vector

$K(\ell)$ . . . . . absorption coefficient as a function of path length

K_p . . . . . planetary magnetic three-hour-range index

L_p . . . . . L value of plasmapause in the geomagnetic equatorial plane

L_s . . . . . center of s^{th} L shell in the geomagnetic equatorial plane

m_e . . . . . rest mass of an electron, 9.11×10^{-31} kg

$n_\pm$ . . . . . real part of the complex refractive index

$n_{r_\pm}$ . . . . . ray refractive index

N_e . . . . . thermal electron number density

$N(E,\alpha)$ . . . . superthermal electron number density per unit energy interval per unit pitch angle

$N(E)$ . . . . . superthermal electron number density per unit energy interval

$N_F(E)$ . . . . superthermal electron flux intensity

$P(\ldots)$ . . . . power spectral density, the power radiated into unit solid angle per Hz of bandwidth

$P_s(\ldots)$ . . . spectral envelope, the power radiated into unit solid angle at the s^{th} harmonic

$\hat{r}$ . . . . . position vector

$R_E(x)$ . . . . real part of x

s . . . . . harmonic number

s_{pk} . . . . . harmonic at which maximum radiation occurs

t . . . . . time

T_e . . . . . absolute temperature of electrons

v . . . . . electron velocity

v_1 . . . . . component of electron velocity perpendicular to the local magnetic field direction

v_2 . . . . . component of electron velocity in direction parallel to the local magnetic field direction

v_{ph} . . . . . electromagnetic wave phase velocity in a medium of refractive index n^*, c/n^*

ΔW . . . . . energy lost by an electron in the form of radiation

α . . . . . angle between an electron's instantaneous velocity vector and the local magnetic field direction

β . . . . . velocity ratio, v/c

β_1 . . . . . $v_1/c = v \sin \alpha/c$

β_2 . . . . . $v_2/c = v \cos \alpha/c$

γ . . . . . Lorentz factor, $(E + E_o)/E_o$

ϵ . . . . . observer look angle in the geomagnetic equatorial plane

ϵ_o . . . . . permittivity of free-space, 8.85×10^{-12} farad m^{-1}

$\underline{\underline{\epsilon}}$ . . . . . dielectric tensor

η . . . . . slope of thermal electron density profile

θ . . . . . angle between the ray path and the local magnetic field direction

λ_m . . . . . geomagnetic latitude referred to a centered dipole model

$\mu_\pm$ . . . . . complex refractive index

μ_o . . . . . magnetic permeability of free-space, 1.26×10^{-6} henry m^{-1}

π 3.14159

σ . . . . . observer look angle in the O-A plane

τ . . . . . optical depth

$\tau(\infty)$ . . . . . optical depth from observer to infinity

χ . . . . . Boltzmann's constant, 1.38×10^{-23} joules kelvin^{-1}

ω . . . . . angular wave frequency

ω_c . . . . . angular collision frequency between electrons and hydrogen ions

ω_e . . . . . angular, nonrelativistic electron gyrofrequency, eB/m_e

ω_g . . . . . angular, relativistic electron gyrofrequency, ω_e/γ

Ω . . . . . solid angle

$\Omega_A(f)$ . . . . antenna solid angle as a function of frequency

$\Omega_s(f,K_p)$ . . . source solid angle as a function of frequency and K_p

ACKNOWLEDGMENTS

I would like to express my gratitude to Dr. Allen Peterson under whose guidance and encouragement the work reported here was performed. I also wish to thank Dr. John Vesecky, whose discussions and advice were of great help, and Dr. A. da Rosa and Dr. M. McWhorter for their careful reading of the manuscript.

Among others who have helped, I am grateful to Dr. H. West, who supplied unpublished OGO-5 electron flux data, Dr. T. Croft, who patiently listened by my ideas, Mr. J. Wickett, who assisted with data reduction, and Miss S. Lewis, who proofread the paper.

The work reported here was performed under National Aeronautics and Space Administration contracts NAS 5-11387 and NAS 5-23205. My thanks go to Dr. L. Brown, Dr. J. Fainberg, and Dr. R. G. Stone, all at Goddard Space Flight Center, for their helpful discussions and for supplying data from the GSFC radio astronomy experiment aboard the IMP-6. I would especially like to thank Dr. Stone for the personal interest he has shown in my behalf.

CHAPTER I

GYRO-SYNCHROTRON RADIATION MODELS

A. Introduction

Synchrotron emission from relativistic electrons has been postulated as the mechanism responsible for radio noise detected from stars [Zheleznyakov, 1967; Thorne, 1962], from the planets of our own system [Fung, 1966; Chang and Davis, 1962], and from extragalactic sources [Zheleznyakov, 1967]. The works of Dyce and Nakada [1959] and Vesecky [1967] explored the possibility of detecting synchrotron radiation at frequencies above 1 MHz from electrons trapped in the earth's inner radiation belt. Dyce and Nakada concluded that, for frequencies around 30 MHz, the radiation from these electrons could not be detected at the earth due to interference from cosmic sources whose emissions are one hundred times as strong. Vesecky found that under suitable conditions it might be possible for an observer situated at a geocentric distance of 4 earth radii in the geomagnetic equatorial plane, to detect synchrotron radio noise between 1 MHz and 10 MHz. His study showed that, for frequencies below 1 MHz, the thermal electron population decreased the synchrotron radiation below detection levels, while the power law energy spectrum of the trapped electrons in the inner belt led to a rapid decrease in the energy radiated at frequencies above 10 MHz.

These studies, however, do not consider the possibility of detecting radio noise generated at frequencies below 1 MHz by superthermal electrons trapped in the outer radiation belt. As will be shown in Chapter II, this portion of the trapped energetic electron population

is located in a region, referred to as the plasmatrough, which is characterized by its very tenuous thermal electron population. Due to this low density, ambient plasma, appreciable power can be generated and propagated in the LF range by a combined cyclotron-synchrotron mechanism (henceforth referred to as the gyro-synchrotron process).

Even though radio noise at frequencies below 1 MHz cannot penetrate the ionosphere, and hence is not detectable by ground based stations, there are an increasing number of radio astronomy experiments aboard earth orbiting satellites with the capability of detecting radio emissions down to frequencies of tens of kHz. The analysis to follow is therefore intended to extend the results of previous studies by determining if the radiation from energetic electrons in the outer radiation belt can be detected at frequencies below 300 kHz by these spacecraft. The upper bound of 300 kHz is arbitrarily set as a means of differentiating between the investigations pursued by previous authors and the one presented here.

To put the problem into more definite terms, we shall determine the intensity and spectrum of the noise between 30 kHz and 300 kHz (during both geomagnetically quiet and disturbed times) that could be received by a spacecraft located in the geomagnetic equatorial plane at a geocentric distance of 32 earth radii. The choice of observer location and the lower bound on the frequency range is not arbitrary; it is intended to allow a direct comparison between the theoretical results of this paper and the data collected by the Goddard Space

Flight Center (GSFC) radio astronomy experiments aboard the IMP-6 spacecraft. (Data from this satellite, kindly supplied through Dr. R. G. Stone and Dr. L. Brown of GFSC, are presented and discussed in Chapter IV.) The analysis carried out in this paper is general, however, and can be extended to data obtained by other spacecraft whose orbits and/or radio astronomy experiments are not the same as those of the IMP-6.

B. Initial Assumptions

In this chapter we shall examine in detail the process by which radio frequency electromagnetic waves are radiated by an ensemble of superthermal electrons (immersed in a magnetoactive plasma) via the gyro-synchrotron mechanism. To model this problem in these general terms, however, would prove to be mathematically intractable due to the complicated phenomena related to the generation and propagation of electromagnetic waves in a magnetized plasma composed of thermally excited electrons, ions and neutral particles [see, for example, Truelsen, 1971]. Fortunately, the problem can be simplified on the basis of the lowest frequency monitored by the experiments aboard the IMP-6 spacecraft and the location in the magnetosphere from where the observed radio noise is shown to emanate. These two conditions led to the results listed below, which shall be referred to by number in the subsequent text.

1. We shall prove that the regions in which appreciable noise is generated are located in the magnetosphere at distances greater than 2.1 earth radii (13,440 km) above the earth's surface. At these heights, the magnetoplasma is composed primarily of hydrogen ions (H^+) and electrons [Chapman, 1959], which are assumed to be present in equal concentration to preserve space charge neutrality.

2. As shown in Chapter III, the region of emission not only lies at a distance of at least 13,000 km from the earth, but is also located between $-40^\circ \leq \lambda_m \leq 40^\circ$. (Here λ_m represents geomagnetic latitude referenced to a coordinate system based on a centered dipole approximation to the geomagnetic field.) This segment of the magnetosphere is that which is swept out by the shaded portion of Figure 1.1 when it is rotated 360° about its vertical axis.

The validity of the centered dipole approximation and the assumptions used in obtaining the bounds for the emission region are subjects considered in Chapter II when the magnetospheric model is developed. At this point it should be noted that the maximum electron and ion (nonrelativistic) gyrofrequencies (f_e and f_i) encountered by an electromagnetic wave propagating in this region are 25 kHz and 13.9 Hz respectively. Since the lowest frequency received by the IMP-6 (30 kHz) is many orders of magnitude above f_i, the ions can be assumed stationary and their effect on the generation and propagation of the radio noise can be ignored [Stix, 1962]. The thermal plasma can therefore be considered as composed of only one constituent: electrons.

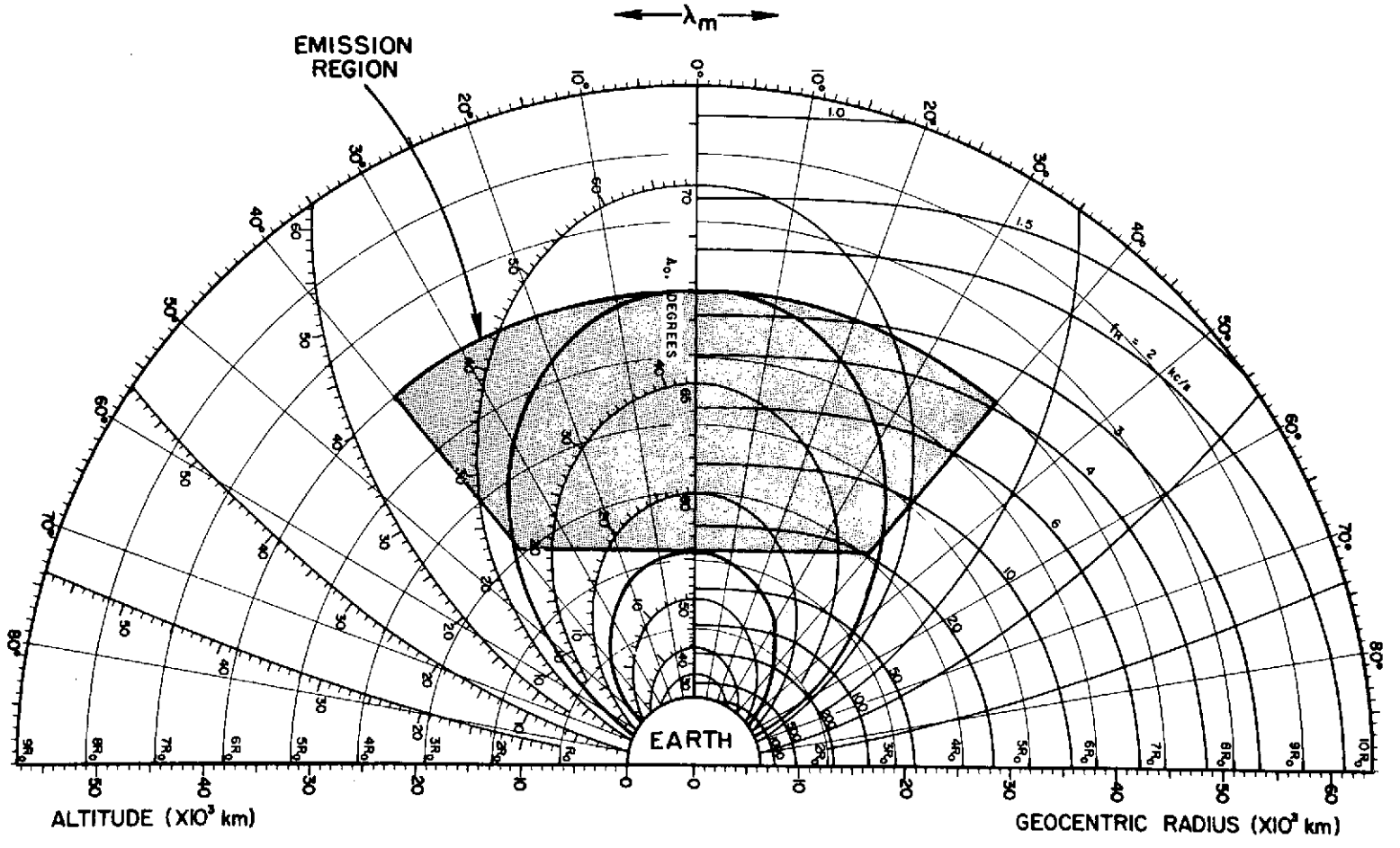

Figure 1.1 SEGMENT OF THE MAGNETOSPHERE IN WHICH LOW FREQUENCY GYROSYNCHROTRON RADIO NOISE IS GENERATED AND PROPAGATED. [Geomagnetic field chart courtesy of Dr. R. A. Helliwell, personal communication.]

3. For 30 kHz to 300 kHz electromagnetic waves propagating in the segment of the magnetosphere described above, the frequency of the radio noise will be above the local upper hybrid frequency (f_u) of the medium. Resonant conditions, where either of the complex refractive indices ($\mu_{\pm}$) tend to infinity, therefore do not occur, and the real part of the indices for the ordinary (μ_+) and extraordinary (μ_-) waves [Ratcliffe's nomenclature, 1962] will be between zero and unity, as shown by Figure 1.2. In this and the subsequent text, the real parts of the complex refractive indices will be referred to simply as the refractive indices, and they are given by

$$n_{\pm} = R_E (\mu_{\pm}) \tag{1.1}$$

$$n_{\pm} = \frac{c}{\omega} R_E(\bar{K}_{\pm}) \tag{1.2}$$

where $\bar{K}_{\pm}$ is the propagation vector for the characteristic waves of the medium and $R_E(x)$ denotes the real part of x.

Furthermore, the energy density of the electromagnetic waves generated in the magnetosphere is small, being less than 10^{-12} watts per square meter, resulting in a magnetic flux density associated with the propagating wave of much smaller magnitude than that which exists in the emission region. These conditions permit the medium to be approximated as linear [Tanenbaum, 1967]. Consequently, the linearized theory of propagation [Ginzburg, 1961] can be used.

4. Stix [1962] shows that a cold-plasma approximation, in conjunction with the linearized theory of propagation, is justified

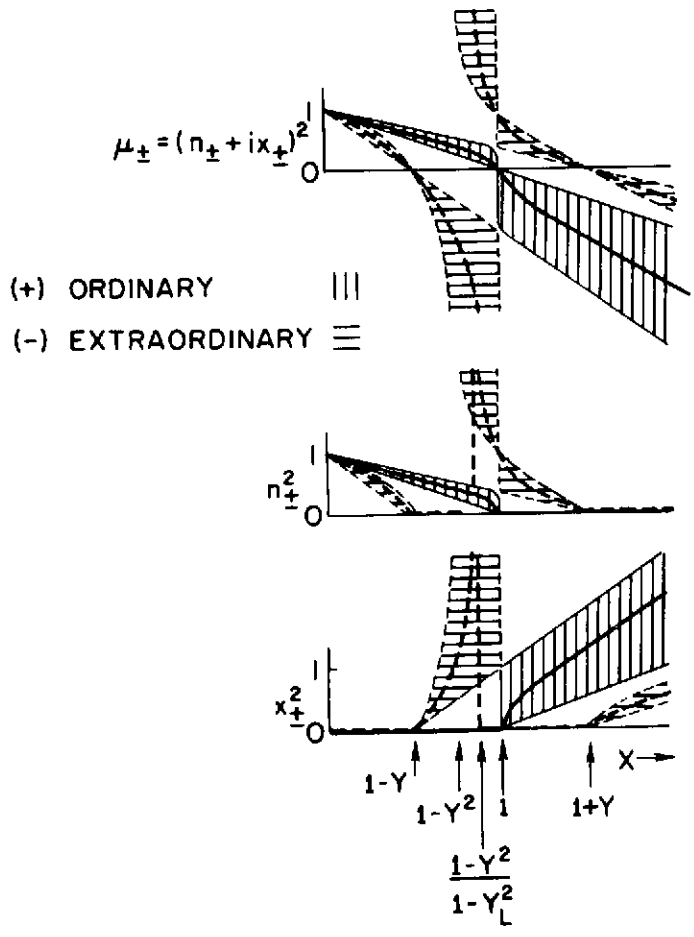

$$\omega_p^2 = \frac{N_e e^2}{\epsilon_o m_e} \qquad \omega_e = \frac{B|e|}{m_e}$$

$$\omega_L = \omega_e \cos\theta \qquad \omega_T = \omega_e \sin\theta$$

$$X = \omega_p^2/\omega^2 \qquad Y = \omega_e/\omega$$

$$Y_L = \omega_L/\omega \qquad Y_T = \omega_T/\omega$$

$$f_u = \omega_u/2\pi = \frac{\sqrt{\omega_p^2 + \omega_e^2}}{2\pi} \qquad f_u \text{ occurs when } X = 1 - Y^2$$

$$\mu_{\pm}^2 = 1 - \frac{2X(1 - X)}{2(1 - X) - Y_T^2 \pm \left[Y_T^4 + 4Y_L^2(1 - X)^2 \right]^{\frac{1}{2}}}$$

Figure 1.2 COMPLEX REFRACTIVE INDICES FOR A MEDIUM IN WHICH $Y < 1$ [From Ratcliffe, 1962].

provided the following equations hold.

$$\left[\frac{\omega + j\omega_e}{|R_E(\bar{K}_z)|}\right]^2 \quad \left[\frac{m_e}{2\chi\ T_e}\right] \gg 1 \qquad j = \ldots,-1,0,1,\ldots \tag{1.3}$$

$$\left[\frac{|R_e(\bar{K}_y)|^2}{\omega_e^{\ 2}\ m_e}\right] \chi T_e \ll 1 \tag{1.4}$$

where

ω = radian frequency of the electromagnetic radiation

χ = Boltzmann's constant

T_e = temperature of the electrons in degrees Kelvin

ω_e = radian gyrofrequency of the electrons

$|R_E(\bar{K}_z)|$ = magnitude of the real part of the wave propagation vector in the z direction

$|R_E(\bar{K}_y)|$ = magnitude of the real part of the wave propagation vector in the y direction

m_e = rest mass of an electron

Using Equation (1.2), an average electron temperature in the magnetosphere of T_e = 1300 K [Bauer, 1965], and the geometry shown in Figures 1.3 and 1.4, the above inequalities can be recast as

$$\left(1 + j\,\frac{\omega_e}{\omega}\right)^2 \gg \frac{n_{\pm}^2 \cos^2\theta\ 2\chi T_e}{m_e c^2} \qquad j = \ldots,\ -1,0,1,\ldots \tag{1.5}$$

and

$$\left(\frac{\omega}{\omega_e}\right)^2 \ll \frac{m_e c^2}{\chi T_e} \quad \frac{1}{n_{\pm}^2 \sin^2\theta} \tag{1.6}$$

Taking the worst case conditions ($n_{\pm} = 1.0$ and $\theta = 90^{\circ}$) for the quantities on the right hand side of these inequalities gives

$$\left(1 + j \frac{\omega_e}{\omega}\right) \gg 6.6 \times 10^{-4} \qquad j = \ldots,-1,0,1,\ldots \tag{1.7}$$

$$\left(\frac{\omega}{\omega_e}\right) \ll 1.51 \times 10^{3} \tag{1.8}$$

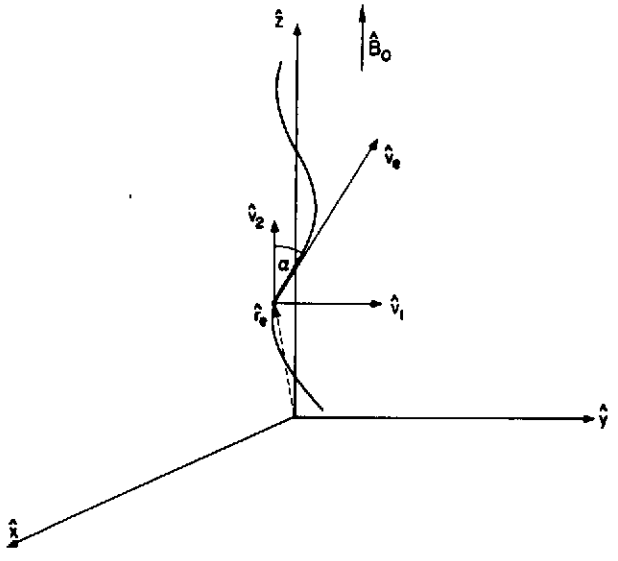

$$\gamma = (1 - \beta^2)^{\frac{1}{2}}$$

$$\beta^2 = (v_1^2 + v_2^2)/c^2$$

$$\beta_1 = v_1/c$$

$$\beta_2 = v_2/c$$

$$\omega_g = \omega_e/\gamma$$

$$r_1 = v_1/\omega_g$$

$$r_x(t) = \gamma r_1 \cos(\omega_g t)$$

$$r_y(t) = \gamma r_1 \sin(\omega_g t)$$

$$r_z(t) = v_2(t)$$

$$\hat{v}_e(t) = d\hat{r}_e(t)/dt$$

Figure 1.3 GEOMETRY FOR THE POSITION AND VELOCITY OF A CHARGED PARTICLE SPIRALING ALONG A STATIC MAGNETIC FIELD LINE.

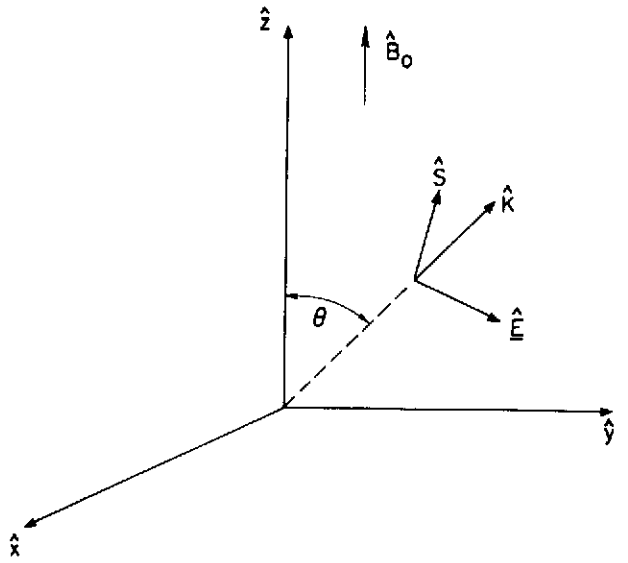

$\hat{S}$ = Poynting vector

$\hat{K}$ = Wave normal direction

$\hat{E}$ = Electric field vector

$\hat{K} = K \sin\theta\ \hat{a}_y + K \cos\theta\ \hat{a}_z$

Figure 1.4 GEOMETRY FOR THE RADIATION EMITTED BY THE CHARGED PARTICLE OF FIGURE 1.3.

In the portion of the magnetosphere which affects the generation and propagation of the radio noise, we find 1 kHz $\leq f_e \leq$ 25 kHz. Thus $1.2 \leq \omega/\omega_e \leq 300$ and the inequalities are always satisfied. Therefore, the cold plasma approximation is valid for this study.

5. For electromagnetic waves of frequency (f) propagating in a plasma, where (f) is greater than the upper hybrid frequency of the thermal plasma, the medium may also be treated as collisionless provided [Ginzburg, 1960]

$$\omega_c^2 \ll (\omega - \omega_e)^2 \qquad (1.9)$$

where

ω_c = radian collision frequency between electrons and hydrogen ions.

The maximum value for ω_c encountered in this study is 10 radians per second [Liehmon, 1965], while $\omega - \omega_e > 3.14 \times 10^3$ radians per second. Therefore, the medium can be taken as collisionless, and the absorption of electromagnetic waves propagating in this medium (due to collisions between electrons and ions) can be ignored. Equivalently, the dielectric tensor ($\underline{\underline{\varepsilon}}$) describing the medium is Hermetian [Yeh and Liu, 1972] and the propagation vector $\underline{\overline{K}}_{\pm}$ is either real or purely imaginary (for real, positive ω) [Bekefi, 1966]. Thus, the wave propagates with no loss of energy due to collisions, or it is evanescent and does not propagate at all.

6. The magnetic permeability of the magnetosphere is taken to be that of free-space (μ_o), which is a good approximation for radio waves propagating in this region of the earth's environment [Yeh and Liu, 1972].

7. Gyro-synchrotron radiation causes an electron gyrating in a magnetic field to lose energy at an average fractional rate per revolution of [Bekefi, 1966]

$$\frac{\Delta W}{E_T} = \frac{e^2 \omega_e}{3\varepsilon_o c} \left[\frac{1}{m_e c^2}\right]\left[\left(\frac{E_T}{m_e c^2}\right)^2 - 1\right] \qquad \beta_2 = 0 \qquad (1.10)$$

where

c = speed of light in free-space

ϵ_o = permittivity of free space

ΔW = energy lost by the particle in the form of radiation

E_T = total energy of the particle (rest mass energy + kinetic energy)

β_2 = velocity component of the particle along the field line as defined in Figure 1.4

The maximum energy, E_T, considered in this study is of the order of 5 Mev, and as stated previously, $\omega_e \leq 15.7 \times 10^4$ rad sec^{-1}. Substituting into Equation (1.10) yields $\Delta W/E_T \approx 6 \times 10^{-16}$. Furthermore, for a fixed E_T, this value decreases as β_2 increases (as will be substantiated later in this chapter). This result implies that the particle energy (as well as β_1 and β_2) is constant over many revolutions; consequently, the gyro-synchrotron model can be used with little error.

8. The lowest frequency received by the IMP-6 radio experiments is 30 kHz, which gives a free-space wavelength for these signals of 10 km. As shown in Chapter II, the region in which the electromagnetic waves propagate is characterized by refractive indices bounded by $0.1 \leq n_{\pm} \leq 1$. Therefore, the wavelength in the medium for the 30 kHz signal is less than or equal to 100 km.

In the models developed in Chapter II for the medium, the magnetosphere is represented by concentric shells whose distances from the earth in the geomagnetic equatorial plane differ by increments of 1000 km. That is, spatial variations in magnetospheric parameters

of importance to this study can be taken as constant over distances less than this value without affecting the final results. Thus, as the scale lengths of variations in these parameters are an order of magnitude or larger than the wavelength of the radiation propagating in these regions, the magnetosphere can be considered as a slowly varying medium. Therefore, the principles of geometric optics can be used to investigate the transfer of radiation from the source regions to the observer [Bekefi, 1966; Ginzburg, 1960].

9. Finally, the time variations associated with the properties of the magnetosphere will generally be much longer than the periods of the signals investigated. As a result, the plasma and the emission processes can be assumed time stationary. This does not imply, however, that gross changes in the magnetosphere due to geomagnetic activity will be excluded from this study, as these changes occur over periods of hours to days.

The above results were derived solely on the basis of the frequency range considered in this study and the location in the magnetosphere from which the major portion of the radiation will be shown to emanate. The importance of this fact is that a much more tractable model for the generation of radio noise can be developed in the next sections.

C. An Overall View of the Problem

Paragraphs eight and nine of the preceding section reduce the problem of calculating the signal generated in the magnetosphere and propagated to the spacecraft to one of radiative transfer in geometric optics. By this analogy, the electromagnetic energy can be envisioned as transported along bundles of curves or rays. For points along a ray of this type (Figure 1.5), a quantity known as brightness (I) satisfies the following differential equation [Bekefi, 1966]

$$\frac{d}{d\ell}\left[\frac{I(\ell)}{n^2_{r_{\pm}}(\ell)}\right] = \frac{J(\ell)}{n^2_{r_{\pm}}(\ell)} - \frac{K(\ell)}{n^2_{r_{\pm}}(\ell)} I(\ell) \qquad (1.11)$$

where

I = brightness of the source at a given point on the ray path (watts m^{-2} Hz^{-1} $ster^{-1}$)

$K(\ell)$ = absorption coefficient as a function of path length (nepers m^{-1})

$J(\ell)$ = emission coefficient as a function of path length (watts m^{-3} Hz^{-1} $ster^{-1}$)

$d\ell$ = element of path length along the ray

$n_{r_{\pm}}$ = ray refractive index which defines the angular variation of the energy flux in an anisotropic medium and is given as a function of $n_{\pm}$ by Equation (1.12) below [Bekefi, 1966].

$$n_{r_{\pm}}^2 = \left| \frac{n_{\pm}^2 \sin\theta \left[1 + \left(\frac{1}{n_{\pm}} \frac{dn_{\pm}}{d\theta} \right)_{\omega}^2 \right]^{\frac{1}{2}}}{\frac{d}{d\theta} \left\{ \frac{\cos\theta + \left(\frac{1}{n_{\pm}} \frac{dn_{\pm}}{d\theta} \right)_{\omega} \sin\theta}{\left[1 + \left(\frac{1}{n_{\pm}} \frac{dn_{\pm}}{d\theta} \right)_{\omega}^2 \right]^{\frac{1}{2}}} \right\}} \right| \qquad (1.12)$$

by defining a quantity called the optical depth (τ) as

$$\tau(\ell_1) = \int_o^{\ell_1} K(\ell)\, d\ell \qquad (1.13)$$

Equation (1.11) can be solved to yield

$$\frac{I(o)}{n_{r_{\pm}}^2(o)} = \frac{I(\infty)\, e^{-\tau(\infty)}}{n_{r_{\pm}}^2(\infty)} + \int_o^{\ell} \frac{e^{-\tau(\ell)} J(\ell)}{n_{r_{\pm}}^2(\ell)}\, d\ell \qquad (1.14)$$

For an observer located in the interplanetary medium and monitoring the frequency range 30 kHz $\leq$ f $\leq$ 300 kHz, we find

$n_{r_{\pm}}^2(o) \approx 1$ $\qquad$ $I(\infty)$ = the brightness of the galactic background

$n_{r_{\pm}}^2(\infty) \approx 1$ $\qquad$ $\tau(\infty) = \int_o^{\infty} K(\ell)\, d\ell$

The observed brightness at the spacecraft is therefore

$$I(o) = I(\text{galactic background})\, e^{-\tau(\infty)} + \int_o^{\ell} \frac{e^{-\tau(\ell)} J(\ell)}{n_{r_{\pm}}^2(\ell)}\, d\ell \qquad (1.15)$$

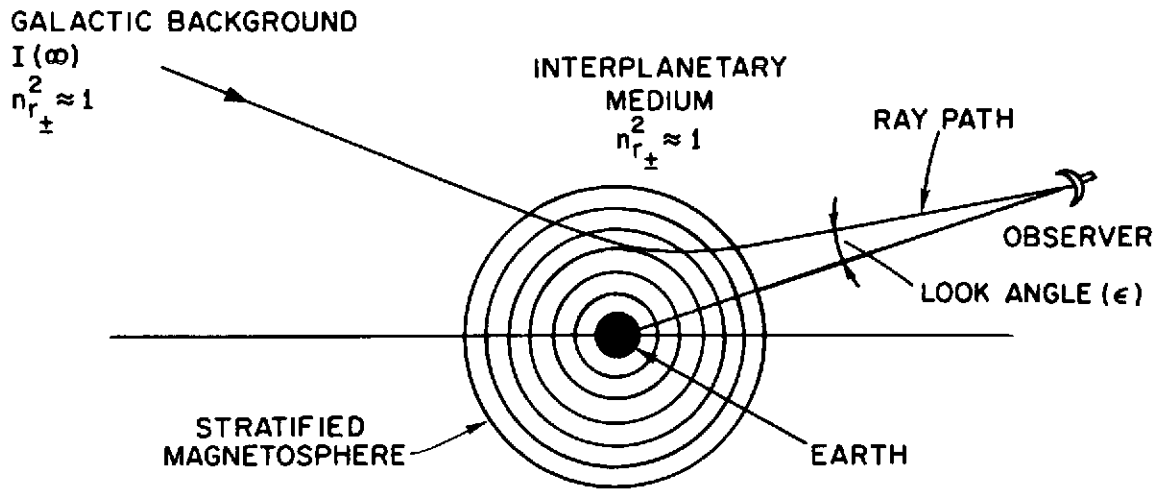

Figure 1.5 AN EXAMPLE OF A RAY PATH IN THE GEOMAGNETIC EQUATORIAL PLANE ALONG WHICH EQUATION (1.11) IS TO BE CALCULATED.

If the brightness due to the galactic background is subtracted from the total observed brightness, the contribution from the magnetosphere is given by

$$I(\text{magnetosphere}) = \int_0^{\ell} \frac{e^{-\tau(\ell)} J(\ell)}{n^2_{r_\pm}(\ell)} d\ell \qquad (1.16)$$

This equation indicates that the brightness along a ray path through the magnetosphere is the sum of the brightness contributions from all interior points of the emitting region along the ray path reduced by their appropriate factors, $e^{-\tau}$, which account for the reabsorption of the radiated energy. The units, steradians, in the definition of brightness and the factor $n^2_{r_\pm}$ in the preceding equations account,

respectively, for the source region subtending a finite solid angle at the point of observation and for the focusing and defocusing of the electromagnetic energy as it propagates through the medium.

To evaluate Equation (1.16) we must determine the emission coefficient $J(\ell)$ and the absorption coefficient $K(\ell)$, both of which are functions of the energetic electron population in the magnetosphere, as well as $n^2_{r_\pm}$ ($n^2_{r_\pm}$, in turn, depends on the thermal plasma). Once these quantities have been determined along all ray paths passing through the emission region and terminating at the observer, an average brightness (I_{av}) for the magnetosphere can be calculated. From I_{av}, the power received in a frequency interval Δf_1 about f_1 can be calculated from

$$\Delta P_r(\Delta f_1) \approx \tfrac{1}{2} \cdot A_e(f_1) \cdot \Omega(f_1) \cdot (\Delta f_1) \cdot I_{av}(f_1) \qquad (1.17)$$

where

$I_{av}(f_1)$ = average brightness of the magnetosphere at frequency f_1 (defined in Section III.G.2)

$A_e(f_1)$ = effective area of the spacecraft receiving antenna at frequency f_1

$\Omega(f_1)$ = solid angle subtended by the emission region at the satellite at frequency f_1

In this equation it is assumed that the receiving antenna is isotropic. When this is not true, the antenna beam pattern and the variation in brightness with observation direction must be considered [Kraus, 1966].

D. Gyro-Synchrotron Radiation from a Single Electron

To obtain a representative value for I_{av}(magnetosphere), it is necessary to understand the properties of the gyro-synchrotron mechanism. To this end, we will develop the more complex case of emission in a magnetoplasma by first considering the more fundamental situation of radio noise generated by electrons spiraling along magnetic field lines in free-space. As a starting point, the model for the particle executing circular motion about the field line will be presented (i.e., α, the particle pitch angle defined in Figure 1.3, will be assumed equal to ninety degrees) and then generalized to the case of helical motion. Finally, radiation in a cold plasma will be discussed as an extension of the simpler free-space results.

1. Radiation from a Superthermal Electron in Free-Space with $\alpha = 90^{o}$

For a moving charge to produce electromagnetic radiation in free-space, it must have a non-zero component of retarded acceleration with respect to the observer. When the acceleration has a component directed opposite to the particle velocity, the particle is slowed, and bremsstrahlung, or braking radiation, is emitted. When the charge is moving in a static magnetic field, the velocity and acceleration are perpendicular, and the resulting radiation is called magnetic bremsstrahlung, or gyro-synchrotron radiation.

For particle energies $E > 100$ kev, the radiation is concentrated in the orbital plane of the electron. Furthermore, the energy is radiated in an increasingly narrow beamwidth as the particle energy increases, and the emission is directed in the particle's instantaneous direction of motion. For example, the total power radiated by an

electron with E $\approx$ 100 kev has a radiation pattern whose beam area is approximately 0.82 steradian, while for E $\cong$ 1000 kev the value is 0.10 steradian. Thus, an observer fixed with respect to the static magnetic field will detect a sequence of pulses separated in time by $T = 1/f_g = \gamma/f_e$ (f_e is the nonrelativistic gyrofrequency of the particle and γ is the Lorentz factor defined as the ratio of the particle's total energy to its rest energy). The length of each pulse is given by $\Delta t = m_e/eB\gamma^2$ [Panofsky and Philips, 1962].

From this discussion, it is evident that the distribution of the radiated power in the frequency domain consists of harmonics of the angular relativistic gyrofrequency (f_g). This observation can be generalized by expressing the power radiated by a single particle, at a frequency equal to the s^{th} harmonic of its gyrofrequency, as a function of five parameters. This function is written as $P_s(f,E,R,\theta,n_{\pm})$ watts $ster^{-1}$ where the variables have the following interpretations:

f, the frequency of observation, where $f = sf_g$

E, the energy of the particle

R, the instantaneous radius of curvature of the particle trajectory. (R is itself a function of the magnetic flux density (B), the velocity of the particle, and the angle (α) which the velocity vector makes with the local magnetic field.)

θ, the angle between the wave propagation vector and the static magnetic field

$n_{\pm}$, the real parts of the complex refractive indices of the medium

Before discussing the effects of these parameters on P_s, it is necessary to obtain the equation for the total power radiated by an electron via the gyro-synchrotron process when $\alpha = 90^o$ and $n_{\pm} = 1.0$. This problem was considered by Panofsky and Philips [1962], who derived the following expression:

$$P_s(f,E,R,\theta) = \frac{e^2 \omega_g^2 \beta^2 s^2}{8\pi^2 \epsilon_o c} \left[J_s'^2 (s\beta \sin\theta) + \frac{\cot^2(\theta)}{\beta^2} J_s^2(s\beta \sin\theta) \right] \tag{1.18}$$

where

e = electronic charge

m_e = rest mass of electron

μ_o = permeability of free-space

ϵ_o = permittivity of free-space

c = velocity of light

v = velocity of particle

B = magnetic flux density

J_s = Bessel function of the first kind of order s

J_s' = derivative of J_s

$f = \omega/2\pi$ = frequency

$f_g = \omega_g/2\pi$ = relativistic gyrofrequency

H = magnetic field intensity

$\beta = v/c$, $\gamma = 1/(1-\beta^2)^{\frac{1}{2}}$

R = radius of circular orbit = $m_e v\gamma/eB$

ω_g = angular gyrofrequency = $v/R = eB/m_e\gamma$

E_T = total energy of particle = $mc^2 = \gamma m_e c^2$

E = kinetic energy = $m_e c^2(\gamma - 1) = E_T - m_e c^2$

ω = angular wave frequency

s = harmonic number

Using the above definitions, Equation (1.18) can be recast as

$$P_s(f,E,B,\theta) = \frac{e^4\beta^2B^2}{8\pi^2\gamma^2m_e^2\epsilon_o c}\left[s^2J_s'^2(s\beta\sin\theta) + \frac{s^2\cot^2\theta}{\beta^2}J_s^2(s\beta\sin\theta)\right] \tag{1.19}$$

(i) To investigate the effect of the particle energy, E, on the emission spectrum, $P_s(f,E,B = \text{constant}, \theta = 90^\circ)$ is plotted as a function of s for different values of E in Figure 1.6. This figure shows that, as E increases, the harmonic number (and therefore frequency) at which peak emission occurs (s_{pk}) also increases. In the energy range considered in this study ($E > 100$ kev), s_{pk} is given approximately by $s_{pk} = [(3/2)\gamma^3]$, where [x] denotes the largest integer less than or equal to x.

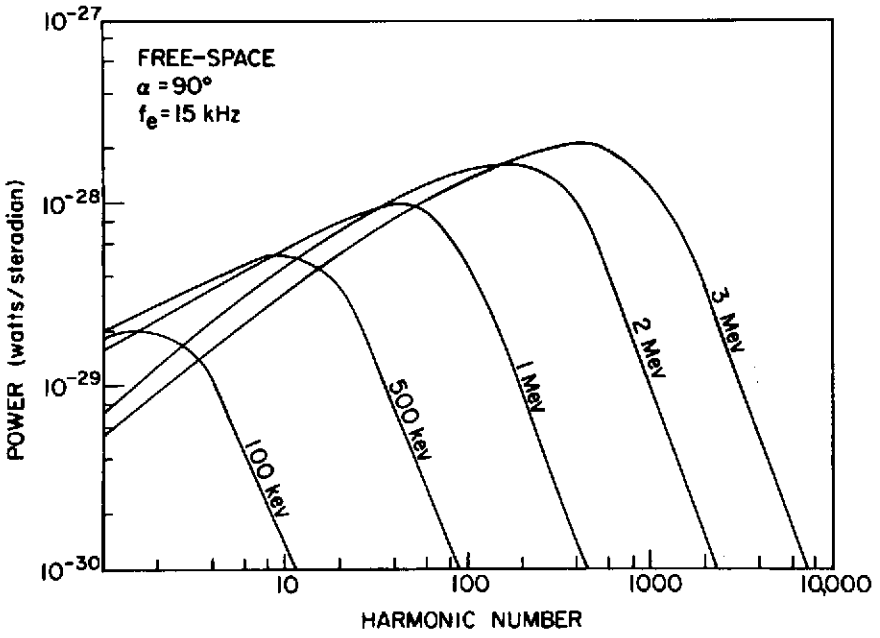

Figure 1.6 ENVELOPES OF $P_s(f,E,B,\theta)$ VERSUS HARMONIC NUMBER FOR ELECTRONS OF VARIOUS ENERGIES WHEN $\theta = 90^\circ$ AND $B = 5.36 \times 10^{-3}$ GAUSS (i.e., f_e = 15 kHz).

(ii) The effect of changes in the magnetic flux density is easily seen from Equation (1.19), which shows that $P_s(f, E = \text{constant}; B, \theta = 90^o) \propto B^2$.

(iii) The radiation pattern for the particle emission is given by the polar plots for $P_s(f, E = 0.1, 0.5, 1.0 \text{ Mev}; B = \text{constant}, \theta)$ in Figures 1.7 a-c. A number of important results should be noticed from these curves. (The emission is taking place in free-space; therefore, all harmonics are generated and propagated. To keep the figures legible, however, all of them were not drawn.)

(a) The power received for $s \gtrsim 3$ and $E \gtrsim 100$ kev is a maximum for $\theta = \alpha = 90^o$.

(b) The beamwidth (defined as the angle between half-power points measured about the direction of maximum emission) decreases as harmonic number increases.

(c) Higher harmonics contribute very little power for directions near or along the magnetic field line. Lower harmonics, however, contribute appreciable energy close to the field lines. In particular, the first harmonic is nearly twice as strong along the field line as compared to $\theta = 90^o$ (see the $E = 100$ kev plots).

(d) There is symmetry with respect to $\theta = 90^o$. (This fact is readily deduced from Equation (1.19).)

(e) The power received at a frequency $f_1 = sf_g$ is strongly dependent on the angle of observation θ.

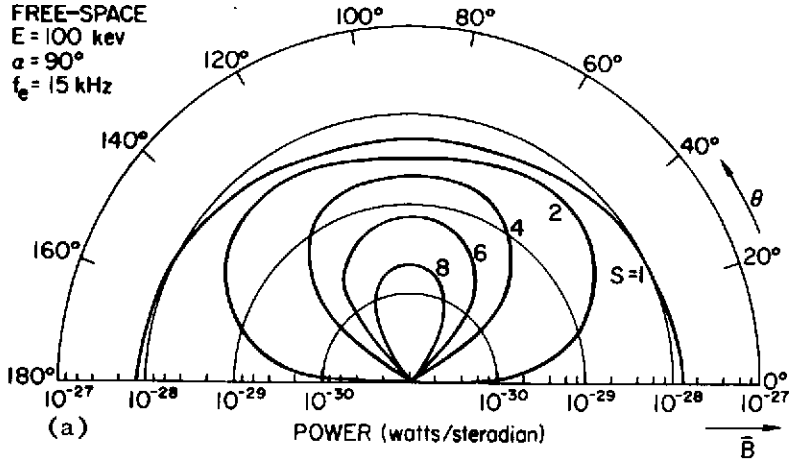

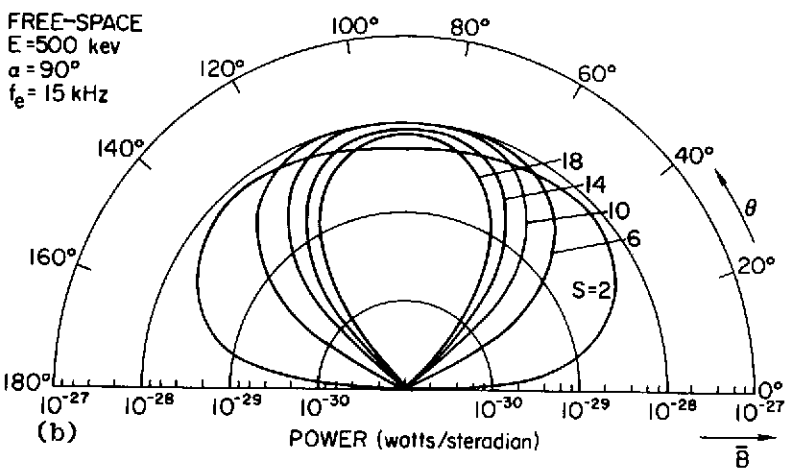

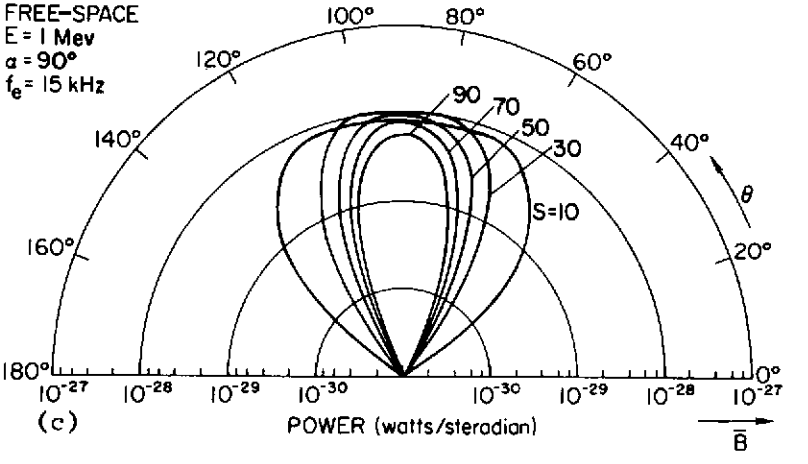

Figure 1.7 a-c $P_s(f,E,B,\theta)$ VERSUS THETA FOR VARIOUS HARMONIC NUMBERS AND THE VALUES OF THE PARAMETERS GIVEN IN EACH FIGURE.

Figures 1.7 a-c and Equation (1.19) represent the total power radiated by the electron, which is defined as the sum of the power radiated into the ordinary and extraordinary modes. These modes of propagation will be defined and discussed in Section I.D.4.

2. Radiation from a Superthermal Electron in Free-Space with $\alpha \neq 90^{o}$

The model presented thus far is the simplest case for which gyro-synchrotron emission can occur, and it has been discussed and applied extensively in the literature [Peterson and Hower, 1966; Hower and Peterson, 1964; Vesecky, 1967]. However, if the particle travels in a helix along the magnetic field line (i.e., $\alpha \neq 90^{o}$ with $n_{\pm} = 1.0$), the model becomes considerably more complex.

For this case, the appropriate equation can be derived by integrating Equation (6.14) of Bekefi's [1966] with respect to radian frequency (ω). The result for the total radiated power per unit solid angle is

$$P_s(f,E,B,\theta,\alpha) =$$

$$\frac{e^4 s^2 \beta_1^2 B^2}{8\pi^2 \epsilon_o c m_e^2 \gamma^2 (1 - \beta_2 \cos\theta)^3} \left[J_s'^2\left(\frac{s\beta_1 \sin\theta}{1-\beta_2\cos\theta}\right) + \left(\frac{\cos\theta - \beta_2}{\beta_1 \sin\theta}\right)^2 J_s^2\left(\frac{s\beta_1 \sin\theta}{1-\beta_2\cos\theta}\right)\right] \tag{1.20}$$

where the frequency of observation (f) is now given by

$$f = sf_g\left[\frac{1}{1 - \beta_2 \cos\theta}\right] \tag{1.21}$$

and

$$\beta_1 = \beta \sin \alpha$$
$$\beta_2 = \beta \cos \alpha \qquad (1.22)$$

The term $(1-\beta_2 \cos \theta)^{-1}$ is due to the Doppler shift occurring as a result of the electron motion with respect to the fixed observer.

Calculations by this author show that the effects of E and B on $P_s(f,E,B,\theta,\alpha)$ satisfy sub-paragraphs b,c,d and e of the preceding section where now $f = sf_g$ is replaced by Equation (1.21). For the present case, however, the maximum radiation for any harmonic and energy is in the direction of the instantaneous orbit of the electron (as shown by Figures 1.8 a-c for $\alpha = 70^\circ$ and Figures 1.9 a-c for $\alpha = 30^\circ$). Furthermore, the symmetry about $\theta = \alpha$ no longer exists, as the power falls off much more rapidly for $\theta < \alpha$ than for $\theta > \alpha$. This effect is a result of the modes of propagation alluded to in the last paragraph of the preceding section. As will be discussed later, the majority of the energy in the "ordinary" mode is generated near $\theta = 90^\circ$ while the energy in the "extraordinary" mode is generated predominantly along the direction $\theta = \alpha$. The sum of the power radiated into both of these modes, therefore, yields the skewed plots shown in these figures.

The curves also indicate that the peak power for a given harmonic decreases as the pitch angle decreases from 90°. This phenomenon is clearly depicted in Figure 1.10, where each curve is plotted for $\theta = \alpha$. Over the energy range 100 kev $\leq E \leq$ 3 Mev, calculations showed that the peak power for a given harmonic was within a factor of one

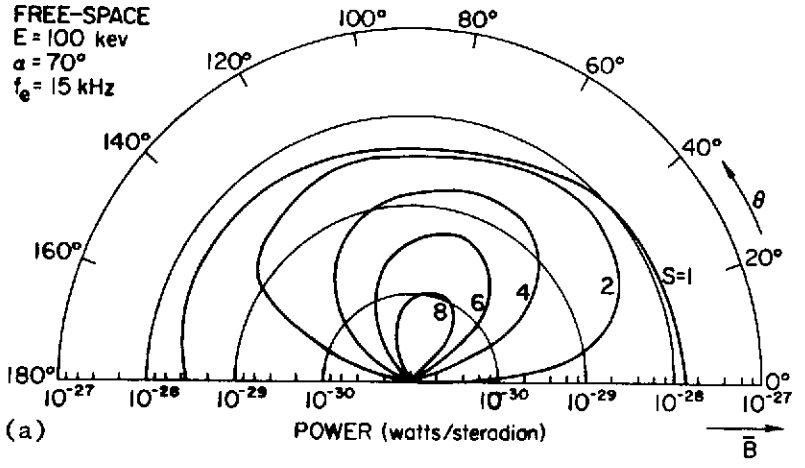

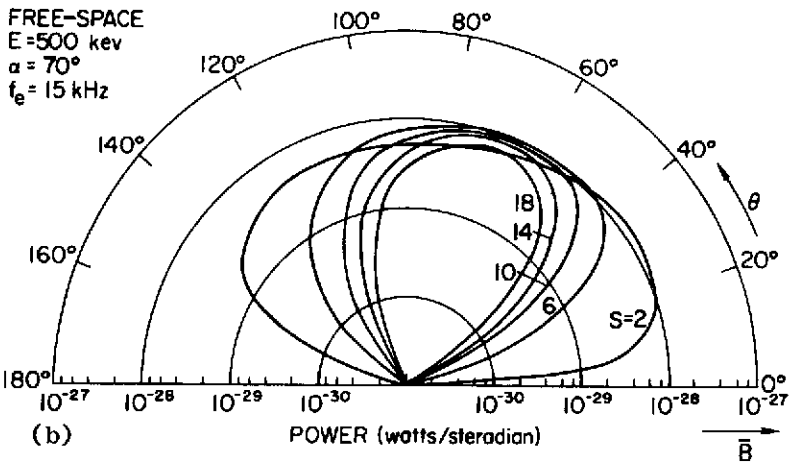

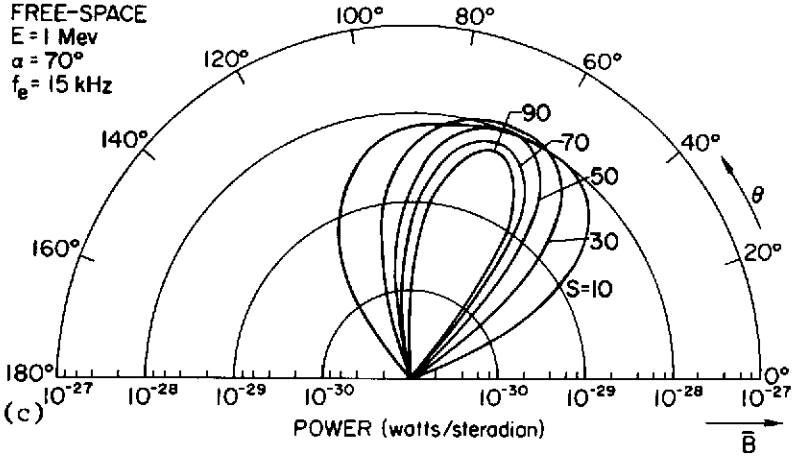

Figure 1.8 a-c $P_s(f,E,B,\theta,\alpha)$ VERSUS THETA FOR VARIOUS HARMONIC NUMBERS AND THE VALUES OF THE PARAMETERS GIVEN IN EACH FIGURE.

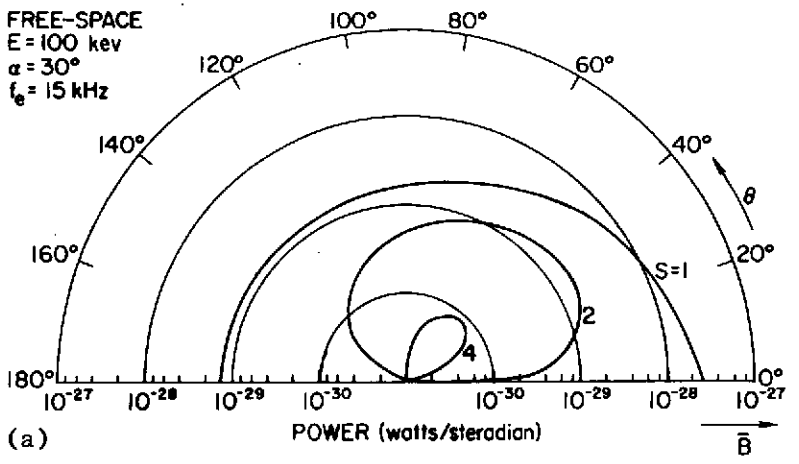

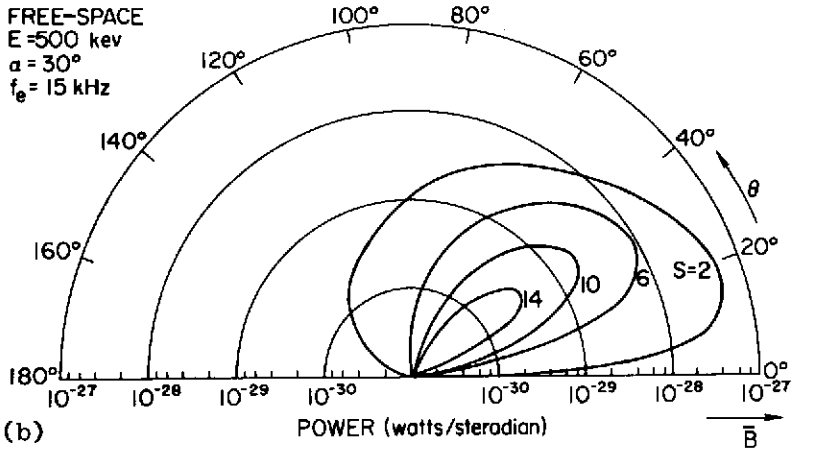

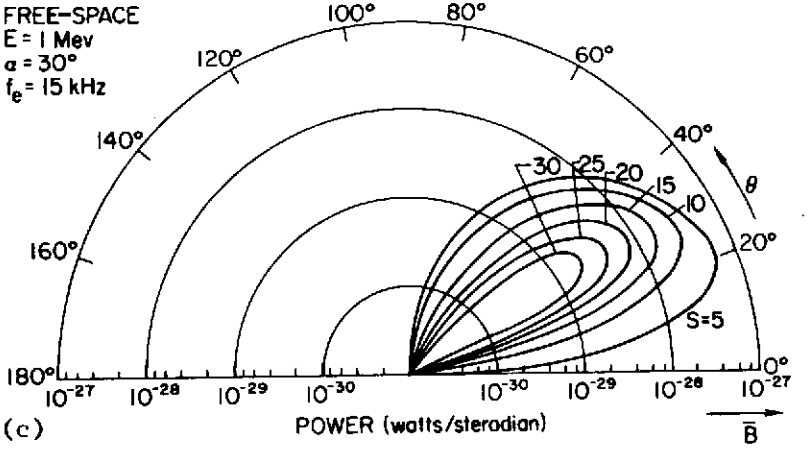

Figure 1.9 a-c $P_s(f,E,B,\theta,\alpha)$ VERSUS THETA FOR VARIOUS HARMONIC NUMBERS AND THE VALUES OF THE PARAMETERS GIVEN IN EACH FIGURE.

half from that at $\alpha = 90^{\circ}$, when $90^{\circ} < \alpha \lesssim 70^{\circ}$. As α becomes less than 70°, the peak power begins to decrease at an increasing rate.

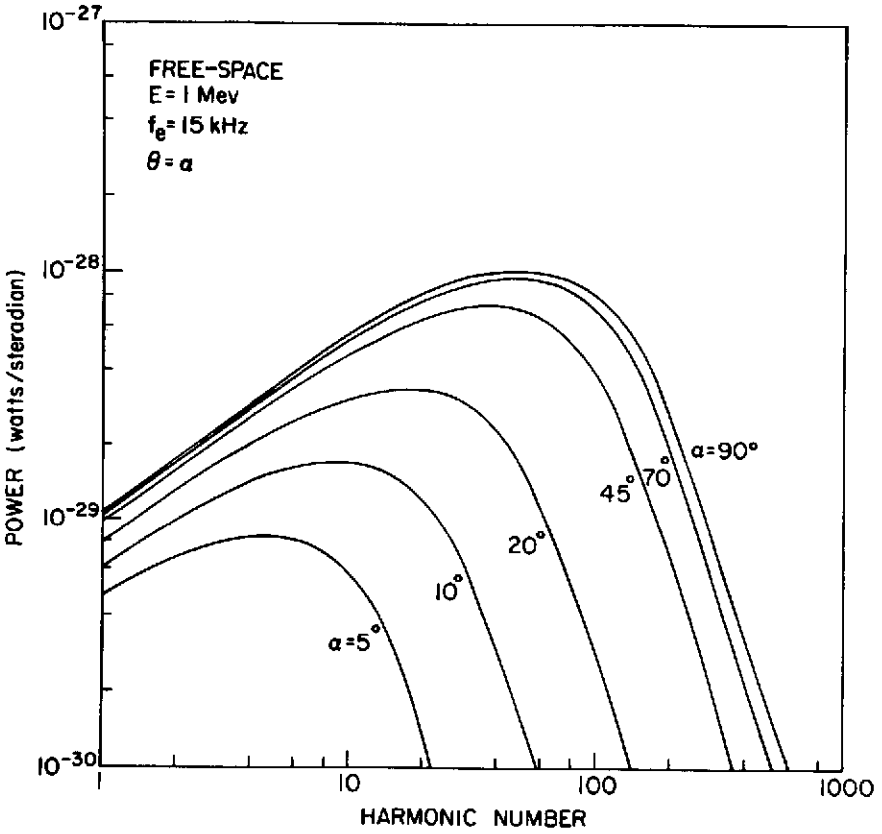

Figure 1.10 ENVELOPES OF $P_s(f,E,B,\theta,\alpha)$ VERSUS HARMONIC NUMBER. EACH CURVE IS OBTAINED FOR THE OBSERVATION DIRECTION COINCIDING WITH THE INSTANTANEOUS ORBITAL PLANE OF THE ELECTRON (i.e., $\theta = \alpha$).

This section has extended the gyro-synchrotron model to include particles whose pitch angles are not equal to ninety degrees, which is the general case applicable to the free-space problem. It remains, however, to investigate how the power spectrum changes when the particle radiates in a medium where the refractive index is no longer equal to unity.

3. Radiation from a Superthermal Electron in an Isotropic, Refractive Medium

Before discussing the final case, we shall consider an isotropic medium composed of a tenuous plasma satisfying the conditions derived in Section I.B (i.e., the magnetic field is assumed weak enough not to affect the propagation of electromagnetic waves yet strong enough to allow gyro-synchrotron radiation to occur). A medium of this nature is described by one refractive index, n^*, for both the ordinary and extraordinary modes of propagation. Under this condition, the power spectrum $P_s(f,E,B,\theta,\alpha,n^*)$ can be obtained by modifying the derivation for $n_{\pm} = 1.0$ in Bekefi [1966]. This modification is based on the fact that the phase velocity of the electromagnetic waves propagating in the plasma is not c (the velocity of light in free-space) but is instead

$$v_{ph} = \frac{c}{n^*} \qquad (1.23)$$

Using this equation in Bekefi's analysis yields

$$P_s(f,E,B,\theta,\alpha,n^*) = \frac{e^4 s^2 B^2 \beta_1^2 n^*}{8\pi^2 \epsilon_o c m_e^2 \gamma^2 (1-n^*\beta_2\cos\theta)^3} \left[J_s'^2\left(\frac{sn^*\beta_1\sin\theta}{1-n^*\beta_2\cos\theta}\right) + \left(\frac{\cos\theta - n^*\beta_2}{n^*\beta_1\sin\theta}\right)^2 J_s^2\left(\frac{sn^*\beta_1\sin\theta}{1-n^*\beta_2\cos\theta}\right)\right] \quad (1.24)$$

where f is now given by

$$f = sf_g\left[\frac{1}{1-n^*\beta_2\cos\theta}\right] \quad (1.25)$$

This formula was evaluated for $n^* = 0.7$ and $\alpha = 90^o$, and the results were plotted in Figures 1.11a-c. These figures do not represent a realistic case as n^* is actually a function of frequency (and thus harmonic number). They do, however, emphasize the relationship between $P_s(f,E,B,\theta,\alpha,n^*)$ and n^*. As seen, for increasing particle energies, the power radiated by a particle is severely decreased in comparison with the n = 1.0 case. This effect is so pronounced that, on a scale consistent with previous figures, only the tenth harmonic for E = 1.0 MeV can be drawn. These figures also show this phenomenon to be greater at higher harmonics, as evidenced by comparing Figures 1.11a-c with Figure 1.7a-c. These same observations are also applicable to pitch angles other than 90^o when n^* is less than unity.

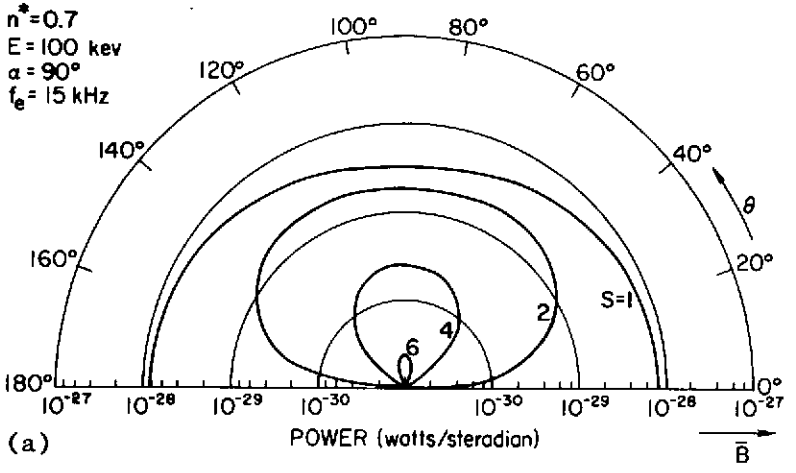

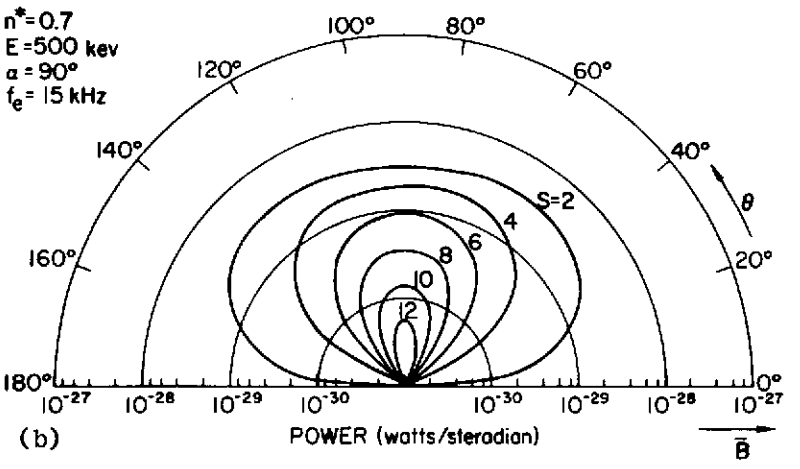

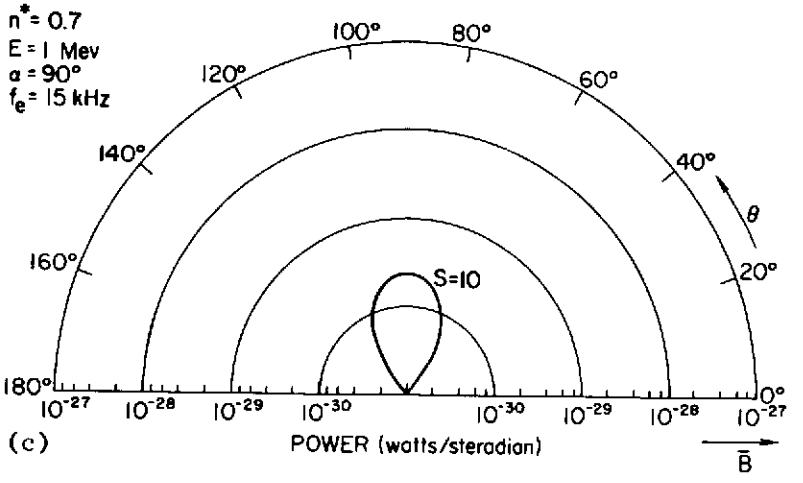

Figure 1.11 a-c $P_s(f,E,B,\theta,\alpha,n^*)$ VERSUS THETA FOR AN ELECTRON RADIATING IN AN ISOTROPIC MEDIUM WHERE IT WAS ASSUMED $n^*(f) = 0.7$.

Even though the above analysis helps to clarify the effects of varying n^* and P_s, it does not represent a physical situation. To understand what actually occurs, consider the emission from a super-thermal electron in a magnetoplasma with a plasma frequency (f_p) of 15 kHz. Since the medium is assumed isotropic (i.e., the effects of the magnetic field are ignored) the refractive index is given by [Tanenbaum, 1967]

$$n^* = \sqrt{1 - \frac{f_p^2}{f^2}} \qquad (1.26)$$

Using this equation for n^* in Formula (1.24), we calculated the curves in Figures 1.12a-c, which show a number of new features.

First, both the power radiated at the lower harmonics and the beamwidth of these harmonics decrease in comparison to the free-space problem. However, as the harmonic number increases, these effects become less evident. This phenomenon was first noticed by Razin [1960] and is easily explained by noting that as the frequency (and hence harmonic number) increases, n^* approaches unity, its value for free-space. Razin has shown that the medium may be treated as free-space provided the frequency of the electromagnetic radiation (f) satisfies the relationship $f \gg 3/2\ f_p^2/f_e$.

Second, a number of the lower harmonics for each energy are no longer emitted. (See Figures 1.12a-c, where the lowest harmonic plotted is the first to be radiated.) As shown, the greater the particle energy the larger the harmonic number which is first

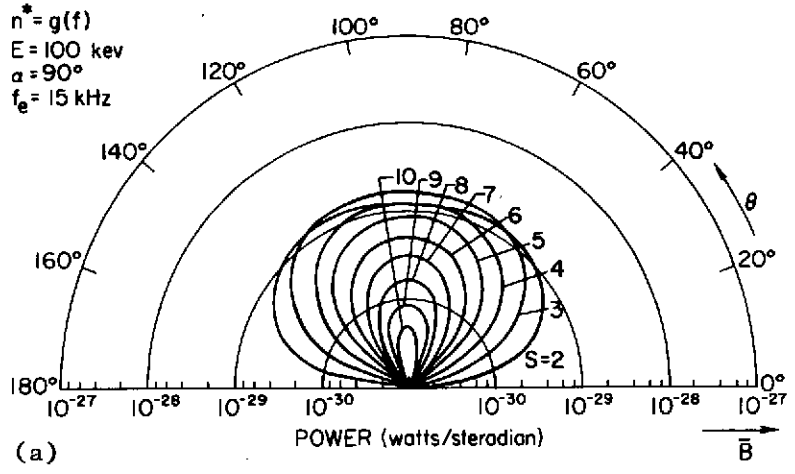

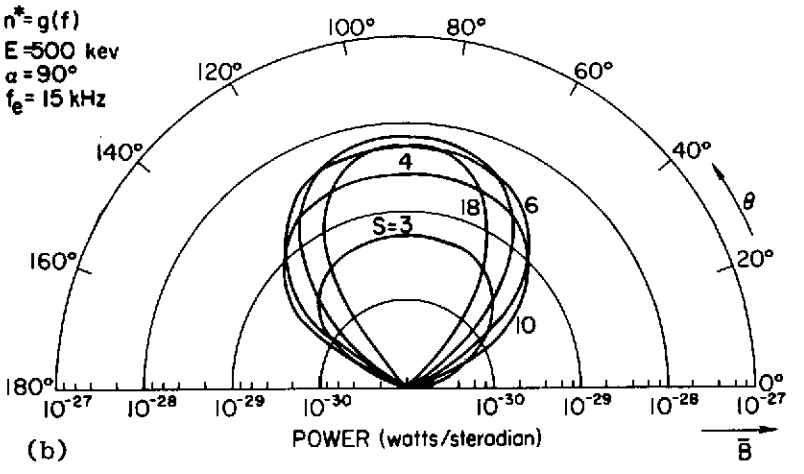

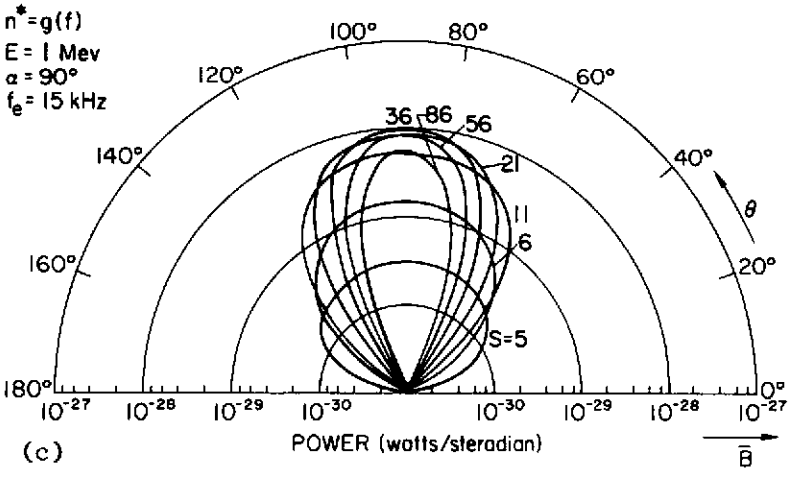

Figure 1.12 a-c $P_s(f,E,B,\theta,\alpha,n^*)$ VERSUS THETA FOR AN ELECTRON RADIATING IN AN ISOTROPIC MEDIUM WHERE n^* IS A FUNCTION OF FREQUENCY AND f_p = 15 kHz.

generated. This phenomenon is explained by noting that for emission and propagation to occur, n^* must be greater than zero. For $\alpha = 90^o$ and $f = sf_g = sf_e/\gamma$, n^* can be expressed as

$$n^* = \sqrt{1 - \frac{f_p^2}{s^2 f_g^2}} \tag{1.27}$$

Thus,

$$s \geq \left[\frac{f_p}{f_g} \right] + 1 \tag{1.28}$$

This expression is plotted in Figure 1.13, where the particle energy is given as a parameter. This plot only has values at integral values of s ; the solid curves are drawn to indicate the envelope of Inequality (1.28).

For pitch angles other than ninety degrees, the features described in the last paragraph still apply, as seen by comparing Figures 1.14a-c with 1.8a-c. For $\alpha \neq 90^o$, however, n^* is an implicit function of θ and β_2 . That is, by substituting (1.25) into (1.26), n^* is now given by

$$n^* = \frac{- f_p^2 \beta_2 \cos\theta + sf_g \sqrt{f_p^2 \beta_2^2 \cos^2\theta + s^2 f_g^2 - f_p^2}}{s^2 f_g^2 + f_p^2 \beta_2^2 \cos^2\theta} \tag{1.29}$$

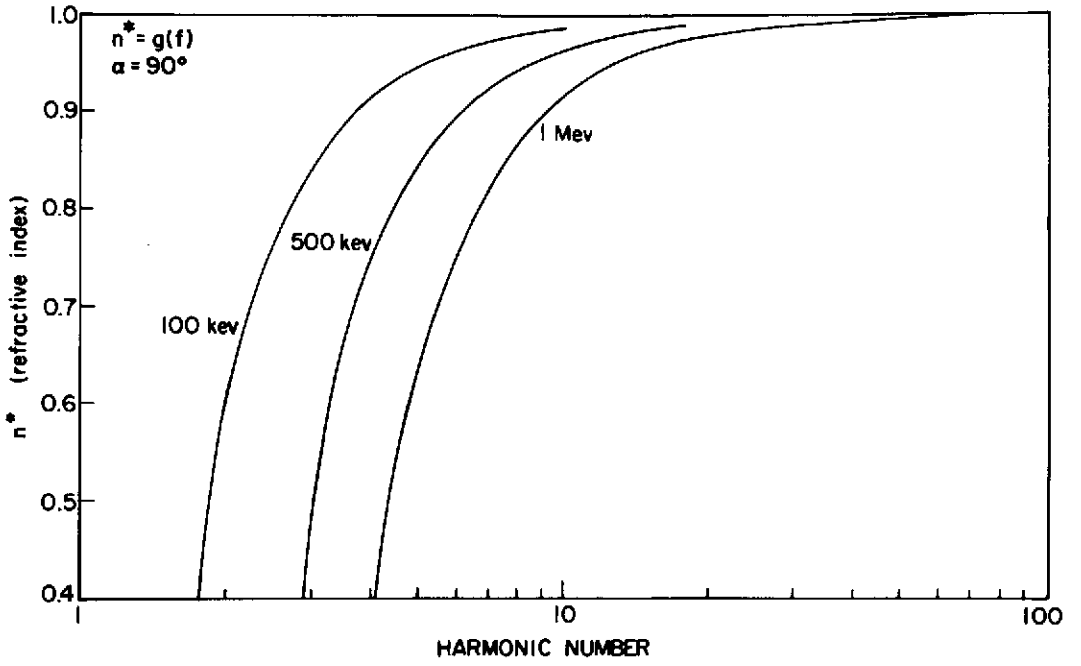

Figure 1.13 ENVELOPE OF THE REFRACTIVE INDEX, n^*, VERSUS HARMONIC NUMBER FOR VARIOUS ELECTRON ENERGIES. THE MEDIUM IS ISOTROPIC AND IS REPRESENTED BY f_e = 15 kHz and f_p = 15 kHz.

This result allows for the interesting possibility that a given set of parameters (s, f_g, β_2 and f_p) will result in n^* becoming less than zero for small values of the angle theta. The consequence of this situation will be demonstrated in the following section where the theory is extended to the general case.

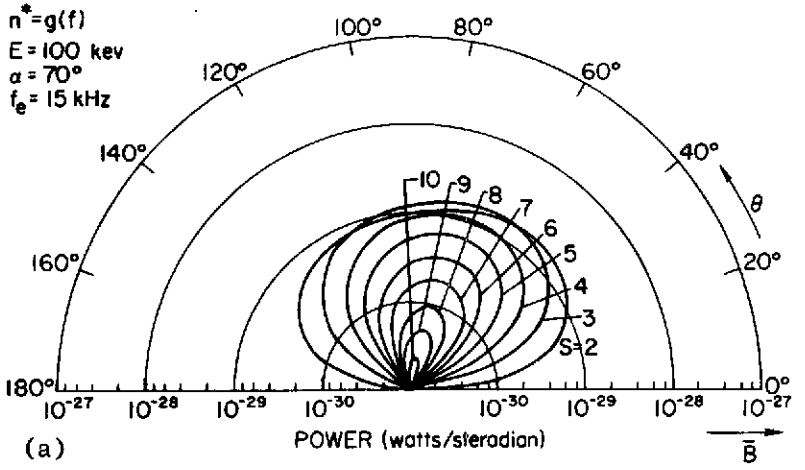

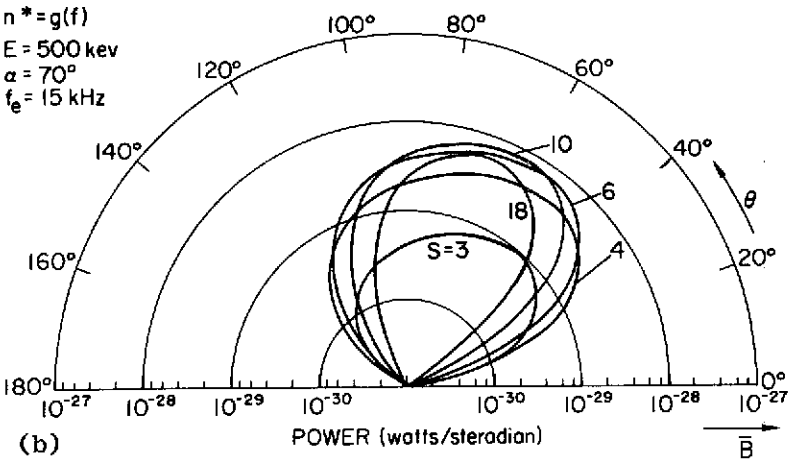

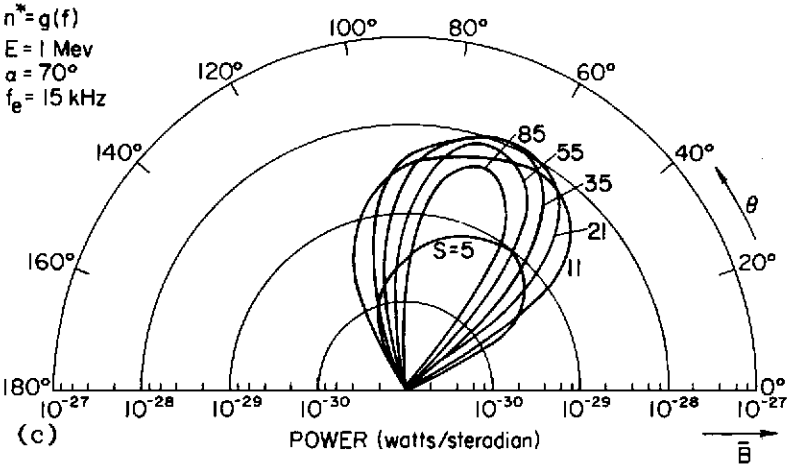

Figure 1.14 a-c $P_s(f,E,B,\theta,\alpha,n^*)$ VERSUS THETA FOR VARIOUS HARMONIC NUMBERS AND THE VALUES OF THE PARAMETERS GIVEN IN EACH FIGURE.

4. Radiation from a Superthermal Electron in a Cold, Anisotropic Plasma

Radiation from a superthermal electron in a cold, collisionless, magnetized plasma has been investigated by several authors [Eidman, 1958; McKenzie, 1967; Melrose, 1968; Truelson and Fejer, 1970] who applied their models to explain VLF and LF radio noise observed at ground-based stations. As a result of their interest in low frequency phenomena, these authors were primarily concerned with whistler mode propagation and hence regions in the magnetosphere where the refractive indices, $n_{\pm}$, (at VLF and LF frequencies) were substantially greater than unity (although their results were valid for $n_{\pm} \geq 0$). The model that gives the emission in an arbitrary anisotropic, collisionless, cold medium is therefore obtained from these studies, but is recast in terms of the parameters X and Y defined in Figure 1.2. The pertinent equations are [Melrose, 1968]

$$P_s(f,E,B,\theta,\alpha,n_{\pm}) =$$

$$\sum_{j=1}^{2} \frac{e^4 s^2 B^2 n_j \Upsilon_j^2}{8\pi^2 \epsilon_o c m_e^2 \gamma^2 (1 - n_j \beta_2 \cos\theta)^2} \frac{\left[-\beta_1 J_s'(\xi) + \left(\frac{A_y s \beta_1}{\xi} + A_z \beta_2\right) J_s(\xi)\right]^2}{\left[1 - \beta_2 n_j \cos\theta \left(1 + \frac{\omega}{n_j} \frac{dn_j}{d\omega}\right)\right]} \tag{1.30}$$

in watts/steradian, where

$$f = s f_g \left[\frac{1}{1 - n_j \beta_2 \cos\theta}\right] \tag{1.31}$$

$$\xi = \frac{s n_j \beta_1 \sin\theta}{1 - n_j \beta_2 \cos\theta} \tag{1.32}$$

$$A_y = H_j \cos\theta + T_j \sin\theta \tag{1.33}$$

$$A_z = T_j \cos\theta - H_j \sin\theta \tag{1.34}$$

$$T_j = \left[1 + H_j^2 \right]^{-\frac{1}{2}} \tag{1.35}$$

$$iH_j = \frac{E_\theta}{E_x} = i \frac{2Y(1-X)\cos\theta}{Y^2 \sin^2\theta \mp \sqrt{Y^4 \sin^4\theta + 4Y^2(1-X)^2 \cos^2\theta}} \tag{1.36}$$

$$iT_j = \frac{E_r}{E_x} i \frac{Y \sin\theta + H_j Y^2 X \cos\theta \sin\theta}{1 - Y^2 - X(1 - Y^2 \cos^2\theta)} \tag{1.37}$$

$$n_j = 1 - \frac{2X(1-X)}{2(1-X) - Y^2 \sin^2\theta \pm \left[Y^4 \sin^4\theta + 4Y^2(1-X^2)\cos\theta \right]^{\frac{1}{2}}} \tag{1.38}$$

If no restrictions are placed on the magnitudes of $n_\pm$ (other than $n_\pm > 0$) there is the possibility that anomalous gyro-synchrotron (given by $s < 0$) and Cerenkov (given by $s = 0$) radiation can be generated concurrently with normal gyro-synchrotron emission ($s > 0$). Result three of Section I.B, however, stated that for the regions of the magnetosphere which we shall be investigating, the frequency of

the radio noise which is generated will be above the local upper hybrid frequency (f_u). This fact implies that f will also be greater than the ambient electron gyro and plasma frequencies. Therefore, $n_{\pm} \leq 1$ which, when taken together with Equation (1.31), gives

$$\cos \theta = \frac{1 - \frac{sf_g}{f}}{n_{\pm}\beta_2} \leq 1 \tag{1.39}$$

Solving for sf_g/f

$$\frac{sf_g}{f} \geq 0 \tag{1.40}$$

and

$$s \geq 0 \tag{1.41}$$

However, for s = 0, sec $\theta = (n_{\pm}\beta_2) \leq 1$, and hence $n_{\pm} \geq (\beta_2)^{-1}$. In general, $\beta_2 < 1$ resulting in $n_{\pm}$ necessarily being greater than unity for s = 0. The medium under study will therefore give rise only to normal gyro-synchrotron emission (s > 0). In this section, this form of radiation from energetic electrons immersed in the complex medium described above will be investigated.

Returning to Equation (1.30), the total power radiated at a given harmonic is the sum of that emitted into two modes (represented by the summation over j), which are the ordinary (n_+, j = 1) and the extraordinary (n_-, j = 2) modes defined by Ratcliffe [1962]. To discuss the total power in general terms is intractable due to the complexity of the mathematics. Nevertheless, a few observations can be made by noting that the general phenomenon is only an extension of

the simpler cases discussed previously. Calculations made by this author showed that the basic characteristics listed in the preceding sections (i.e., the effects on $P_s(f,E,B,\theta,\alpha,n^*)$ of changes in its parameters) remain basically the same for each mode when they are considered separately. Thus the total flux, being the sum of the power radiated into each mode, demonstrates the same dependence on these parameters.

More specifically, Equation (1.30) was used to calculate the emission expected from a superthermal electron under geophysical conditions and locations in the magnetosphere pertinent to this paper. The parameters for two such cases are listed in the headings of Figures 1.15a-h and 1.16a-h respectively. The reason for this choice of parameters and how they relate to this study will become evident in the next chapter. It is intended at this point only to show the effects of the complex medium on the radiation. The new results are summarized below:

a. The maximum power emitted in the ordinary mode is a factor of two or more below that generated in the extraordinary mode for all electron energies E. This ratio is a function of E, increasing as E increases. (In free-space, however, calculations for $E \geq 10$ kev showed that this ratio lies between 0.3 and 3.0 where $|\theta| \geq |\alpha - 10^o|$ and increases rapidly for $|\theta| = |\alpha - 10^o|$. Thus, for $n_{\pm} = 1.0$ and for particles whose instantaneous orbital planes are directed near or along the direction of observation, the power radiated into the ordinary mode is comparable to that radiated into the extraordinary mode.)

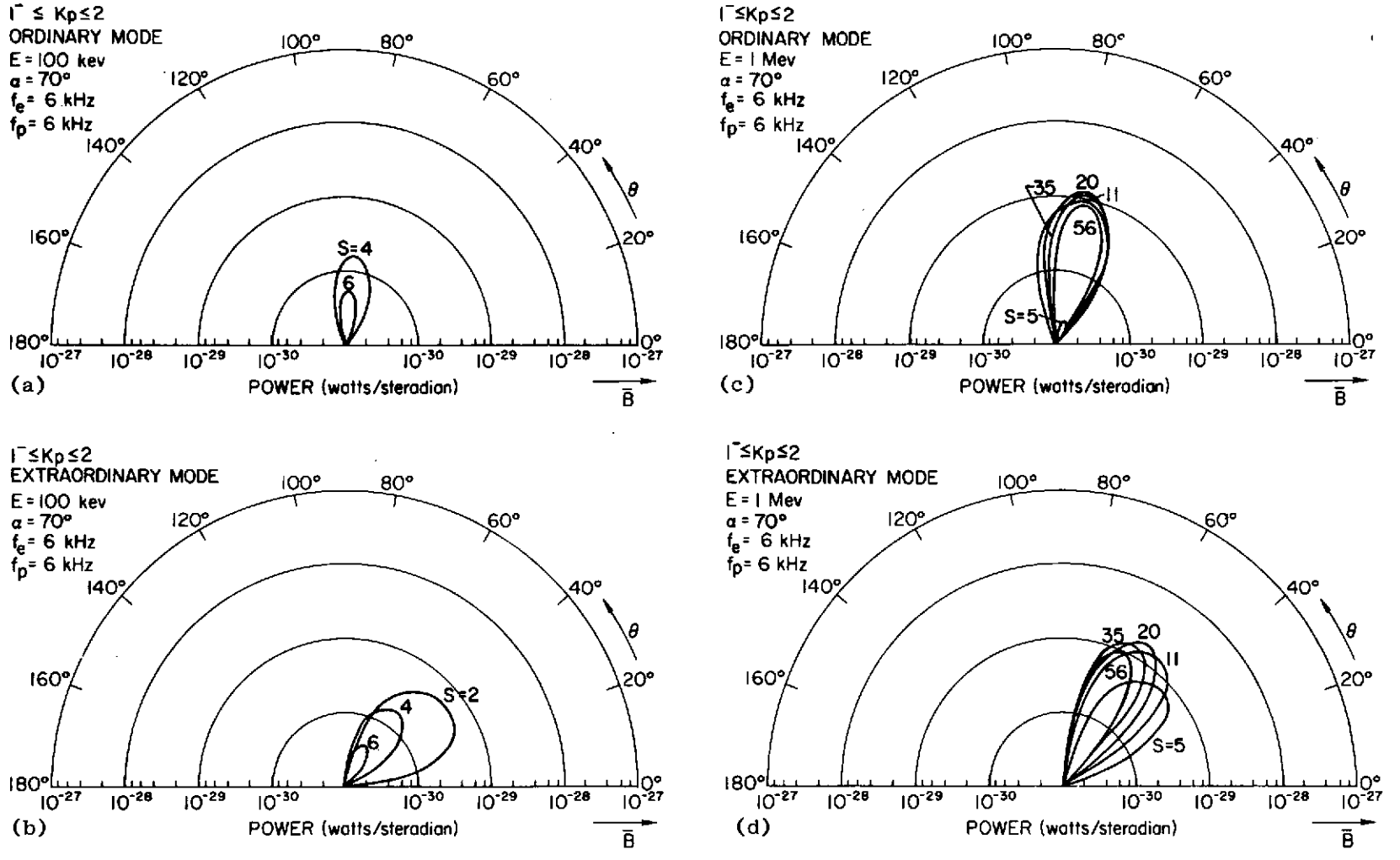

Figure 1.15 a-h $P_s(f,E,B,\theta,\alpha,n_\pm)$ VERSUS THETA FOR AN ELECTRON IN AN ANISOTROPIC MEDIUM WHERE f_p = 6 kHz AND f_e = 6 kHz.

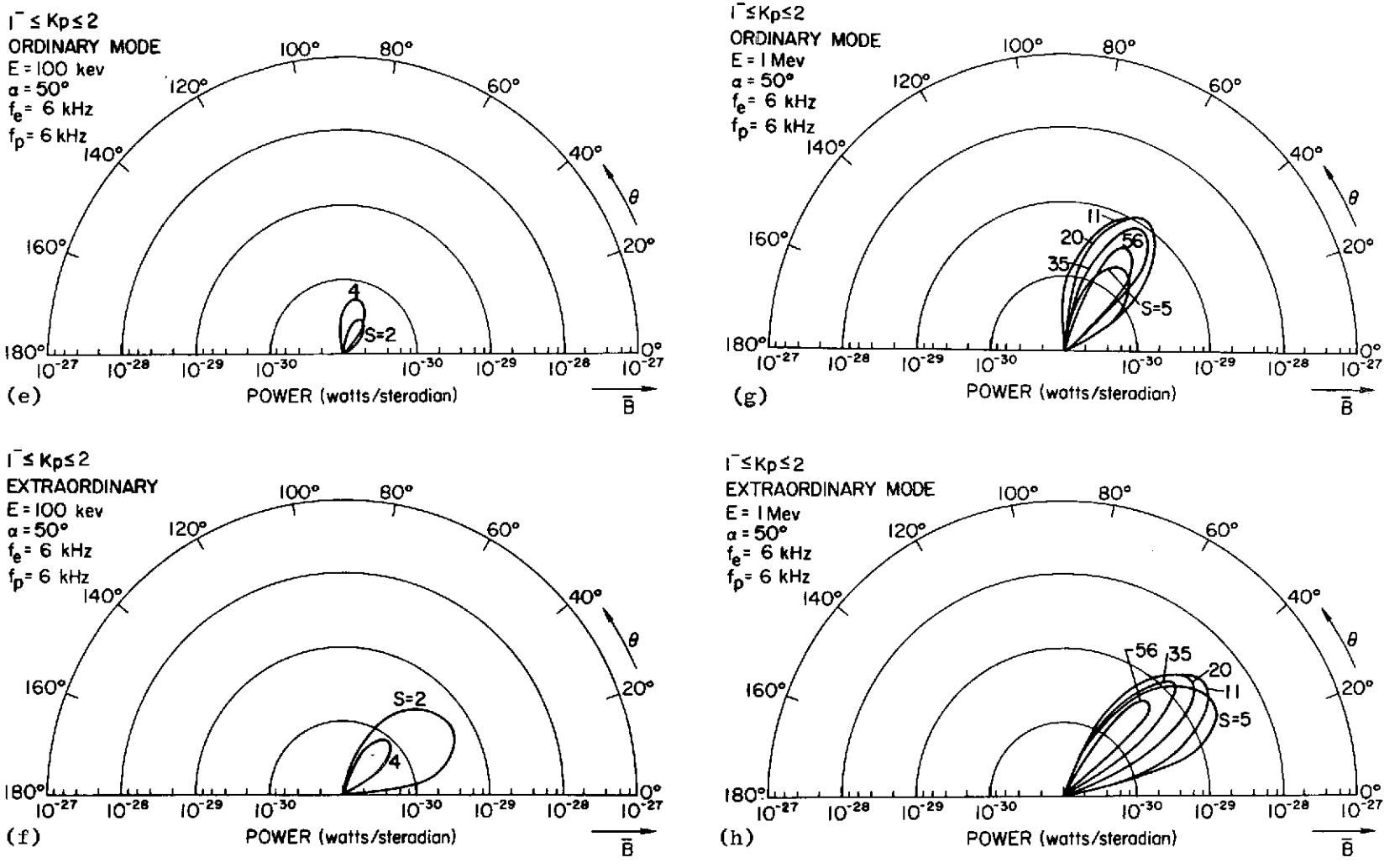

Figure 1.15 (continued)

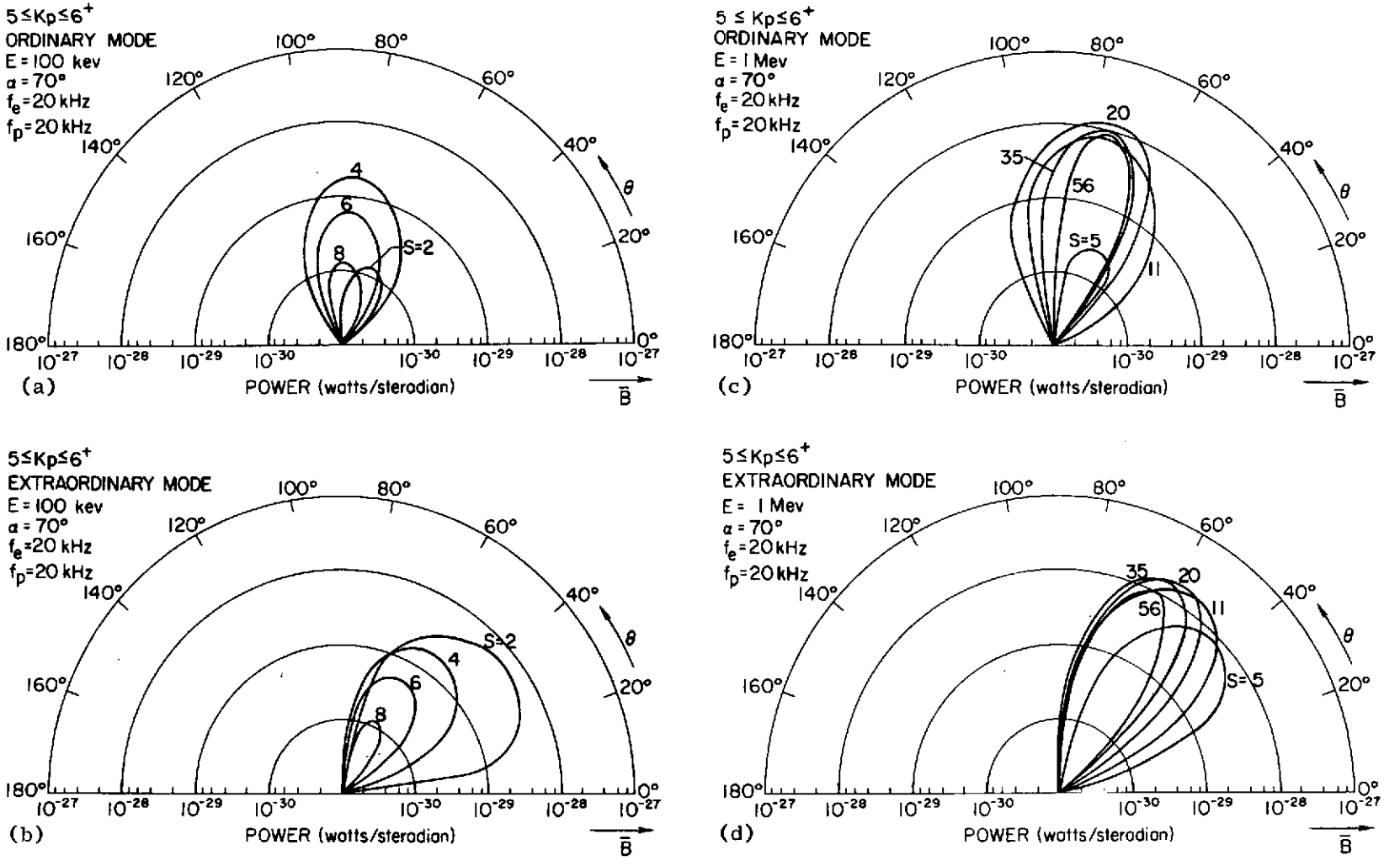

Figure 1.16 a-h $P_s(f,E,B,\theta,\alpha,n_\pm)$ VERSUS THETA FOR AN ELECTRON IN AN ANISOTROPIC MEDIUM WHERE f_p = 20 kHz and f_e = 20 kHz.

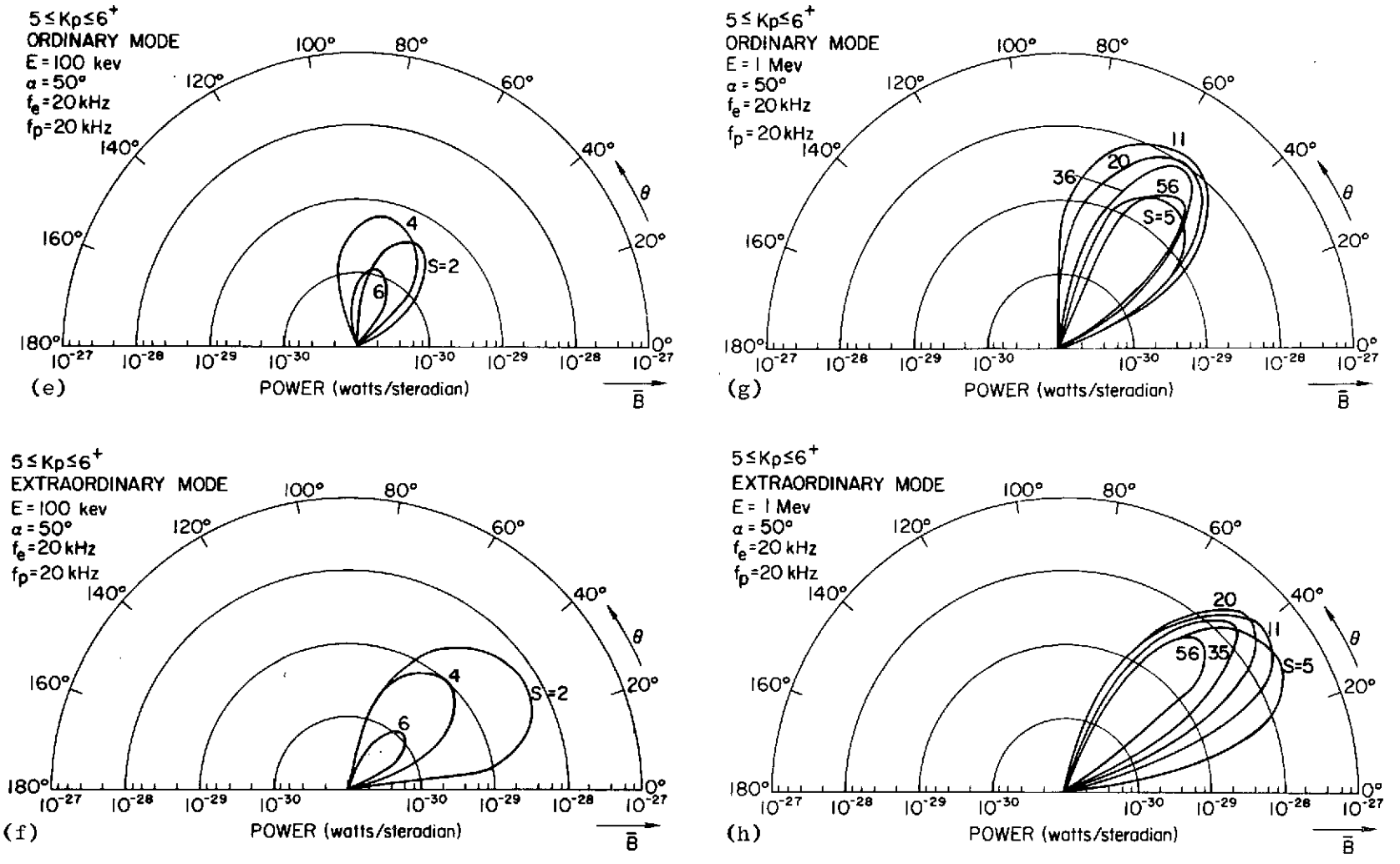

Figure 1.16 (continued)

b. The maximum power in the extraordinary mode is radiated predominantly along $\theta = \alpha$, while the ordinary mode is emitted closer to $\theta = 90^{o}$. This feature is particularly evident for the lower energy electrons and lower harmonic numbers. If these two modes are summed to obtain the total power radiated into a given harmonic, the resultant polar plot for $P_s(f,E,B,\theta,\alpha,n_{\pm})$ will be asymmetrical, as described in Section I.D.2. This result is general and applies to the free-space problem since Equation (1.30) reduces to (1.20) when the appropriate free-space values for n_j, T_j and H_j are used in (1.30) [Eidman, 1958].

c. The Razin effect (Section I.D.3) is evident for each mode, as seen by comparing these figures with those of previous sections.

d. The lowest harmonic generated (i.e., $n_{\pm} > 0$) is the first plotted in each figure. Furthermore, the lower harmonics can be abruptly cut off for small values of the angle theta. This is a result of Equation (1.31) not being satisfied for values of theta less than the critical value θ_c given by

$$\theta_c = \cos^{-1}\left(\frac{1 - \frac{sf_g}{f}}{n_{\pm}\beta_2}\right) \tag{1.42}$$

in which the following inequality must be satisfied:

$$\left|\frac{1 - \frac{sf_g}{f}}{n_{\pm}\beta_2}\right| \leq 1 \tag{1.43}$$

That is, for a given set of parameters s, f_g, f and β_2, values of θ less than θ_c result in values of $n_{\pm}$ ($n_{\pm}$ being a function of f_g, f, f_p and θ) which do not allow Inequality (1.43) to be satisfied.

These results conclude the presentation of the radio noise model which shall be used in the subsequent text to quantitatively determine and discuss the noise generated in the magnetosphere. To this point, however, we have only determined the model for the power radiated at the site of its source, a single superthermal electron. We must now turn to the problem of theoretically deriving the total energy radiated by an ensemble of energetic electrons and the subsequent propagation of this energy from the source region to the observer.

E. The Power Spectral Density Emitted from a Single Electron

In the previous sections the characteristics of $P_s(f,E,B,\theta,\alpha,n_{\pm})$ as a function of its six parameters were investigated in detail to give the reader an understanding of the basic properties of the gyrosynchrotron mechanism. However, to calculate the emission coefficient $J(\ell)$ it is necessary to derive an expression for the power spectral density $P(f,E,B,\theta,\alpha,n_{\pm})$ which is expressed in units of watts Hz^{-1} $steradian^{-1}$.

The derivation of $P(f,E,B,\theta,\alpha,n_{\pm})$ as a function of the six variables proves to be unnecessary. As stated in paragraph eight of Section I.B (and justified in Chapter II), the magnetosphere shall be modeled as a stratified medium composed of concentric shells. Within each shell at the geomagnetic equator, B and $n_{\pm}$ can be taken as constant. Furthermore, once the position of an observer relative

to the earth is specified, the parameter θ and hence α can also be taken as constant within each of these shells. (The angle α is determined since emission in the direction θ results from particles with $\alpha \approx \theta$ due to the directivity of the gyro-synchrotron mechanism.) Thus the general function $P(f,E,B,\theta,\alpha,n_{\pm})$ reduces to evaluating $P(f,E)$ for given sets of values for B,θ,α, and $n_{\pm}$.

Theoretically, $P(f,E)$ is the power radiated by an electron, with energy dE about E, into a bandwidth df about f. In Section I.D.4, we found that for an anisotropic medium, f is given by

$$f = \frac{sf_e}{\gamma(1 - n_{\pm}\beta_2 \cos\theta)} \tag{1.44}$$

where

$$\gamma = \frac{E_o + E}{E_o} \tag{1.45}$$

and by definition

$$\beta_2 = \beta \cos\alpha = \sqrt{1 - \frac{1}{\gamma^2}} \cos\alpha \tag{1.46}$$

Substituting (1.45) and (1.46) into (1.44) yields

$$\frac{E_o+E}{E_o} = \frac{\frac{sf_e}{f} \pm n_+ \cos\alpha \cos\theta \left(\frac{s^2 f_e^2}{f^2} + n_{\pm}^2 \cos^2\theta \cos^2\alpha - 1 \right)^{\frac{1}{2}}}{1 - n_{\pm}^2 \cos^2\alpha \cos^2\theta} \tag{1.47}$$

The $\pm$ sign in front of the radical indicates that electrons with two different energies, E_1 and E_2, can generate electromagnetic waves at a frequency f, corresponding to a given harmonic, s.

Differentiating the above expression with respect to f and solving for $|df|$ gives

$$|df| = \frac{f^2(1 - n_{\pm}^2 \cos^2\alpha \cos^2\theta)}{E_o\left[sf_e \pm \frac{s^2 f_e^2 n_{\pm} \cos\alpha \cos\theta}{(s^2 f_e^2 + f^2 n_{\pm}^2 \cos^2\theta \cos^2\alpha - f^2)^{1/2}}\right]} |dE| \tag{1.48}$$

Then the power spectral density for a single electron can be written as

$$P(f,E) = \frac{P_s(f,E)}{|df|} \pm \delta\left[s - \frac{(\gamma - n_{\pm}\sqrt{\gamma^2 - 1} \cos\theta \cos\alpha) f}{f_e}\right] \tag{1.49}$$

where

$P(f,E)$ = power radiated into a frequency interval df about f by an electron with energy dE about E (watts Hz^{-1} $ster^{-1}$)

$P_s(f,E)$ = power radiated by an electron into its s^{th} harmonic (watts $ster^{-1}$)

f = frequency of observation

E = center of energy range within which the electron being

considered must be found. Note that this energy is given explicitly by Equation (1.44) once $f, n_{\pm}, \theta, f_e, \alpha$ and s are specified

$\underline{\delta}(\quad)$ = Dirac delta function which implicitly gives the energy E that the electron must have to radiate at a frequency f for a given s

If we consider the specific case where $\alpha = 90^{\circ}$, $\gamma \gg 1$ and $s \gg 1$, Equation (1.48) reduces to

$$|dE| = \frac{E_o s f_e}{f^2} |df| \tag{1.50}$$

From the argument of the delta function

$$|dE| \approx \frac{\gamma E_o}{s} \tag{1.51}$$

Furthermore, for these values, $P_s(f,E)$ may be considered continuous and $s \cong \gamma f/f_e$ [Peterson and Hower, 1966; Vesecky, 1967]. Substituting these results into (1.49), we obtain

$$P(f,E) = \frac{P_s(f,E)}{f_g} \tag{1.52}$$

This equation is just the approximation used by previous authors [Peterson and Hower, 1966; Vesecky, 1967] when they considered problems related to the detection of synchrotron radiation at frequencies where $s \gg 1$ from relativistic electrons. In this study, however, electrons with energies $E > 50$ kev and $s \geq 1$ must be considered; therefore, the general Equation (1.49) will be used.

F. The Gyro-Synchrotron Emission Coefficient from an Ensemble of Superthermal Electrons

For the problem considered in this paper, the emission coefficient, $J(\ell)$, can be defined as [Vesecky, 1967]

$$J(f,\theta,B,n_{\pm}) = \iint P(f,E,B,\theta,\alpha,n_{\pm})\, N(E,\alpha)dE\, d\alpha \qquad (1.53)$$

where

$J(f,\theta,B,n_{\pm})$ = power radiated at a frequency (f) and angle (θ) from the static magnetic field by an ensemble of electrons with different energies and pitch angles, specified in watts $m^{-3}Hz^{-1}ster^{-1}$

$P(f,E,B,\theta,\alpha,n_{\pm})$ = power spectral density at a frequency f radiated by an electron with energy dE about E and pitch angle α at an angle θ from the magnetic field line, given in units of watts $Hz^{-1}ster^{-1}$

$N(E,\alpha)$ = the number density of electrons with energy dE about E having pitch angle $d\alpha$ about α, specified in units of electrons $m^{-3}\ ster^{-1}$

As stated, the magnetosphere is modeled as a stratified medium in which θ, B, and $n_{\pm}$ are taken to be constant within each layer. Furthermore, the pitch angle distribution of the superthermal electrons satisfies a $\sin^2\alpha$ law (see Section II.B.5) which is much broader in angular extent than the synchrotron emission patterns calculated in the preceding sections. Consequently, the integration with respect to

α in Equation (1.53) reduces to determining the number of electrons which radiate in the direction of θ. Thus, we may express Equation (1.53) as

$$J(f) = \int \frac{P_s(f,E)}{|df|} N(E) \quad \underline{\delta}\left[s - \frac{\left(\gamma - n_{\pm}\sqrt{\gamma^2-1}\cos\theta\cos\alpha\right) f}{f_e} \right] dE \tag{1.54}$$

where

$$N(E) = 2\pi \int_{\alpha_1}^{\alpha_2} N(E,\alpha) \sin\alpha \, d\alpha \tag{1.55}$$

In the last equation, the limits of integration α_1 and α_2 are a function of θ. They will be discussed in depth in Sections III.G.3 and III.H.2.

By virtue of the delta function, Equation (1.54) reduces to the following summation

$$J(f) = \sum_{s=1}^{\infty} \frac{P_s(f,E)}{|df|} N(E) \quad \underline{\delta}\left[s - \frac{\left(\gamma - n_{\pm}\sqrt{\gamma^2-1}\cos\theta\cos\alpha\right) f}{f_e} \right] \tag{1.56}$$

where the delta function is retained in this and subsequent equations to show that the particle energy (E) is determined once a set of values for $s, n_{\pm}, f_e, \theta, \alpha$ and f is specified. Equation (1.56) gives the power in watts m^{-3} Hz^{-1} $ster^{-1}$ radiated at a frequency (f) from

an ensemble of electrons located in a layer of the magnetosphere represented by the quantities B,θ and $n_{\pm}$.

This equation, however, is not in the most convenient form for this study, as the particle density data, given in the next chapter, is expressed as a flux (electrons m^{-2} kev^{-1} sec^{-1}). It is therefore more useful to write (1.56) in the following form

$$J(f) = \sum_{s=1}^{\infty} P_s(f,E) \left|\frac{dE}{df}\right| \frac{N_F(E)}{c\beta(E)} \underline{\delta}\left[s - \frac{\left(\gamma - n_{\pm}\sqrt{\gamma^2-1}\cos\theta\cos\alpha\right) f}{f_e} \right] \tag{1.57}$$

where $|dE/df|$ is given by Equation (1.48) in kev Hz^{-1} and the particle flux $N_F(E)$ is given by $N_F(E) = c\beta(E)N(E)$ per kev.

G. Absorption Mechanisms and the Absorption Coefficient, $K(\ell)$

As the electromagnetic waves propagate through the magnetosphere, it is possible that they can lose energy to the medium from collisions between electrons and other particles [Ratcliffe, 1962] or from gyro-synchrotron self-absorption [Pacholczyk, 1970]. In paragraph five of Section I.B, it was shown that the first process may be neglected. The second, however, must be considered in more detail.

We proceed by using the result obtained by Pacholczyk, who gives the absorption coefficient at a frequency (f) as

$$K(f) = \frac{c^2}{f^2} \int_0^\infty \frac{N(E)}{E^2} \frac{d}{dE}\left[E^2 A(f,E)\right] dE \qquad (1.58)$$

where

$K(f)$ = power absorbed by electrons from an incident electromagnetic plane wave propagating in a direction $\hat{I}$ with a given polarization P (nepers m^{-1})

$A(f,E)$ = energy radiated at a frequency (f) in the direction $\hat{I}$ with a given polarization P by electrons with energy dE about E (watts Hz^{-1} $ster^{-1}$)

This equation can be integrated by parts to yield

$$K(f) = \frac{c^2}{f^2}\left\{ N(E)\, A(f,E) \Big|_0^\infty - \int_0^\infty E^2\, A(f,E)\, \frac{d}{dE}\left[\frac{N(E)}{E^2}\right] dE \right\} \qquad (1.59)$$

The first term in this equation vanishes since $N(E) \to 0$ as $E \to \infty$, and $A(f,E) \to 0$ as $E \to 0$. Furthermore, from the definition of both terms, $A(f,E) = P(f,E)$ and

$$K(f) = -\frac{c^2}{f^2} \int_0^\infty E^2\, P(f,E)\, \frac{d}{dE}\left[\frac{N(E)}{E^2}\right] dE \qquad (1.60)$$

Substituting (1.49) into this equation and once again retaining the Dirac delta function, we obtain

$$K(f) = -\frac{c^2}{f^2}\sum_{s=1}^{\infty} E^2 \frac{P_s(f,E)}{|df|}\frac{d}{dE}\left[\frac{N(E)}{E^2}\right] \underline{\delta}\left[s - \frac{(\gamma - \sqrt{\gamma^2-1}\cos\theta\cos\alpha)f}{f_e}\right]$$

(1.61)

This last equation and the one obtained for J(f) will be used in Chapter III to obtain numerical solutions to the energy transfer equation defined in Section I.C. Before this is possible, however, appropriate models for the magnetosphere must first be developed.

CHAPTER II

MAGNETOSPHERIC MODELS AND RAY PATH CALCULATIONS

A. Introduction

In order to calculate the gyro-synchrotron radiation generated in the earth's outer radiation belt and propagated to an observer in the interplanetary medium, we must develop models for the energetic and thermal electron populations in this portion of the magnetosphere. This problem is complicated, however, by the dynamic behavior of these quantities resulting from geomagnetic activity. An attempt will be made, therefore, to develop models that are representative of average conditions for these populations during three levels of geomagnetic activity: $1^- \leq K_p \leq 2$, $3 \leq K_p \leq 4$, and $5 \leq K_p \leq 6^+$, where K_p is the planetary magnetic three-hour-range index. These models will then be used with the radio model presented in the previous chapter to calculate the intensity, spectrum and variation of the noise generated in the magnetosphere as a function of geomagnetic activity. Finally, these theoretical results for the noise will be compared to the data returned by the GSFC radio experiment on the IMP-6 spacecraft.

These particle models are to be developed from two sources of data: open literature and personal communications. One difficulty arises, however, since the data obtained from these sources were collected prior to the time period covered by the results from the IMP-6 experiment. These data, pertaining to the particle populations, will therefore be extrapolated in time to allow a direct comparison between the theoretically calculated and experimentally measured radio noise.

B. The Superthermal Electron Population

The change in the density of trapped electrons in the outer radiation belt due to geomagnetic activity is believed to be caused by an acceleration and subsequent injection of low energy electrons into the stable trapping regions [Williams and Smith, 1965]. The source of these low energy electrons is not entirely clear at present. However, it is found that the effect of a sudden intensive magnetic disturbance is an increase in trapped electron densities for $L > 3$. (In this study, McIlwain's magnetic coordinates [McIlwain, 1966] will be used to discuss the location of trapped electron fluxes in the earth's magnetosphere.)

Frank et al [1964] found this impulsive increase in the electron intensities to follow an orderly sequence. During the main phase of a magnetic storm, the density of low energy electrons, $40 \text{ kev} \leq E \leq 200 \text{ kev}$, begins to increase within one day after the onset of the storm. Following a delay of several days, the intensity of electrons with $E \geq 1.6$ Mev also increases over pre-storm values by a factor similar to the enhancement of the low energy component of the fluxes. For these fluxes in the outer radiation belt this factor can be 1 to 1.5 orders of magnitude over quiet time flux intensities for $K_p \approx 3$ (moderate activity), and as much as 1.8 to 2.0 orders of magnitude for $K_p \approx 5$ [Freeman, 1964; Frank et al, 1964; Owens and Frank, 1968; Craven, 1966; Williams, 1966; Rose, 1966].

Frank further observed that the intensity of electrons, $40 \text{ kev} \leq E \leq 200 \text{ kev}$, decays over a period of a week from its maximum, disturbed value to its pre-storm level; the more energetic electrons take a

considerably longer period of time. The temporal history for the intensity of electrons 200 kev < E < 700 kev is intermediate to the low and high energy components of the fluxes.

These large, temporal variations in the trapped electron population make it difficult to determine an average value for the terrestrial noise that is generated by these particles via the gyro-synchrotron mechanism. To simplify the problem (and not neglect these particle fluctuations), models for the trapped electrons as a function of K_p will be developed. That is, we shall determine the expected increase in the electron densities during periods of sustained geomagnetic activity. As pointed out in the introduction, these models are arrived at by using two sources of data, results on the trapped particle population published in the literature and data obtained through personal communications with Dr. Harry West (at Lawrence Livermore Laboratories, Livermore, California) who supplied published and unpublished results from the OGO-5 electron spectrometer experiment.

1. The OGO-5 Electron Spectrometer

A very brief description of the electron spectrometer aboard the OGO-5 is presented to familiarize the reader with this experiment. For a more detailed discussion of this and other experiments on the spacecraft, see West et al [1969].

The electron spectrometer is composed of seven discrete channels that respond to electrons whose energies lie in the ranges given in Table 1. This table also includes the acceptance angle for each channel, defined as the effective width at 50% acceptance in the

scan plane [West et al, 1972]. Pitch angle data for the electrons were also obtained in this experiment by scanning the entire aperture of the spectrometer [West et al, 1969].

Table 1

DESCRIPTION OF THE CHANNELS COMPRISING THE ELECTRON SPECTROMETER ABOARD THE OGO-5 SPACECRAFT

Channel No.	Center Energy in kev	Acceptance Angle
1	79	7.6^{o}
2	158	5.9^{o}
3	266	4.7^{o}
4	479	3.5^{o}
5	822	5.3^{o}
6	1530	4.1^{o}
7	2820	2.5^{o}

By combining the data received from this experiment with that available from the literature, it was possible to obtain a reasonable estimate for the differential energy spectrums for the electrons trapped in the outer radiation belt. This model will be assumed representative for the period of time covered by the IMP-6 radio noise data.

2. Differential Electron Flux Spectrums for $1^{-} \leq K_p \leq 2$ in the Geomagnetic Equatorial Plane

Vette et al [1966] have developed a trapped electron environment for both the inner and outer radiation zones through L = 6.0. Their model is an average representation of the energetic electron population

for the time around August 1964, a period of little average geomagnetic activity during solar cycle minimum. This model, termed the AE2 electron environment, was used to generate the differential electron flux spectrums shown in Figure 2.1. They show the average perpendicular electron fluxes that were measured or extrapolated to the geomagnetic equatorial plane. (Vette's model was expressed in terms of omni-directional fluxes, which were converted by this author to perpendicular fluxes to allow comparison with OGO-5 data. A $\sin^2 \alpha$ pitch angle distribution was assumed in the conversion. This assumption will be justified in Section II.B.5.

However, there is one problem with the AE2 model; for $L > 5$ at the geomagnetic equator, in situ data sufficient for an accurate representation of the fluxes could not be obtained. As stated by Vette, "extrapolations to higher L values should be interpreted with caution and only used for order of magnitude estimates" [Vette et al, 1966]. Since the region $5 \leq L \leq 7$ is important to this study, Vette's data will be supplemented with in situ measurements made by OGO-5 for $2 \leq L \leq 9$ and $K_p < 1$ (Figures 2.2a-b). A comparison of Figures 2.1 and 2.2b shows that they agree very well for $L \leq 5.0$ and $E \leq 500$ kev. But, for $L \geq 5.0$ and $E > 1.0$ Mev, the OGO-5 data give fluxes that are larger than Vette's results by factors as great as eight. This difference may be due to the solar cycle; the OGO-5 data were taken during a time of maximum activity (1968). However, Vette [1971] states that as the solar cycle goes from minimum to maximum, an average increase by a factor of four is expected for electron fluxes with $E \approx 500$ kev. Since the fluxes at $E \approx 500$ kev

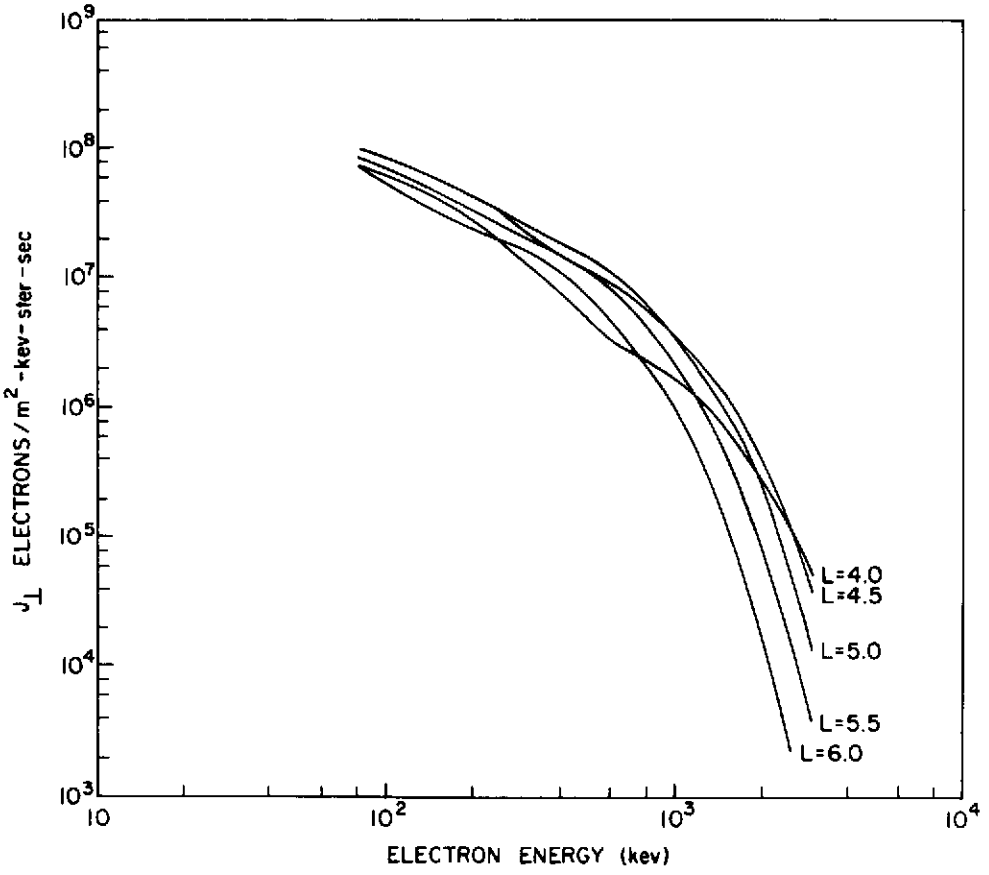

Figure 2.1 DIFFERENTIAL ELECTRON FLUX SPECTRUMS FOR PARTICLES WITH $\alpha = 90^{\circ}$ IN THE GEOMAGNETIC EQUATORIAL PLANE.

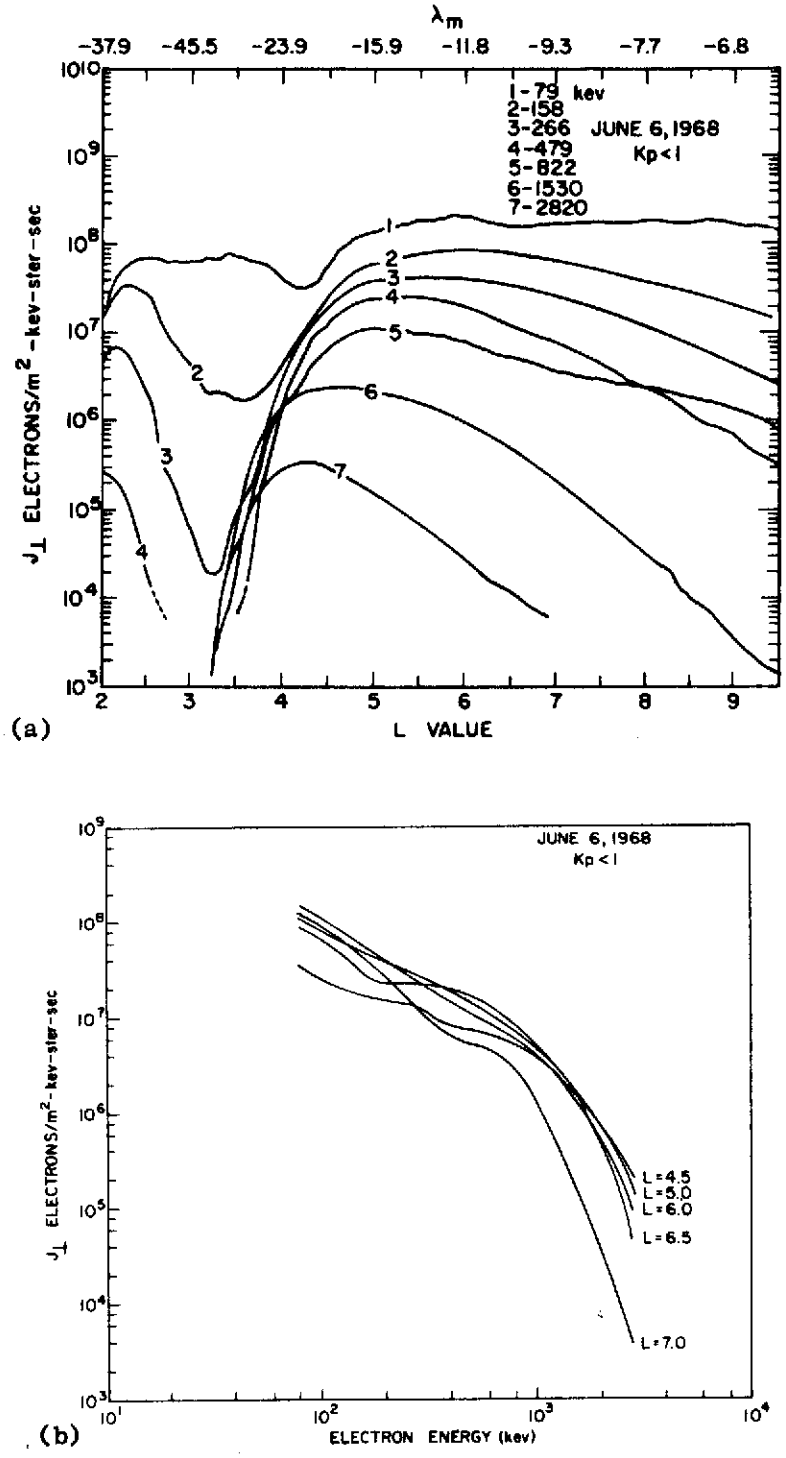

Figure 2.2 a-b DIFFERENTIAL ELECTRON FLUX SPECTRUMS FOR PARTICLES WITH $\alpha = 90^{o}$ MEASURED NEAR THE GEOMAGNETIC EQUATORIAL PLANE [H. West, unpublished data, 1972].

are the least sensitive to geomagnetic activity [Frank et al, 1964; Freeman, 1964], both the lower, 40 kev $\leq E \leq$ 200 kev, and the higher energy electron densities, $E > 1.0$ Mev, should show increases larger than this factor. Contrary to this expectation, Figures 2.1 and 2.2b show that the OGO-5 and AE2 data agree almost exactly for all L values and $E \leq 500$ kev. The implication is that this set of OGO-5 measurements shows fluxes lower than those expected during solar cycle maximum; therefore, the discrepancy between these Figures (2.1 and 2.2b) for $L \geq 5$ and $E \geq 1.0$ Mev, is assumed due primarily to the scarcity of data (particularly from in situ measurements) in Vette's model. To compensate for this lack of data, the AE2 environment was averaged with the OGO-5 data to obtain a new model (referred to as the V-O model), which is more representative of the electron fluxes in the region $5 \leq L \leq 7$ for geomagnetically quiet periods ($K_p < 1^-$) and solar cycle minimum conditions. The validity of this approach is supported by the close agreement between the differential energy spectrum obtained for $L = 6.5$ and the data given by Vette et al [1967] for $L = 6.6$. (Vette obtained results at this L shell from satellites in synchronous orbits.)

The V-O model is still not representative of the condition in the magnetosphere pertinent to this study, as the IMP-6 data were obtained predominantly during periods of sustained geomagnetic activity which resulted in $1^- \leq K_p \leq 2$. Furthermore, the radio noise data were taken during March through October of 1971, a year which was characterized by an abnormally high amount of solar and geomagnetic activity

[see the ESSA publication, Solar-Geophysical Data, for that year]. Thus, we must extend the V-O model on two accounts.

a. First, it is necessary to compensate for differences in the average K_p range represented by this model ($K_p \leq 1^-$) and the range from which IMP-6 data are obtained. The appropriate factor by which the V-O model must be augmented is derived from the results published by Pfitzer et al [1966], Freeman [1964], Owens and Frank [1968], and Craven [1966]. These authors show that there exists a positive correlation between an increase in K_p and the intensity of trapped electrons. In particular, Craven and Freeman observed that, on the average, the increase in the integrated electron flux for $E \geq 40$ kev, when K_p goes from less than 1^- to 2, is a factor of four to five.

As was pointed out earlier, during the early recovery phase of a geomagnetic storm, the increase in the entire spectrum of the trapped radiation is approximately constant and is given by the enhancement of the lower energy electrons. (This constant increase in the electron intensities, for all E, is also shown in Pfitzer's et al [1966] data.) Therefore, it shall be conservatively assumed that the average V-O model must be increased by a factor of three to be valid for $1^- \leq K_p \leq 2$.

b. Second, Vette [1971] points out that the expected enhancement of the maximum flux intensities at E = 500 kev is a factor of approximately four as the solar cycle (and hence solar activity) goes from minimum to maximum. The 500 kev

segment of the electron spectrum, however, appears to be the least sensitive to changes in geomagnetic activity [Frank et al, 1964; Pfitzer et al, 1966]. Thus, as stated previously, one is led to suspect that the increases in the lower, 40 kev $\leq$ E $\leq$ 200 kev, and higher, E $\geq$ 700 kev, electron intensities will be greater than four, as they respond much more dramatically to geomagnetic disturbances [Frank et al, 1964; Craven, 1966]. Consequently, we shall again assume that the averaged V-O model must be increased by a second factor of three.

The final model used to represent the quiet time ($K_p < 1^-$) electron fluxes expected during 1971 is, therefore, the V-O model increased by a factor of three. This model is then increased by a second factor of three in order to make it valid for fluxes at the geomagnetic equator during periods of geomagnetic activity resulting in $1^- \leq K_p \leq 2$.

3. Differential Electron Flux Spectrums for $3 \leq K_p \leq 4$ in the Geomagnetic Equatorial Plane

The differential electron density spectrums for $3 \leq K_p \leq 4$ are derived from the results of Pfitzer et al [1966] and Frank et al [1964]. These studies show that the average increase in the electron intensities (for 40 kev < E < 2 Mev) from quiet time values to periods of moderate geomagnetic activity ($K_p \approx 3$) is 1.0 to 1.2 orders of magnitude. This same enhancement was also found by Craven [1966] and Freeman [1964] for the integrated electron fluxes, E $\geq$ 40 kev, under similar changes in geomagnetic activity.

We have included in Figures 2.3a-b data obtained by OGO-5 in the morning magnetosphere during a period of sustained geomagnetic disturbances in which $K_p \approx 3$. Comparing Figures 2.2b and 2.3b shows that the lower energy electron intensities are increased by a factor of ten; this is consistent with Pfitzer's and Frank's studies. The higher energy electron population ($E \geq 700$ kev), in turn, is enhanced by factors of decreasing magnitude, as both L and E increase. Combining these OGO-5 data with the published results, the average differential energy spectrums expected for $3 \leq K_p \leq 4$ are taken to be equal to the model used in the preceding section, multiplied by a factor of eight. This model not only satisfies the sources quoted above, but also agrees with the average enhancements of trapped electrons caused by the storm time injection process summarized in the first paragraphs of Section II.B.

An interesting feature of the data given in Figures 2.2a and 2.3a is the depletion of the fluxes near $L = 3.0$. The location of the minima in these figures is a function of the particle energy. However, for the K_p ranges considered in this and the preceding section there is a consistent decrease in the electron fluxes (for all energies) in the region $2.5 \leq L \leq 4$, compared to $1.5 \leq L \leq 2$ and $5.0 < L < 7$. This segment of the magnetosphere, referred to as the slot region [Vette, 1971], serves to differentiate between the inner and outer radiation belts, and proves to be important to the discussion in the next section.

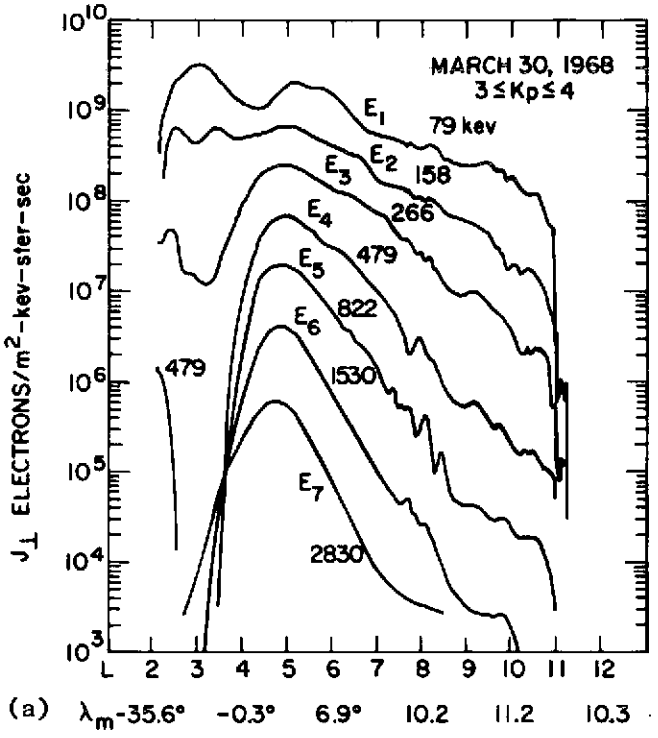

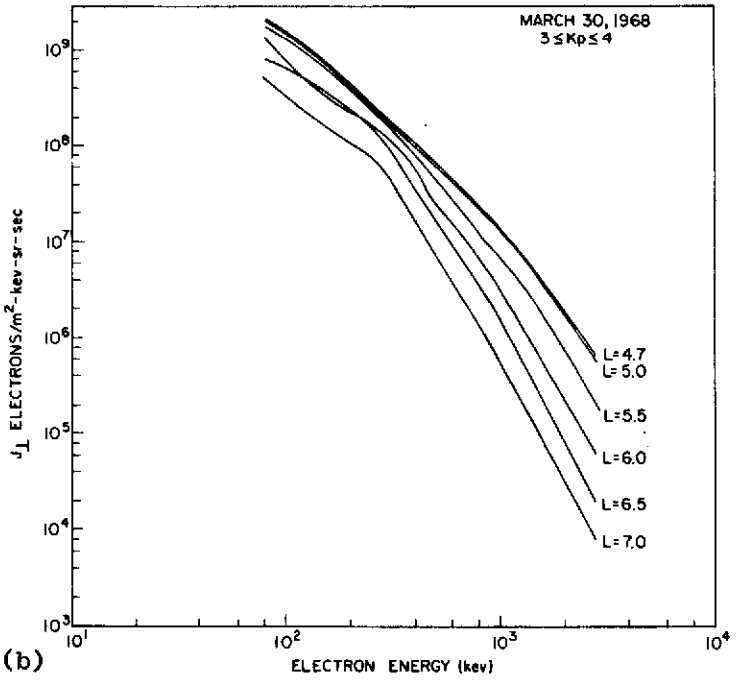

Figure 2.3 a-b DIFFERENTIAL ELECTRON FLUX SPECTRUMS FOR PARTICLES IN THE MORNING MAGNETOSPHERE DURING MODERATE GEOMAGNETIC ACTIVITY. MEASUREMENTS FOR $3 < L < 7$ WERE MADE WHEN $-8^{o} < \lambda_{m} < 8^{o}$ [From West, 1972].

4. Differential Electron Flux Spectrums for $5 \leq K_p \leq 6^+$ in the Geomagnetic Equatorial Plane during the Early Recovery Phase of a Geomagnetic Storm

Due to the scarcity of data for periods of sustained geomagnetic activity in which $5 \leq K_p \leq 6^+$ during May - October 1971 (the time covered by the IMP-6 data), we shall develop a typical differential flux spectrum for the early recovery phase of geomagnetic storms which result in a K_p index of magnitude $5 \leq K_p \leq 6^+$. This model will allow the comparison between theoretical calculations and the radio noise received by the IMP-6 during the 16-18 May and 24-28 September 1971 geomagnetic disturbances.

The storm time temporal variations of the electron intensities in the outer radiation belt follow a very intricate, but repetitive, pattern during the onset and main phase of large geomagnetic storms [Freeman, 1964; Frank et al, 1964; Craven, 1966; Owens and Frank, 1968]. During the early recovery phase, the injection and depletion processes (which result in large, short term fluctuations) have generally subsided, and the fluxes reach their stable disturbed levels from which they gradually decay to pre-storm conditions [Freeman, 1964]. This early recovery phase is characterized by enhancements in the low, 40 kev $< E <$ 200 kev, and high energy, $E > 1.6$ Mev electron fluxes by factors around 40 [Frank et al, 1964]. Freeman [1964] saw this same general increase in intensities; his results for $K_p \approx 4$ show rises in these two components of the trapped electron population by factors of 50 to 100. Craven [1966] conducted

a detailed correlation between K_p and the integrated electron density for $E \geq 40$ kev. His study showed that for $K_p \approx 5^+$, the increase was approximately 60 over quiet time values.

Based on these results, we shall assume average electron fluxes which are a factor of 60 above the quiet time model developed for $K_p < 1^-$. Even though this factor is probably not valid for electron fluxes of 200 kev $\leq E \leq$ 700 kev, the fact that an average model is used results in a calculated brightness for the magnetosphere which differs by less than a few percent from that obtained by using a model where factors of approximately 70 were taken for 40 kev $\leq E \leq$ 200 kev and $E \geq$ 700 kev and a factor of 10 to 20 for 200 kev $\leq E \leq$ 700 kev.

One further important aspect of large geomagnetic storms on the trapped electron population is the injection of energetic electrons into the slot region. In this segment of the magnetosphere, increases in low energy electron fluxes by 1000 are common, and during the recovery phase similar increases (following a main phase depletion) are observed for the high energy electron intensities [West et al, 1970]. This effect is clearly seen in Figures 2.4 and 2.5, which show OGO-5 data taken during the geomagnetic storm of 11 June 1968. These data, which are typical of storms resulting in $K_p \approx 5^+$ [West, personal communication], show that the injection process can bring flux levels in the slot region to values comparable with those in the outer radiation zone. This effect is only seen, however, for storms resulting in moderate to severe geomagnetic disturbances [Hess, 1968].

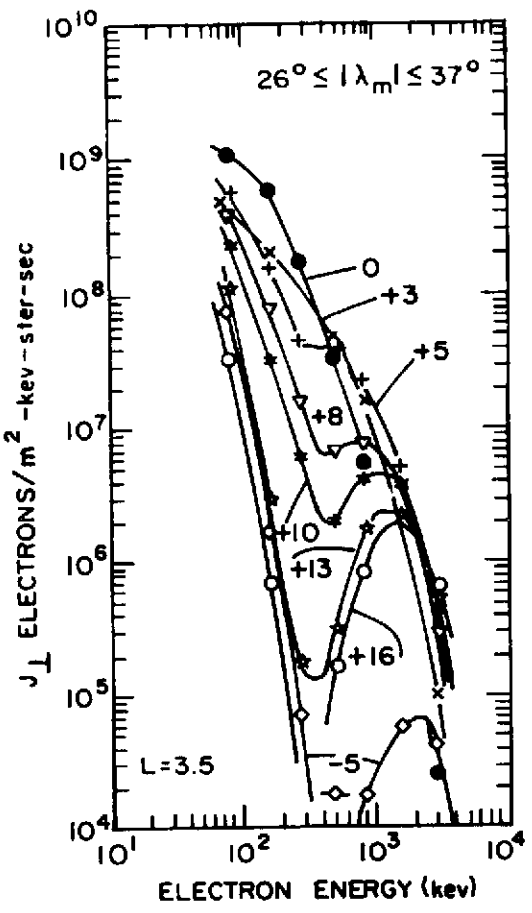

(2.4)

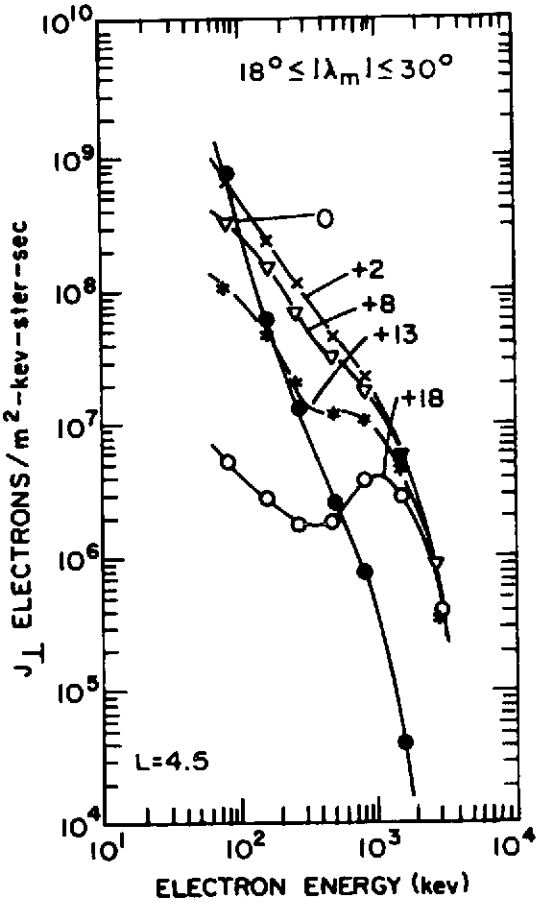

(2.5)

Figure 2.4 THE RESPONSE OF THE ELECTRON FLUXES IN THE SLOT REGION, L=3.5, TO A MODERATE GEOMAGNETIC STORM. LABELS ON THE CURVES INDICATE DAYS PRIOR TO OR AFTER THE ONSET OF THE DISTURBANCE WHICH OCCURRED ON JUNE 11, 1968 [H. West, unpublished data, 1972].

Figure 2.5 THE RESPONSE OF THE ELECTRON FLUXES IN THE OUTER RADIATION BELT, L=4.5, TO A MODERATE GEOMAGNETIC STORM. LABELS ON THE CURVES INDICATE DAYS PRIOR TO OR AFTER THE ONSET OF THE DISTURBANCE WHICH OCCURRED ON JUNE 11, 1968 [H. West, unpublished data, 1972].

The complete model for the electron intensities existing during the early recovery phase of such geomagnetic disturbances must therefore be extended to include the fluxes to $L \approx 3.1$. These fluxes, for $3.1 \leq L \leq 4.0$ and 100 kev $\leq E \leq$ 700 kev, were made a factor of three to four below the fluxes in the same energy interval at $L \approx 5.0$, and this factor was decreased monotonically, for increasing E, to unity for $E > 1.0$ Mev. This allowed the composite model for $5 \leq K_p \leq 6^+$ and $3.1 \leq L \leq 7.0$ to be consistent with the data presented in Figures 2.2b, 2.4 and 2.5 and to still retain the slot region as a separate entity from the outer radiation belt.

5. Pitch Angle Distributions

The pitch angle distribution for the energetic particles proves to be an important consideration in the analysis to follow. Therefore, pitch angle data taken on the fluxes of Figure 2.2a are given in 2.6a-c. These distributions are representative of particles drifting on closed L shells in the morning magnetosphere. It is possible, however, to have pitch angle distributions which are either isotropic or butterfly in nature [West, 1972]. For this study, it will be shown qualitatively that the brightness of the magnetosphere is least for pitch angle distributions which are humped in form (i.e., the maximum fluxes occurring at $\alpha = 90^\circ$ and decreasing monotonically for $\alpha \lesseqgtr 90^\circ$). This distribution is a worst case condition and will be used in the quantitative portions of this paper.

For L values $3.5 \leq L \leq 7$, Figures 2.6a-c indicate that the particle fluxes at a given energy are within a factor of two to three for $\alpha \approx 45^\circ$ compared to $\alpha = 90^\circ$. To put this observation into more

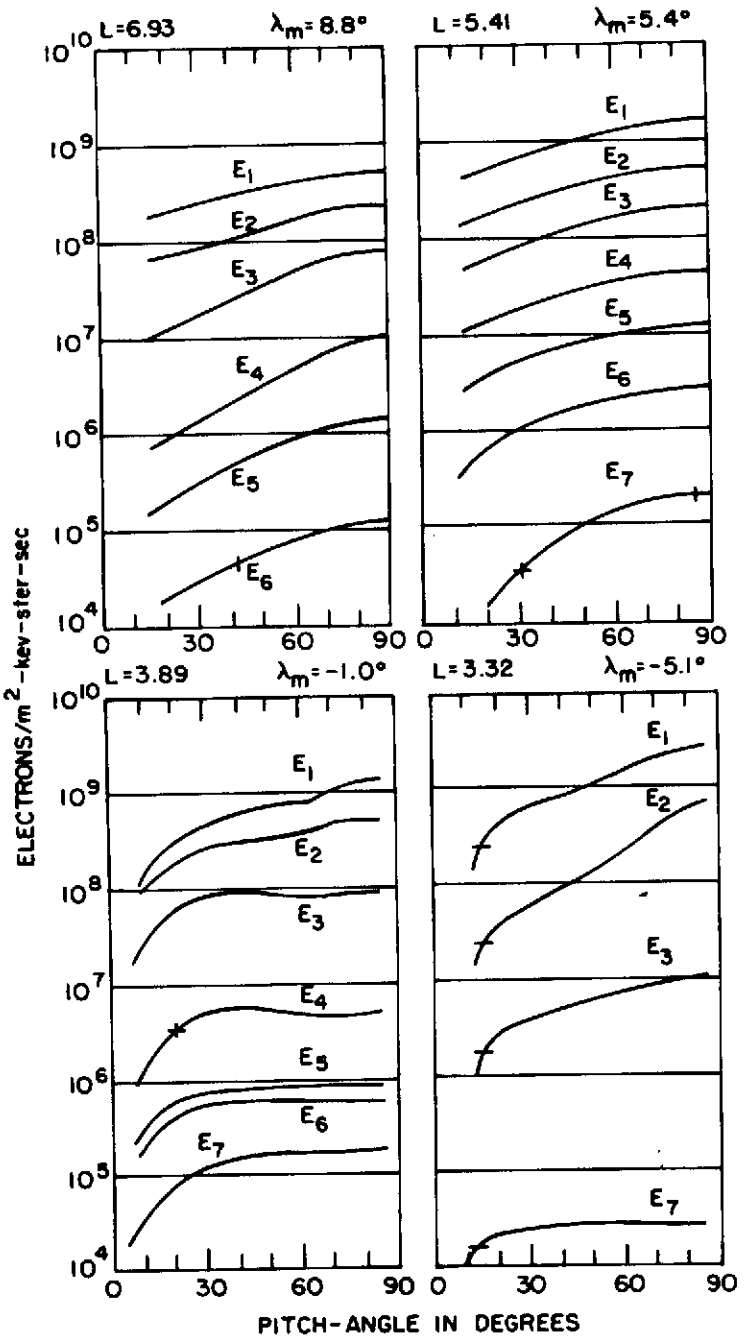

Figure 2.6 ELECTRON FLUX PITCH ANGLE DATA TAKEN CONCURRENTLY WITH THE DATA GIVEN IN FIGURES 2.3 a-b [From West, 1972].

quantitative terms, these data were approximated by a $\sin^2 \alpha$ law. That is, the flux of electrons at a given energy (E) and pitch angle (α) is found from the flux for $\alpha = 90^\circ$ by

$$J_\alpha(E) = J_\perp(E) \sin^2 \alpha \qquad (2.1)$$

This approximation agrees very well with the data shown in these figures as well as the pitch angle data published by Katz [1966].

C. The Thermal Electron Population

The effects of the thermal electron population on the calculated brightness of the magnetosphere have already been discussed in Chapter I, where it was shown that for regions in which the real part of the refractive indices, $n_\pm$, is less than or equal to zero, gyro-synchrotron radiation will not be generated. Furthermore, the radio model proved that if $n_\pm < 1.0$, the intensity of the radiation at a given frequency is substantially reduced below the free-space situation.

Once the electromagnetic energy has detached itself from the source, however, the effect of the thermal plasma reduces to the well-known problem of electromagnetic waves propagating through an ionized medium [Budden, 1961; Ginzburg, 1961; Ratcliffe, 1962; Stix, 1962]. The portion of this theory that is relevant to this study pertains to the propagation of radio waves at a frequency f_1 through regions where $n_\pm(f_1) \leq 0$. It is shown by these authors that if the conditions shown in Figure 2.7 exist, the observer will not receive the energy incident on the left side of the region (assuming the width

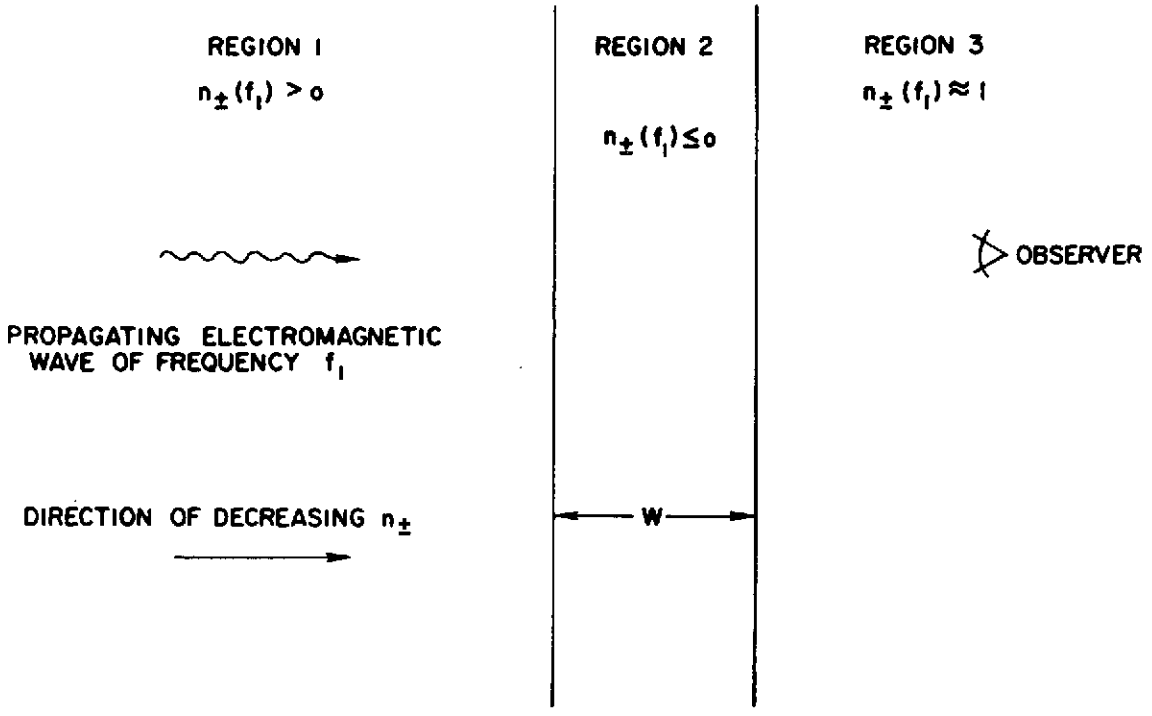

Figure 2.7 RADIATION OF FREQUENCY LESS THAN OR EQUAL TO f_1 IN REGION ONE IS SHIELDED FROM THE OBSERVER BY REGION TWO WHERE $n_{\pm}(f \leq f_1) = 0$.

(w) is many wavelengths of the incident radiation). For an observer located in the interplanetary medium, the situation depicted in this figure will occur for radio noise, 30 kHz $\leq$ f $\leq$ 300 kHz, generated within certain segments of the magnetosphere (as discussed in Section II.G). Thus, it is necessary to determine the thermal electron density in (B,L) space as a function of geomagnetic activity, as this particle population will be significant to the results of the next chapter. To this end, in situ and indirect measurements on the density and response of the ambient plasma to magnetic disturbances are used to derive an appropriate model.

1. Response of the Thermal Plasma at the Geomagnetic Equator to Variations in K_p

The plasmapause, defined in the literature as the location of a sudden decrease in the thermal plasma density as one moves radially outward from the earth, separates a region of high thermal electron density (the plasmasphere) from a region of very low density (the plasmatrough). (Schematic diagrams defining these regions in the earth's magnetosphere are given in Chappell [1972] and Carpenter [1968].) This phenomenon has been studied to a great extent in the geomagnetic equatorial plane, and the results are briefly summarized below:

a. OGO-1 and OGO-3 data [Taylor et al., 1968], obtained for local time near midnight, show a sudden decrease in the magnetospheric proton density from 10^9 ions m^{-3} to 5×10^6 ions m^{-3} in instances of less than one half an earth radius as one moves radially outward from the earth along the geomagnetic equator. (The lower bound of 5×10^6 ions m^{-3} is a result of instrument limitations.) Furthermore, there is a correlation between geomagnetic activity and the distance to the plasmapause, which decreases from $L = 5.0$ during undisturbed times to $L = 3.5$ or less for $K_p \approx 5^+$.

b. Whistler data [Carpenter, 1966, 1970, 1971; Angerami and Carpenter, 1966; Carpenter et al., 1971] show these same results with the added feature that a bulge in the plasmapause exists for local times between 1800 and 2100 hours. At this bulge, the distance to the plasmapause may be as large as 5.0

earth radii, compared to 3.5 for the 0600 - 0800 time zone, during periods of moderate geomagnetic activity. Whistler data also indicated that the position of the plasmapause changes with a delay of at most a few hours in response to geomagnetic disturbances.

c. A comprehensive study of the plasmapause has been carried out recently by Chappell et al [1970] and Chappell [1972] from OGO-5 data. They showed that the response of the plasmapause to changes in K_p is observed both in the 1000 ± 2 hour and 0200 ± 2 hour local time zones after a two to six hour time delay from the onset of the geomagnetic disturbance. This time delay was most evident for the 0200 ± 2 hour zone, but also fits the data from the 1000 ± 2 hour region.

As a result of the increased sensitivity of the experiments aboard the OGO-5 (compared to OGO-1 and OGO-3) it was also discovered that, for undisturbed periods, the change in the thermal proton density (as the plasmapause was crossed) was from 10^9 ions m^{-3} to approximately 3×10^5 ions m^{-3} over a distance of one earth radius. As geomagnetic activity increased, this same three orders of magnitude change in density occurred over distances of only 600 km.

For this paper, the results of these investigations were combined to obtain the following relationship between the location of the plasmapause in the geomagnetic equatorial plane and K_p.

$$L_p = 5.6 - 0.45\ K_p \qquad (2.2)$$

We shall assume (based on OGO-5 data) that, after a maximum delay of six hours, Equation (2.2) gives the average plasmapause location in the 2100 to 1800 hours local zone. From 1800 to 2100 hours, it will be assumed there exists a bulge in the plasmapause extending to $L \approx 5.0$.

The data obtained by OGO-5 were also used to determine density profiles for the thermal electron population as a function of K_p. Linear approximations to these data, for the three K_p ranges specified previously, are given in Figure 2.8

D. The Electron Plasma and Gyrofrequencies as a Function of K_p and L in the Geomagnetic Equatorial Plane

The electron plasma frequency, as a function of K_p, is found from the data in Figure 2.8 by using [Rossi and Olbert, 1970]

$$f_p \approx 9\sqrt{N_e} \qquad \text{Hz} \qquad (2.3)$$

where

N_e = electrons m^{-3}

The results are shown in Figures 2.9 a-c.

To determine the electron gyrofrequency at the geomagnetic equator, the variation of the magnetic field intensity (B) in this plane as a function of K_p must be obtained. Roederer [1970] states that the field at the magnetic equator can be expressed as

$$B_o(r) = \frac{k_o}{r^3} + k_1 - k_2 r \cos\phi \qquad (2.4)$$

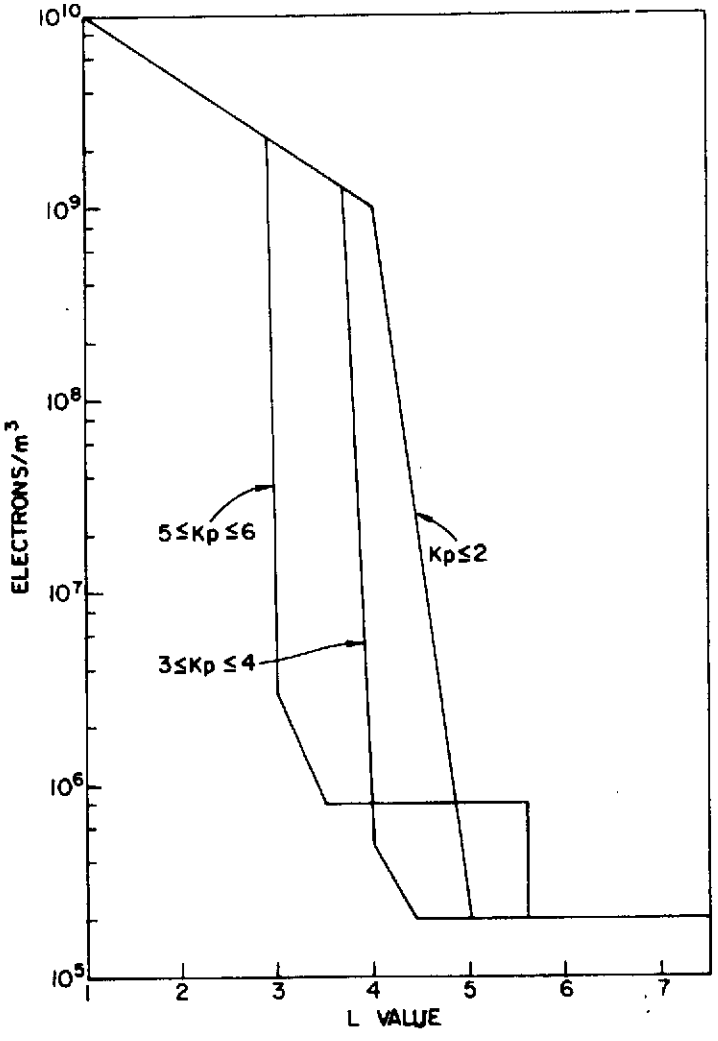

Figure 2.8 THERMAL ELECTRON DENSITY IN THE GEOMAGNETIC EQUATORIAL PLANE AS A FUNCTION OF L FOR THREE K_p RANGES [From Chappell et al , 1970].

where

$$k_o = 3.11 \times 10^4 \text{ gamma}$$

$$k_1 = \frac{12 \times 10^3}{R_s^3} \text{ gamma} \qquad (1.0 \text{ gamma} = 10^{-5} \text{ gauss})$$

$$k_2 = \frac{2.27 \times 10^4}{R_s^4} \text{ gamma}$$

R_s = distance from the center of the earth to the subsolar point of the magnetosphere in earth radii.

ϕ = longitude east of midnight.

r = distance from the center of the earth at which B_o is to be evaluated (in earth radii).

Changes in K_p are accounted for in this equation by R_s. For $K_p \leq 2$, $R_s \approx 10\ R_E$; during a severe compression of the magnetosphere, R_s may be as low as 6 R_E (earth radii).

This equation was evaluated for $R_s = 10\ R_E$, $K_p \leq 2$; $R_s = 8\ R_E$, $3 \leq K_p \leq 4$; and $R_s = 7\ R_E$, $5 \leq K_p \leq 6^+$ as a function of ϕ. The values for B_o were then used to calculate the electron gyrofrequencies for nonrelativistic particles in the equatorial plane; the results are plotted in Figures 2.9a-c with the electron plasma frequencies.

The curves for f_e and f_p allow an important simplification to be made. Intuitively, we expect the radiation emitted by superthermal electrons to increase for decreasing L in the geomagnetic equatorial plane, since both the magnetic flux density (B) and the energetic electron population increase. This indeed occurs, as demonstrated in Chapter III, where the calculations show that the bulk of the radiation, for any K_p value, emanates within two to three earth radii from the

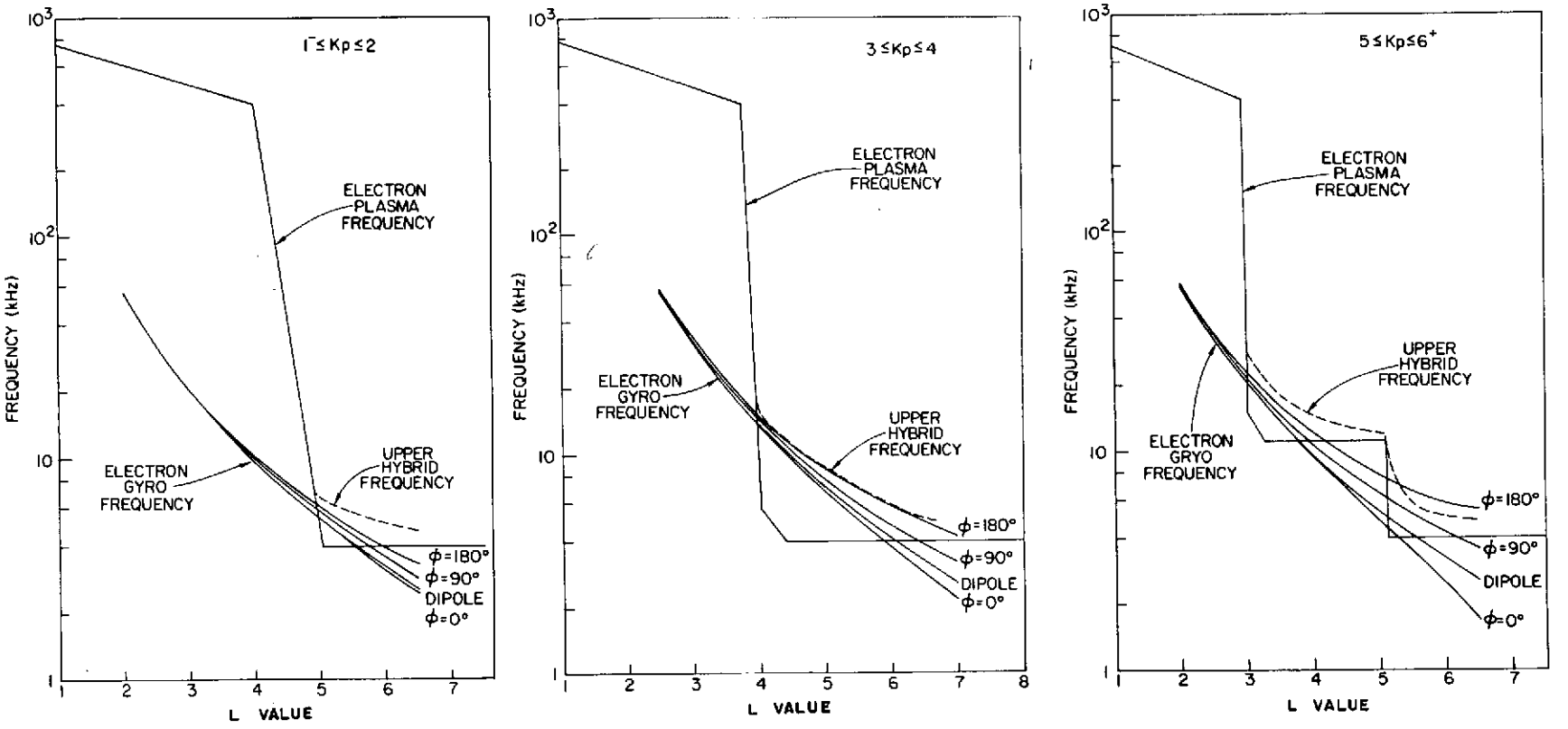

Figure 2.9 a-c ELECTRON PLASMA AND GYROFREQUENCIES IN THE GEOMAGNETIC EQUATORIAL PLANE AS A FUNCTION OF L FOR THREE K_p RANGES. THE UPPER HYBRID FREQUENCY (f_u) WAS CALCULATED USING f_p AND f_e (DIPOLE).

plasmapause (in a direction away from the earth). The preceding figures illustrate that, for $L_p + 3\ R_E$, the difference between the electron gyrofrequency as one proceeds from the midnight to the noon meridian is a maximum of 3.5 kHz (for each K_p range) with respect to the dipole field. Since this discrepancy proves insignificant to the theoretical results, the earth's magnetic field can be satisfactorily approximated by a centered dipole model for this study.

E. Extension of the Particle Models to Regions off the Geomagnetic Equator

Thus far we have developed the models for the thermal and energetic electron populations as a function of K_p in the geomagnetic plane. These data, however, are not sufficient to calculate the brightness of the magnetosphere. To complete these models, the discussion of the previous section must be extended to regions of the magnetosphere off the equator.

1. The Thermal Electron Density in (B,L) Space

Carpenter [1966] has found that the plasmasphere can be modeled as a doughnut-like cloud of ionization with a sharp, field-aligned boundary. This magnetic field line, which bounds the region of high thermal electron density, passes through the plasmapause at L_p in the geomagnetic equator.

This boundary serves as a natural divider for calculating the thermal electron densities off the geomagnetic equator. Well within the plasmasphere, the thermal electron density is high enough to cause sufficient collisions between electrons to establish a diffusive-equilibrium distribution of plasma along the field lines. Outside

the plasmapause, collisions are rare, and an idealized collisionless distribution is appropriate. These features imply that, for magnetic field lines within the plasmapause and near the earth's surface, the plasma density decreases with distance along the field line (measured from the earth) in accordance with a diffusive distribution law; outside the plasmasphere, the density decreases with distance as R^{-4} [Park, 1970; Helliwell, 1970]. As the portion of the magnetosphere outside of the plasmapause proves important to this study, the thermal electron density in (B,L) will be calculated by extrapolating the value at the equator (for a given L) using this R^{-4} power law.

2. The Energetic Electron Population in (B,L) Space

In this paper, only energetic particles which are stably trapped will be considered sources of gyro-synchrotron noise. The lifetime of these particles, in the stable trapping regions, ranges from three days at $L \approx 6$ to six days at $L \approx 4$ [Hess, 1968]. Consequently, the energetic electron population would be lost if it were not for the continual replenishment of these particles by geomagnetic disturbances.

As a result of the short bounce and drift periods for electrons with 100 kev $\leq E \leq$ 5 Mev (which are a maximum of seconds to hundreds of minutes, respectively, [Hess, 1968]) and the long particle lifetimes, these particles will distribute themselves uniformly along drift shells within hours after injection. The resulting population in (B,L) space can therefore be determined by using Liouville's theorem, which is given by

$$J_P(E, \cos \alpha_P) = J_O(E, \cos \alpha_O) = J_O\left\{E, \left[1 - \frac{B_O}{B_P}(1 - \cos^2 \alpha_P)\right]^{\frac{1}{2}}\right\} \tag{2.5}$$

This equation shows that the flux of particles, $J_P(E, \cos \alpha)$, having energy E and pitch angle α_P, measured at a point P on a given magnetic field line, results from the flux of particles, $J_O(E, \cos \alpha_O)$ on the same field line, with pitch angle α_O, passing through the point O. Equation (2.5) can be put into the following more useful form when $\alpha_P = 90^o$

$$J_P(E,0) = J_O\left\{E, \left[1 - \frac{B_O}{B_P}\right]^{\frac{1}{2}}\right\} \tag{2.6}$$

where, as a result of the dipole field approximation,

$$B_P = \frac{B_O(1 + 3 \sin^2 \lambda_m)^{\frac{1}{2}}}{\cos^6 \lambda_m} \tag{2.7}$$

In these equations

B_O = magnetic flux density at the geomagnetic equator measured at point O.

B_P = magnetic flux density measured at point P along the same dipole field line passing through point O.

λ_m = geomagnetic latitude

$J_P(E,0)$ = perpendicular flux of particles of energy E measured at the point P.

$J_O\left\{E, \left[1 - \frac{B_O}{B_P}\right]^{\frac{1}{2}}\right\}$ = flux of particles of energy E measured on the equator (at point O) with pitch angle α defined by $\cos \alpha = \left(1 - \frac{B_O}{B_P}\right)^{\frac{1}{2}}$.

For example, if we consider L = 5.0 and $K_p \leq 2$, Figure 2.2a shows that $J_\perp(E = 266 \text{ kev}) \approx 4 \times 10^7$ electrons m^{-2} kev^{-1} $ster^{-1}$ sec^{-1} at $\lambda_m \approx -15^\circ$. To calculate the perpendicular flux at L = 5.0 and $\lambda_m = 38^\circ$, we proceed as follows:

$$J_P(E, \cos \alpha_P) = J_P(E,0) = J_P(E,0,L = 5^\circ, \lambda_m = 38^\circ)$$

$$= J_O(E, \cos \alpha_O, L = 5, \lambda_m = 0^\circ) = J_O\left\{E, \left[1 - \frac{B_O}{B_P}\right]^{\frac{1}{2}}\right\}$$

$$= J_O\left[E, (1 - 0.16)^{\frac{1}{2}}\right] = J_O(E, 0.91)$$

Using the $\sin^2 \alpha$ pitch angle distribution,

$$J_O(E,0.91) = J_O(E,0) \sin^2 23.9^\circ = 0.16\, J_O(E,0)$$

Going through this procedure once more to account for the flux of Figure 2.2a being measured at $\lambda_m = -15^\circ$, we find that:

$$J(E,0,L = 5.0, \lambda_m = 38^\circ) = (0.25)\, J(E,0,L = 5.0, \lambda_m = -15^\circ)$$

$$= 10^7 \text{ electrons } m^{-2} \text{ sec}^{-1} \text{ kev}^{-1} \text{ ster}^{-1}$$

This value compares well with the OGO-5 data shown in Figure 2.10, which is the extension of Figure 2.2a to higher geomagnetic latitudes.

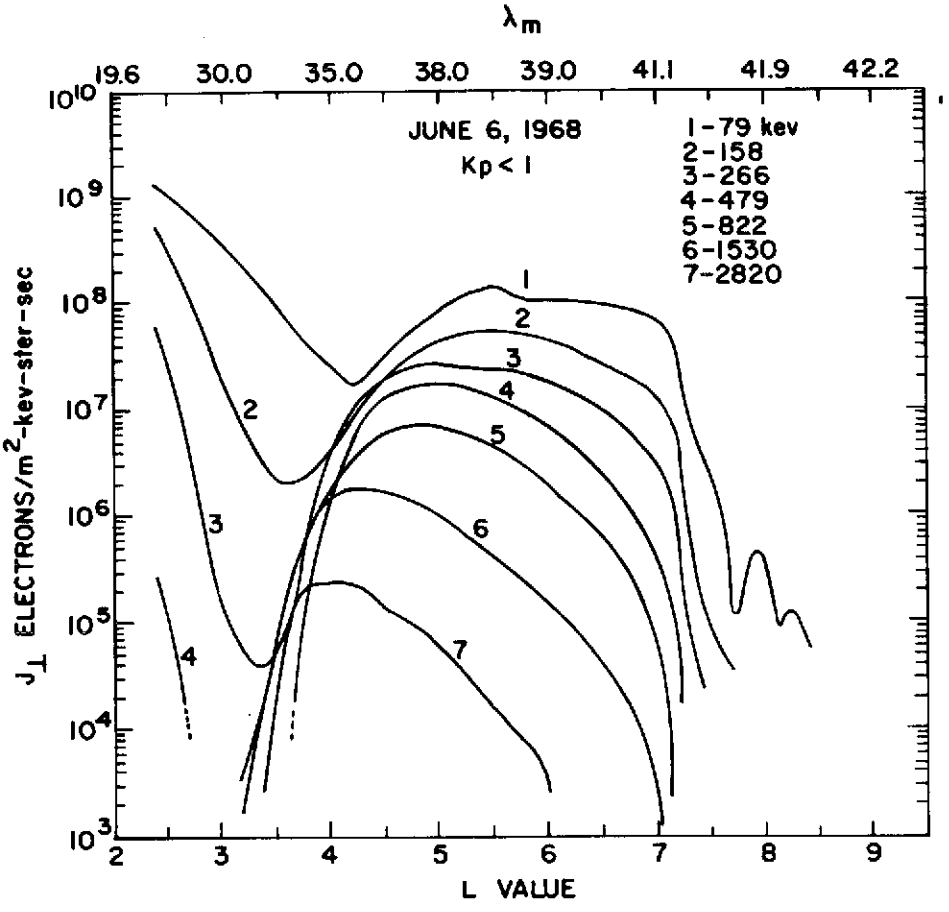

Figure 2.10 EXTENSION OF THE ELECTRON FLUXES OF FIGURE 2.2a TO REGIONS OFF THE GEOMAGNETIC EQUATORIAL PLANE [H. West, unpublished data, 1972].

F. Stratification of the Magnetosphere

To evaluate the equation for the transfer of radiation (1.11) from source to observer on a digital computer, it is necessary to stratify the magnetosphere. Previous sections pointed out that a sufficiently accurate value for the generated radio noise can be obtained by considering only the electrons trapped in a dipole magnetic field. The particle dynamics in this type of field configuration have been investigated by Roederer [1967, 1970], who showed that the trapped particles are constrained to move along closed L shells (or drift shells) which are determined by rotating dipole field lines about the dipole axis. Therefore, the most natural stratified representation of the magnetosphere is a collection of concentric L shells. It remains, however, to determine a convenient distance (ΔL) between each shell at the geomagnetic equator.

This problem was resolved by running a few trial calculations for the noise based on different ΔL values, under the assumption that all the radiation emanates from the geomagnetic equatorial plane. The results indicated that if ΔL was greater than 0.3 earth radii, the calculated radio noise spectrum varied considerably from one shell to the next, and the summed spectrum for all the shells showed a characteristic cyclotron harmonic structure at the lower frequencies. This is a result of these frequencies being close to the fundamental gyrofrequency of electrons with $E \approx 100$ kev. [See Bekefi, 1966; Figure 6.10a, for an example of this effect.] The cyclotron structure was particularly evident for $5 \leq K_p \leq 6^+$, as f_e attains values to 66% of the lowest frequency considered in the paper (30 kHz).

However, these fluctuations in the summed radio spectrums become insignificant and a reasonably good power law for the radio noise was obtained when a ΔL value of 0.125 earth radii was used. The magnetosphere was therefore modeled as a set of concentric drift shells separated by this ΔL value in the geomagnetic equatorial plane. The center of each shell in this plane (in the region of interest) is given by

$$L_s = 3.0 + j(0.125) \qquad j = 0,1,2 \ldots \tag{2.8}$$

G. The Refractive Indices in (B,L) Space

Using Equation (1.38), the values for $n_{\pm}$ (both when theta equals zero and theta equals ninety degrees) were calculated and plotted in Figures 2.11 a-f. These curves show that, for each mode, there exists a region at the geomagnetic equator for which $n_{\pm}$ is equal to zero. Furthermore, for each K_p range, this region is located within the plasmasphere and ends abruptly at the plasmapause. This same situation also exists when the refractive indices are calculated in (B,L) space along the plasmasphere-plasmatrough boundary. Heuristically, this result is supported by the following argument. Choose the L value (for a given K_p range) which determines the location of the plasmapause in the geomagnetic equatorial plane. Moving toward the magnetic poles along field lines which pass through this L value, both the field flux density (Equation 2.4) and the thermal electron population increase. Thus, at a given frequency, the real parts ($n_{\pm}$) of the refractive indices will decrease in magnitude toward zero for a value less than or equal to unity at the equator. If $n_{\pm}$ is already zero at the equator, it will not change as one moves

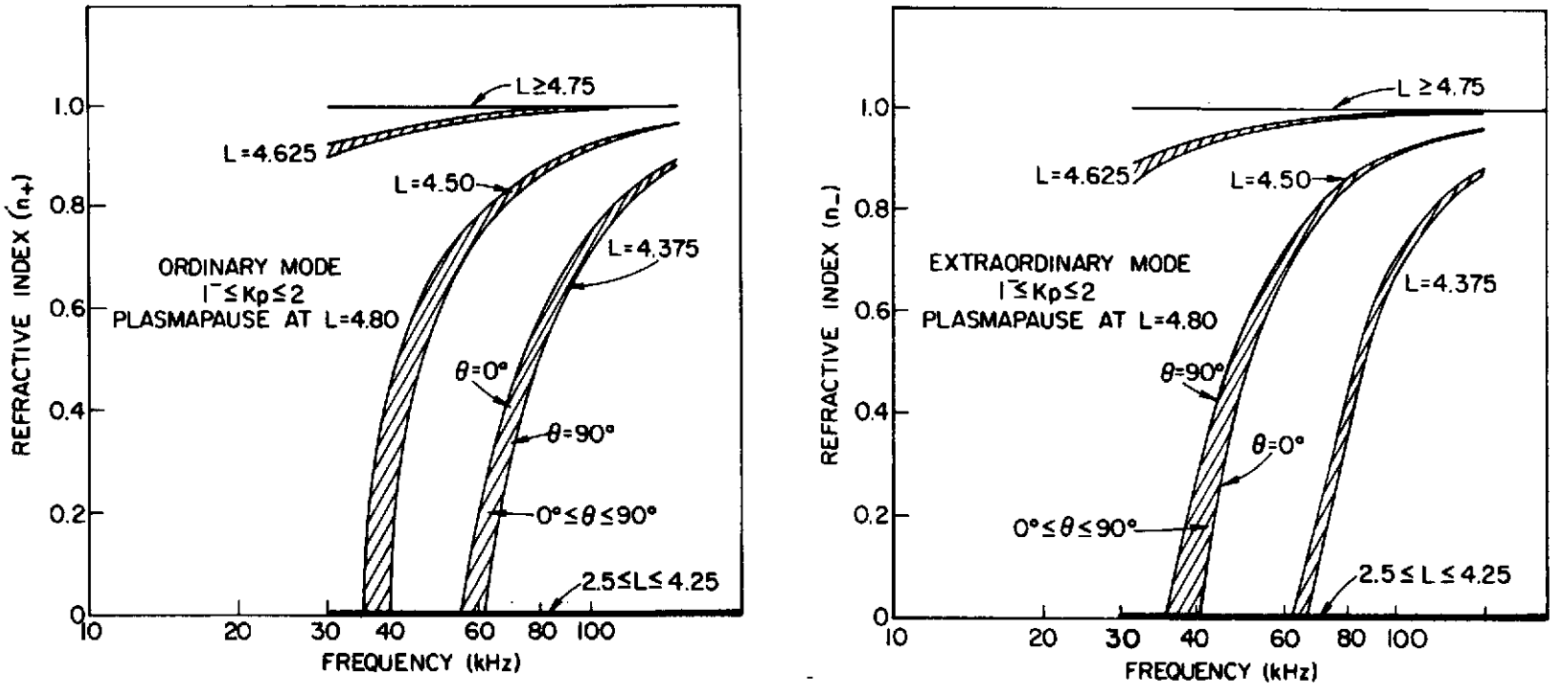

(a) (b)

Figure 2.11 a-f REFRACTIVE INDICES ($n_{\pm}$) VERSUS FREQUENCY, L, K_p AND THETA IN THE GEOMAGNETIC EQUATORIAL PLANE.

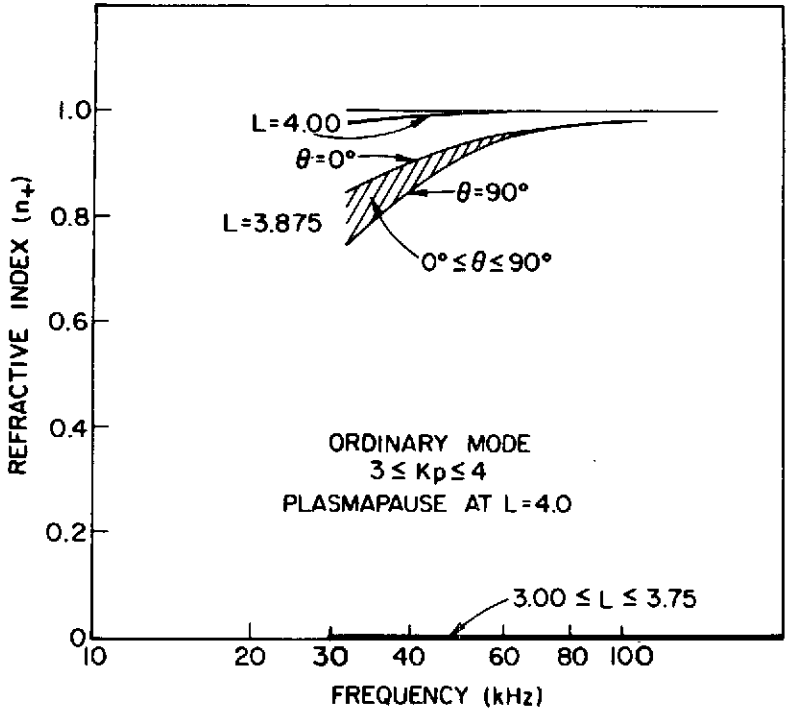

(c)

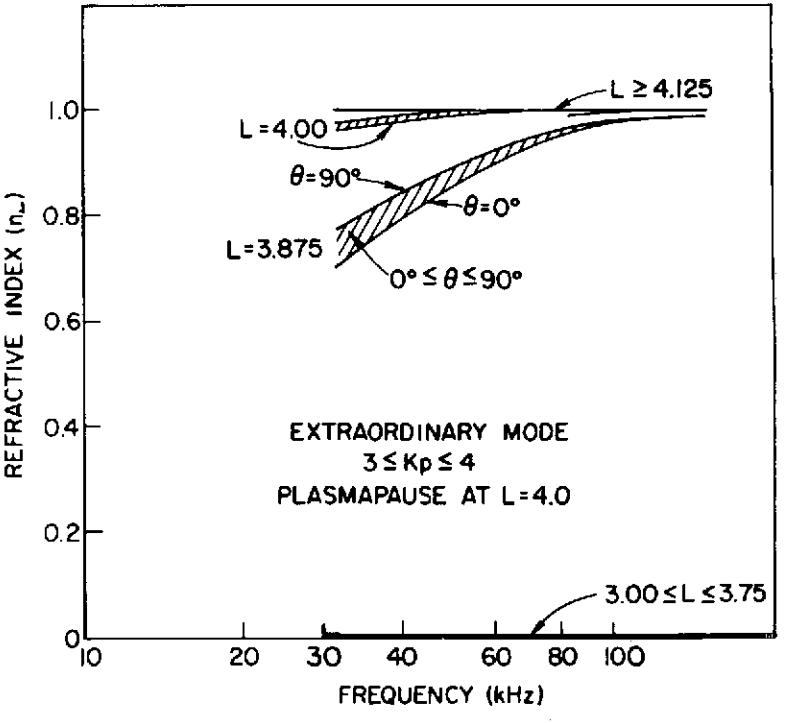

(d)

Figure 2.11 (continued)

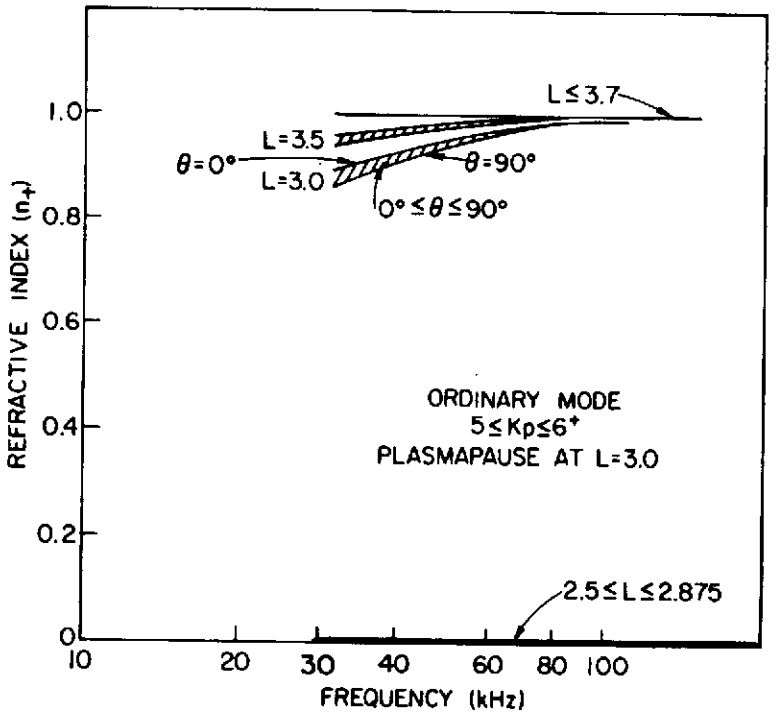

(e)

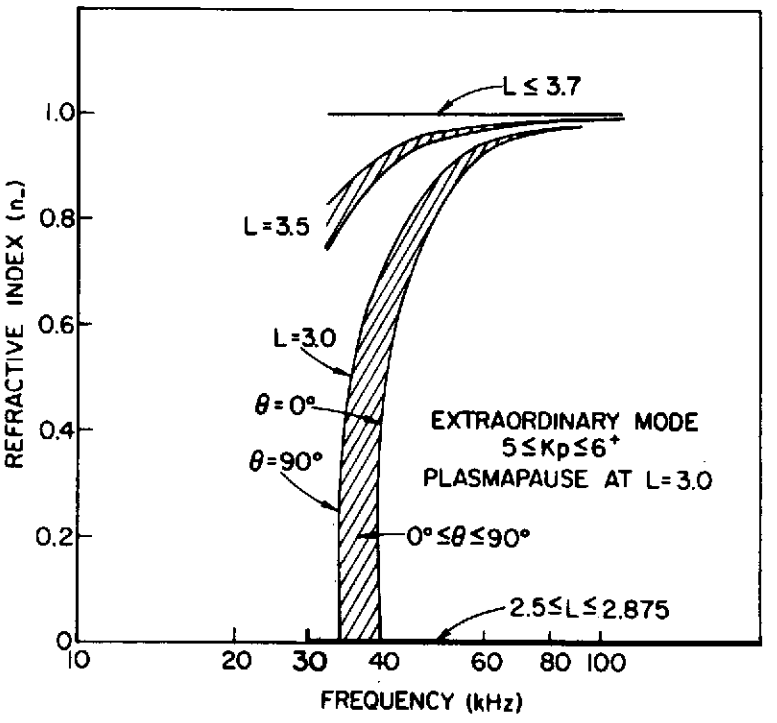

(f)

Figure 2.11 (continued)

along the field line. (This argument is based on the assumption that the frequency of observation is always greater than the upper hybrid frequency encountered along the field lines defining the plasmapause. This assumption will always be valid for regions in the magnetosphere from which appreciable radiation will be shown to emanate.) Consequently, for frequencies between 30 kHz and 300 kHz, radiation from within the plasmasphere will not reach an observer located in the interplanetary medium. The noise that would be received, therefore, comes from energetic particles located beyond the magnetic field line defining the plasmapause (i.e., primarily from the outer radiation belt electrons since the inner belt, located between $L = 1.1$ and $L \approx 2.0$, is found within the plasmasphere for $K_p < 6^+$: see Equation 2.2).

Figures 2.9 a-c, 2.10 a-c, and 2.11 a-c also show that the refractive indices (for 30 kHz $\leq f \leq$ 300 kHz) vary monotonically from zero to one over a very short distance as the plasmapause is traversed from the plasmasphere to the plasmatrough. The models of Chapter I proved that, for regions where $n_{\pm} < 1.0$, the power radiated by an electron is decreased below that which would be emitted if $n_{\pm} = 1.0$. It is therefore possible to limit this study to regions where $n_{\pm} > 0.1$ without introducing significant error in the final result. This statement is supported as follows. The segment of the magnetosphere, in which $0 \leq n_{\pm} \leq 0.1$, has a width of at most 0.125 earth radii (measured in the geomagnetic equatorial plane) while the overall emission region (where by definition $0.1 \leq n_{\pm} \leq 1.0$) has an extent of at least 2.5 earth radii. Thus, the calculations for the next chapter (see Section III.B) will show that the noise generated within the segment of the

magnetosphere adjacent to the plasmapause, is almost three orders of magnitude below that generated in the overall emission region; it can therefore be safely ignored.

H. Ray Path Calculations

For the frequency range 30 kHz to 300 kHz, the magnetospheric models valid for this study, and radio noise propagating in a region characterized by $0.1 \leq n_{\pm} \leq 1.0$, paragraph eight of I.B states that the transfer of radiation from the source to an observer can be calculated using the principles of geometric optics. That is, the magnetospheric noise received by an observer in the interplanetary medium can be calculated by determining the brightness received along ray paths that pass through the emission region and terminate at the observation point (see Figure 1.3). The calculations for these ray paths (referred to as raytracing) are greatly simplified by the following.

1. The ray path geometry is easier to compute if we assume the paths start at the observer (i.e., the observer is modeled as a transmitter) and pass through the magnetosphere. By the reciprocity theorem, these same paths would be obtained if they started in the magnetosphere and were traced to the observer. This latter approach, however, complicates the calculations unnecessarily.

2. Consider the ray paths of Figure 2.12, which are drawn in the geomagnetic equatorial plane. For points along the second path, before it hits the plasmapause, the refractive indices are approximately equal to unity (as shown in the preceding section). Therefore, the ray paths

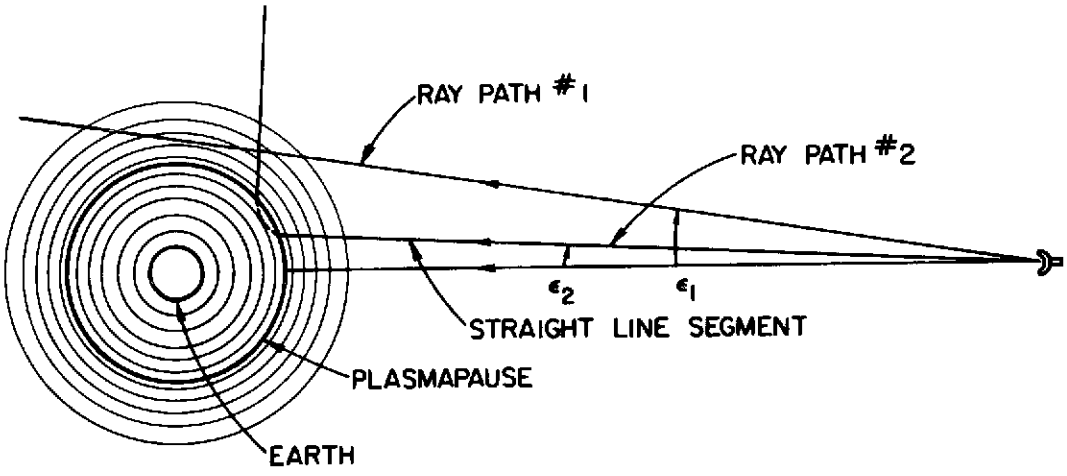

Figure 2.12 RAY PATH GEOMETRY IN THE GEOMAGNETIC EQUATORIAL PLANE FOR AN OBSERVER WHOSE GEOCENTRIC DISTANCE IS 32 EARTH RADII (not drawn to scale).

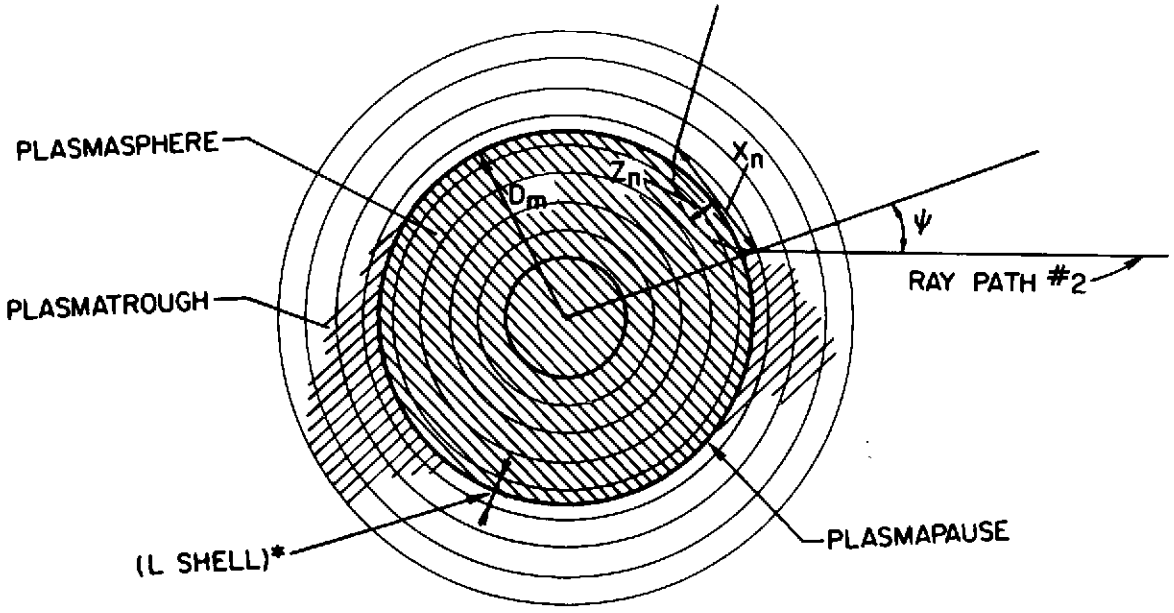

Figure 2.13 EXPANDED VERSION OF FIGURE 2.12. THIS FIGURE DEFINES THE RAY PATH GEOMETRY PERTINENT TO THIS STUDY.

can be taken as a straight line from the observer to approximately one L shell from the plasmapause.

3. As the ray approaches the plasmasphere, it encounters a medium in which the electron density increases rapidly in a direction toward the center of the earth. Furthermore, the rate of change of the electron density (and hence plasma frequency) is much greater than the rate of change of the electron gyrofrequency. This results in a decrease in magnitude for $n_{\pm}$, which is primarily due to the electron density gradient. Consequently, the magnetic field can be neglected in the ray path calculations.

4. Consider the geometry shown in Figure 2.13. Define the L shell which contains the plasmapause as (L shell)*. For a ray path hitting the plasmapause, the distance it penetrates the plasmasphere is designated as Z_m, and the distance from the ray entry point to the exit point from (L shell)* is X_m. Provided both X_m and Z_m are small compared to the distance (D_m) defined in the figure, the magnetosphere can be modeled as a plane (at the ray entry point) in which the thermal electron density increases linearly, with decreasing L, along the earth-observer line. Based on this model, it is possible to obtain explicit solutions for X_m and Z_m [Kelso, 1964] which are given by

$$Z_m = \frac{f^2 \cos^2 \Psi}{\eta A^2} \tag{2.9}$$

$$X_m = \frac{4f^2 \sin^2 \Psi \cos \Psi}{\eta A^2} \tag{2.10}$$

where

f = frequency of the electromagnetic wave propagating along the ray path (Hz)

A^2 = 80.6 meters^3 sec^{-2}

η = slope of the electron density profile (electrons m^{-1})

Ψ = angle of incidence of the ray path as defined in Figure 2.13.

Using these equations, X_m and Z_m were calculated for ray paths starting at the observer and passing through the three model magnetospheres developed in this chapter. In the worst case, where Z_m assumed its largest value, it was found that $Z_m \approx 640$ km. The value for X_m, however, increases as the ray path becomes tangent to (L shell)* (i.e., $\Psi \rightarrow 90^\circ$). If this case is neglected, by setting $\Psi \leq 80^\circ$, the worst case results in $X_m \approx 2800$ km. Since the corresponding value for D_m is approximately 32,000 km, the approximations used in calculating the ray paths (for $\Psi \leq 80^\circ$) are justified.

When $80^\circ < \Psi < 90^\circ$, trial calculations showed that the values obtained for X_m by Equation (2.10) were at most 10% less than those which would actually be obtained if a rigorous raytracing procedure were used. If this 10% discrepancy is accounted for in the next chapter, however, a change in calculated brightness of the magnetosphere of less than 1.0% would be obtained. This reduction in the percent error is due to the fact that X_m is always much less than the overall length of the ray path in the emission region; hence the integration of the emission coefficient $J(\ell)$ along each ray path

reduces the relative magnitude of this error. Since the 1.0% error in the brightness calculations is insignificant, the approximations for Z_m and X_m given by Equations (2.9) and (2.10) were used for obtaining all the ray paths.

Examples of the calculated ray paths (drawn to scale) are illustrated in Figures 2.14, 2.15 and 2.16 for the three K_p ranges discussed previously and for a frequency of 110 kHz. In each figure, two sets of drawings are given. One represents ray paths in the geomagnetic equatorial plane, and the second represents ray paths in the plane defined by the earth's dipole axis and a line drawn from the center of the earth to the observer. It should be noted that in this second set of drawings, a number of ray paths (particularly for $5 \leq K_p \leq 6^+$) were terminated before they traversed the entire magnetosphere. Such paths are those which come close to the earth's surface at large geomagnetic latitudes. They were truncated because they start to penetrate regions of high thermal electron densities and increased magnetic field strengths, which invalidate the simplifications listed above. Their termination, however, is not of major concern since, if these ray paths are extended, they continue through portions of the magnetosphere where the trapped energetic electron population is orders of magnitude less than that which exists along the segments of the paths drawn in these figures. The truncation of these paths will therefore introduce second order errors in the final results obtained in the next chapter. In fact, calculations in the next chapter will show that all ray paths could be terminated at a geomagnetic latitude of $\lambda_m = \pm 40^o$ (resulting

in the bounded emission region of Figure 1.1) without introducing significant error in the average brightness obtained for the magnetosphere.

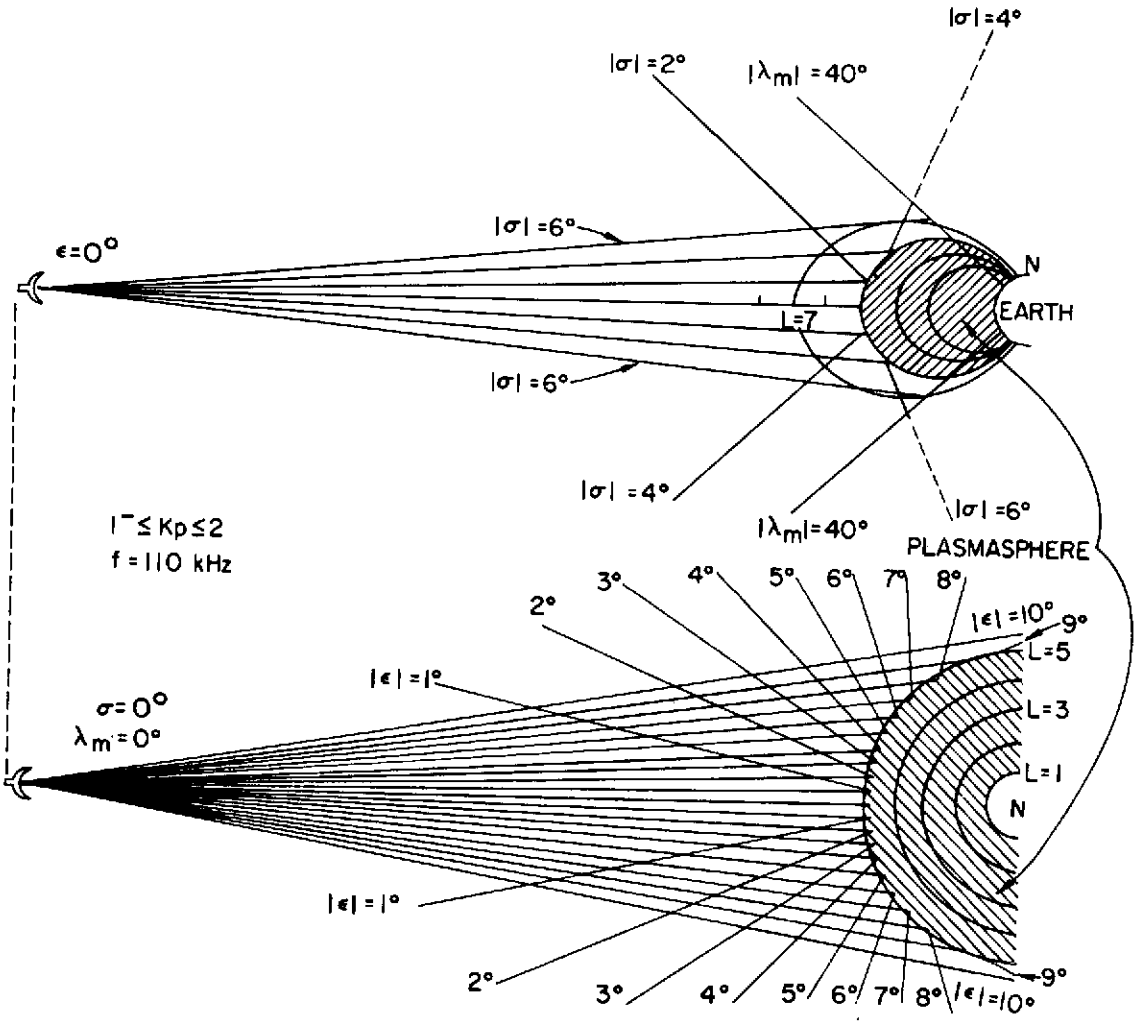

Figure 2.14 RAY PATHS CALCULATED IN THE O-A PLANE (DEFINED IN THE TEXT) AND THE GEOMAGNETIC EQUATORIAL PLANE FOR GEOMAGNETICALLY QUIET DAYS (drawn to scale). σ and ϵ are the observer look angle, subtended between the launch direction of a particular ray and the earth-observer line, projected onto the O-A plane and the geomagnetic plane respectively.

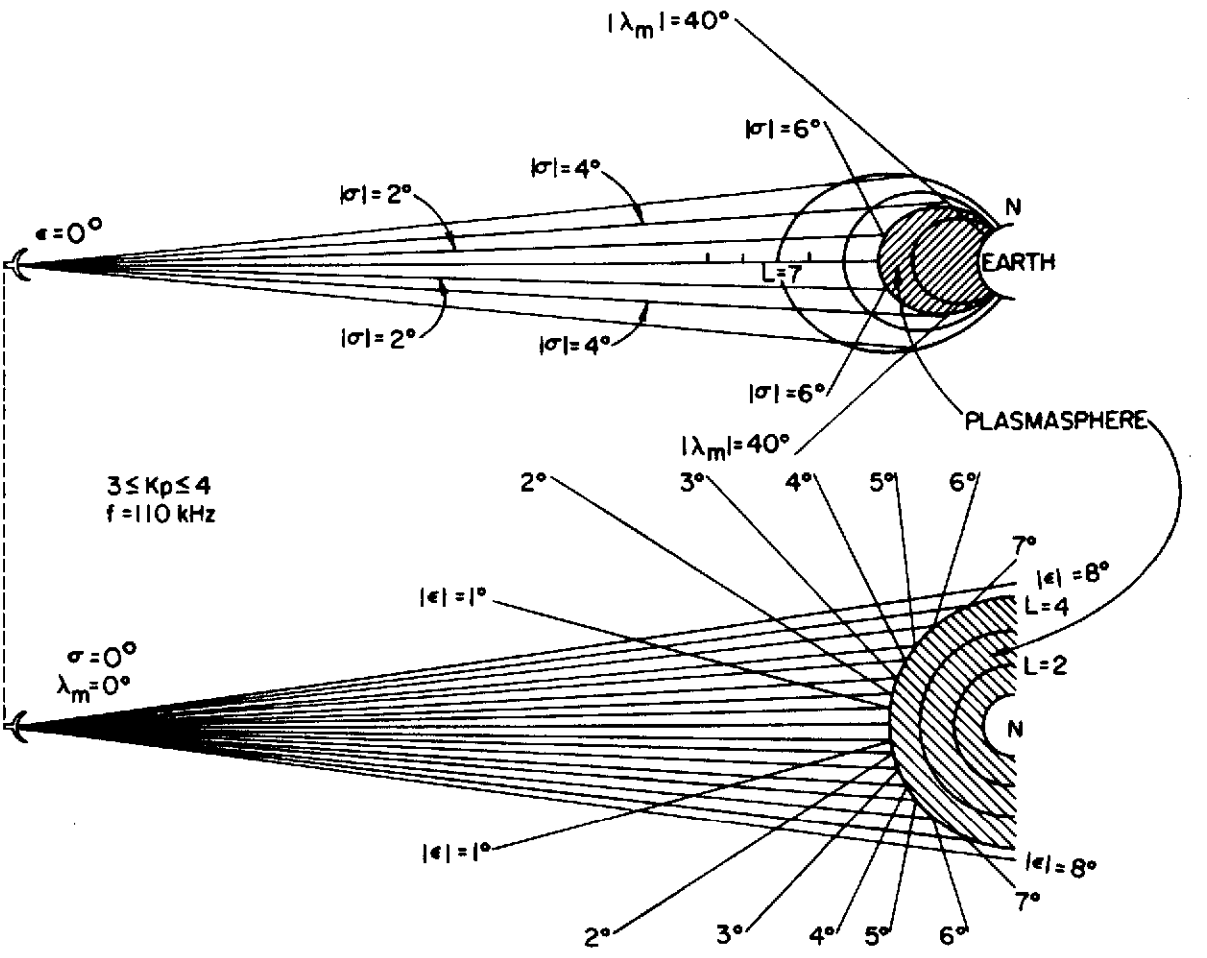

Figure 2.15 RAY PATHS CALCULATED IN THE O-A PLANE (DEFINED IN THE TEXT) AND THE GEOMAGNETIC EQUATORIAL PLANE DURING SUSTAINED GEOMAGNETIC ACTIVITY RESULTING IN $3 \leq K_p \leq 4$ (drawn to scale). σ and ϵ are the observer look angle, subtended between the launch direction of a particular ray and the earth-observer line, projected onto the O-A plane and the geomagnetic plane respectively.

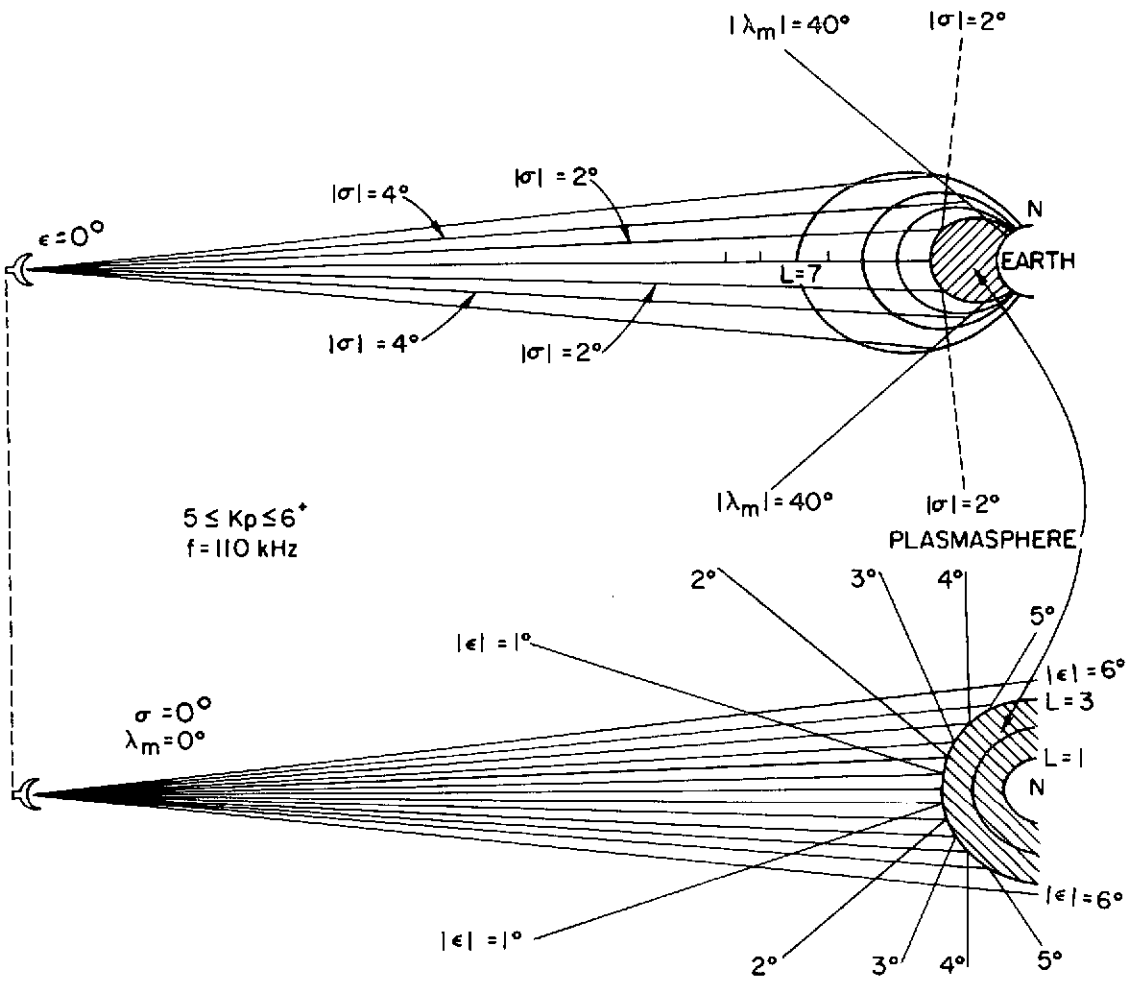

Figure 2.16 RAY PATHS CALCULATED IN THE O-A PLANE (DEFINED IN THE TEXT) AND THE GEOMAGNETIC EQUATORIAL PLANE DURING GEOMAGNETIC ACTIVITY RESULTING IN $5 \leq K_p \leq 6^+$ (drawn to scale). σ and ϵ are the observer look angle, subtended between the launch direction of a particular ray and the earth-observer line, projected onto the O-A plane and the geomagnetic plane respectively.

CHAPTER III

THEORETICAL CALCULATIONS

A. Introduction

Using the models given in the last two chapters, it is now possible to calculate the expected brightness of the earth's outer radiation belt due to gyro-synchrotron radiation. These calculations are made only for the extraordinary mode, since previous results showed that the power radiated into this mode is, in general, greater than or equal to that radiated into the ordinary mode, which will therefore not be discussed in this chapter.

Sections III.B through III.F neglect the bulge in the plasmapause and consider the case of an observer and ray paths located in the geomagnetic equatorial plane. The complete problem, in which these two restrictions are relaxed, is discussed in Section III.G, and the final results are then presented in III.H.

B. The Emission Coefficient, J(f)

The emission coefficient, as a function of K_p, was calculated using Equation (1.57) and the results are plotted in Figures 3.1 a-c. These figures show that, as the plasmapause is approached, radiation at the lower frequencies is greatly reduced from that which exists in the plasmatrough. This decrease in the emission is a result of the Razin effect discussed in Chapter I (i.e., $n_{\pm}(f) \rightarrow 0$, for all frequencies, as $L \rightarrow L_p$). It is interesting that the distance to the plasmapause, from the L shell in which J(f) begins to decrease, is directly related to the magnitude of K_p. This phenomenon is a result of the

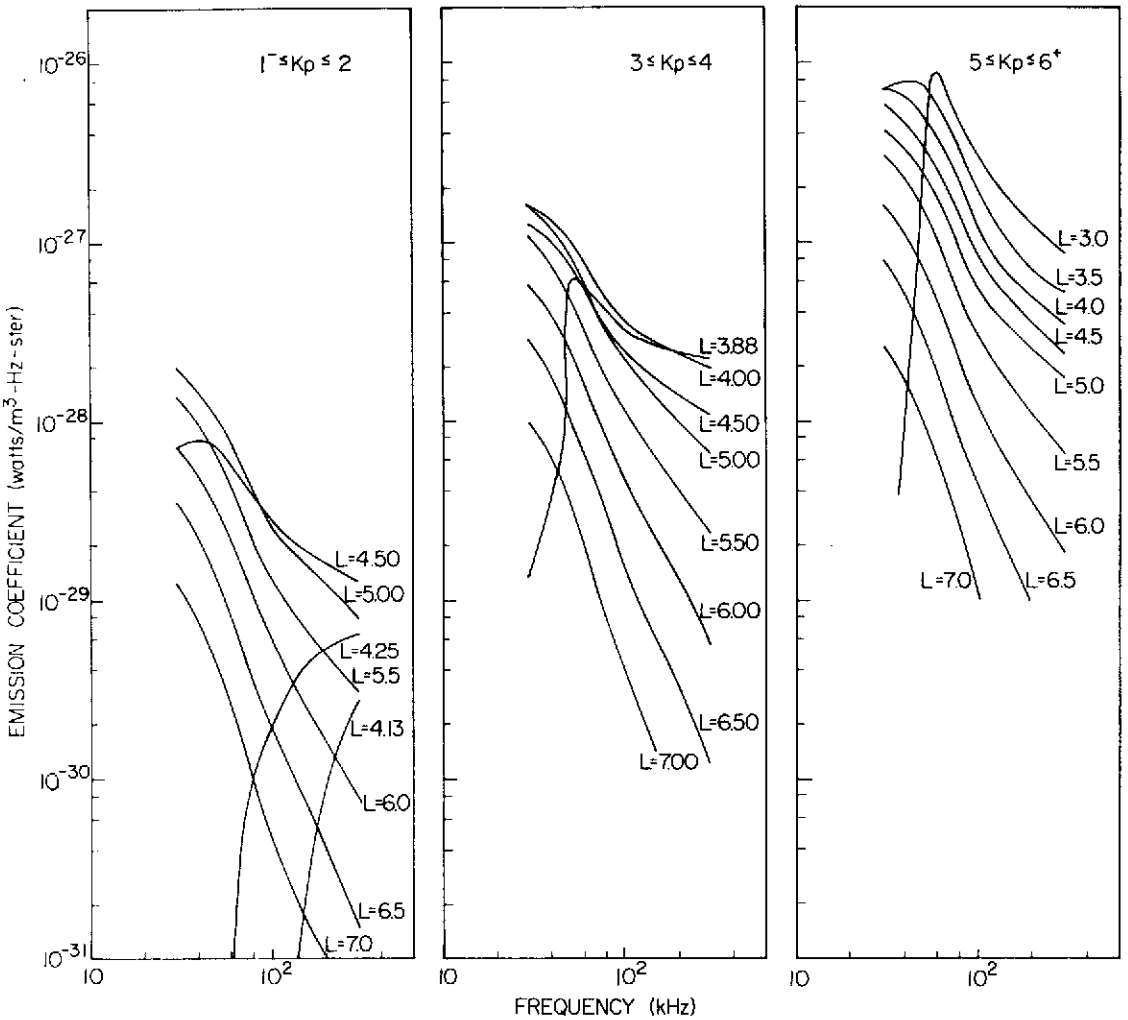

Figure 3.1 a-c THE EMISSION COEFFICIENT J(f) IN THE GEOMAGNETIC EQUATORIAL PLANE AS A FUNCTION OF FREQUENCY FOR VARIOUS L AND K_p VALUES.

increase in the thermal electron density gradient as K_p increases (see Figure 2.8). That is, as the density gradient increases, $n_{\pm}(f)$ goes from unity to zero over a shorter distance. The maximum value for this distance (measured from the plasmapause to the L shell in which the Razin effect, at any frequency, is negligible) occurs for $1^- \leq K_p \leq 2$, and is equal to approximately ΔL ($\Delta L = 0.125$ earth radii).

C. Path Lengths as a Function of Look Angle, ϵ

Figure 3.2 gives the length of the ray paths, within each L shell, as a function of the observer look angle (ϵ). This angle, shown in Figures 1.5 and 2.18, is defined as the one between the observation direction and the earth-observer line (i.e., each value of ϵ defines a particular ray path in the geomagnetic equatorial plane). The sudden increase in the path length, in each L shell, occurs when a ray passes tangential to that shell. This takes place, for an L shell given by $L = L^*$, when ϵ has the value

$$\epsilon^* = \sin^{-1}\left[\frac{L^* - 0.0625}{D_o}\right] \tag{3.1}$$

where

D_o = distance from the center of the earth to the observer located in the geomagnetic equatorial plane, measured in earth radii. ($D_o \approx 32$ earth radii in this study.)

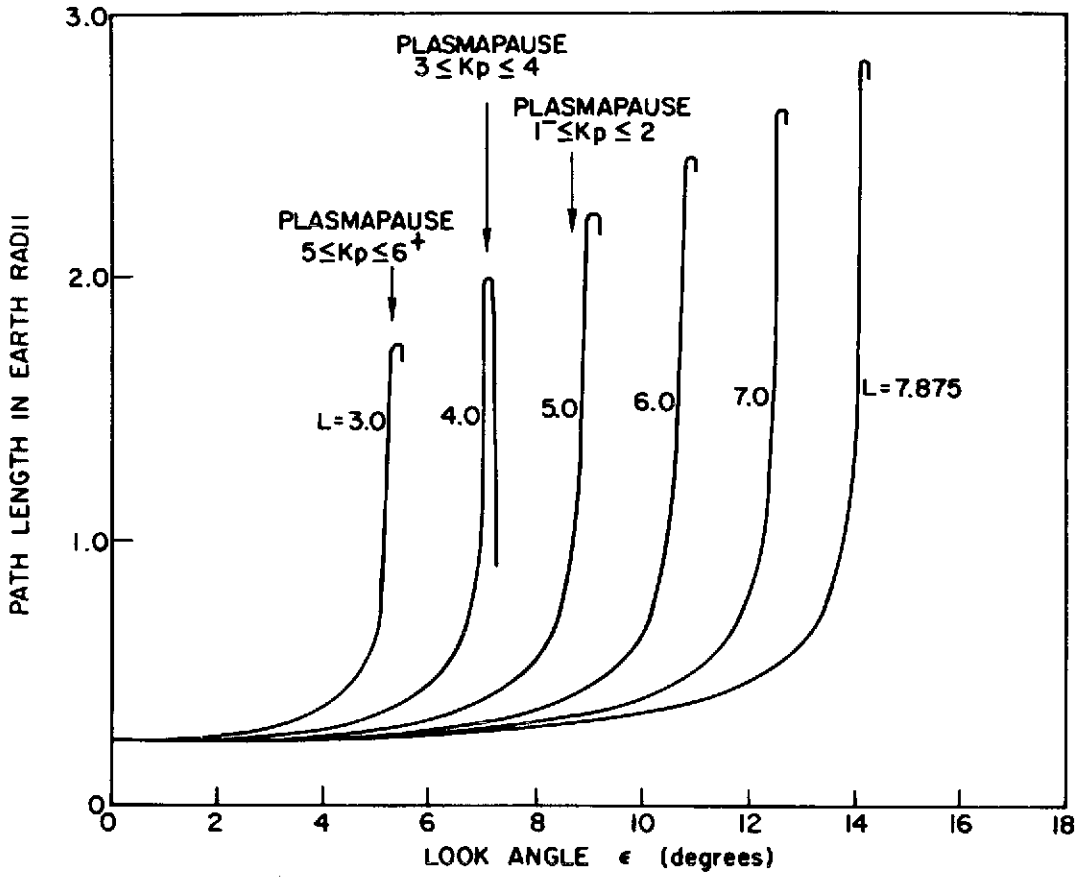

Figure 3.2 PATH LENGTHS IN THE GEOMAGNETIC EQUATORIAL PLANE (WITHIN A GIVEN L SHELL) AS A FUNCTION OF THE OBSERVER LOOK ANGLE.

As an example, for $K_p \geq 3$, the ray length in the L = 4.0 shell is 0.25 earth radii when $\epsilon = 0^o$, but increases to 2.0 earth radii for $\epsilon \approx 7^o$. When $K_p < 3$, however, the path length in this shell is zero since it is located within the plasmasphere, and ray paths for 30 kHz ≤ f ≤ 300 kHz were shown not to penetrate this portion of the magnetosphere. Thus, only path lengths in L shells, where L is greater than L_p (given by Equation (2.2)), have values other than zero.

This fact is shown in Figure 3.2 by the arrows, which indicate the location of the plasmapause as a function of K_p. For a given K_p range, shells to the left of each arrow are shielded from the observer, and hence do not contribute to the total length of any ray path that is calculated.

D. The Absorption Coefficient, K(f)

The next quantity to be considered is the absorption coefficient, which was calculated from Equation (1.61) for f = 30 kHz and the three K_p ranges previously defined. Since K(f) is proportional to the emission coefficient, which increases when the frequency decreases (see Figures 3.1 a-c), and is inversely proportional to the frequency squared, the choice of f = 30 kHz results in the maximum expected absorption of the radio noise for 30 kHz $\leq$ f $\leq$ 300 kHz. Therefore, K(f) = 30 kHz can be considered a worst case situation. Figure 3.3 gives the absorption, in dB per earth radius, for this frequency.

The dip in these absorption curves at $L \approx 4.5$ is a result of the slot region, which is located in the magnetosphere from $2.5 \lesssim L \lesssim 4.5$. Within this region, the decrease in the low energy electron fluxes (compared to $L \approx 5.0$) causes a decrease in the emission coefficient J(f) at low frequencies. (This result will be discussed in detail in Section III.F.) Due to the proportionality between K(f) and J(f), a similar reduction in K(f) is also observed. The dip in K(f) at $L \approx 4.5$, however, should not be confused with the abrupt cutoff in J(f), and hence K(f), caused by the Razin effect at low frequencies. (The subsequent rise in the absorption, when $L \rightarrow L_p$, is due to the

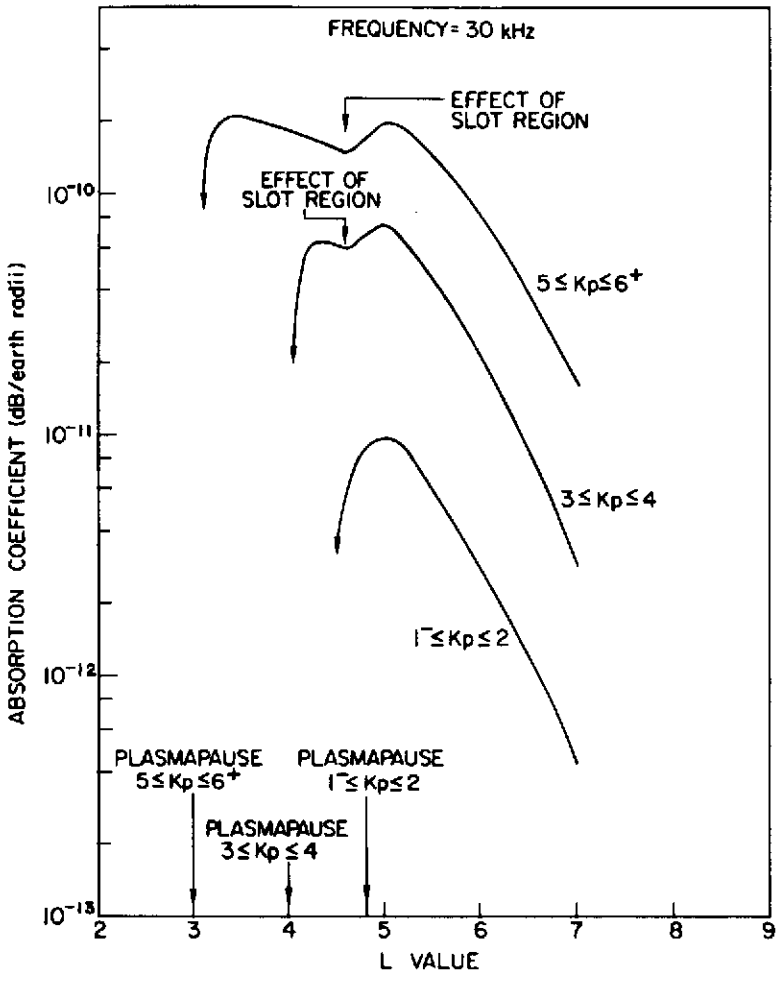

Figure 3.3 THE ABSORPTION COEFFICIENT K(f) IN THE GEOMAGNETIC EQUATORIAL PLANE AS A FUNCTION OF L FOR f=30 kHz AND VARIOUS K_p VALUES.

increase in the magnetic flux density (B), which causes a corresponding increase in J(f) and K(f)).

The results for K(f) in Figure 3.3 allow an important simplification to be made. Since the longest path length within any L shell is not more than 4 earth radii, the maximum possible attenuation suffered

by the radio noise propagating along any ray path (for f ≥ 30 kHz) is $\approx 4.0 \times 10^{-8}$ dB. The gyro-synchrotron self-absorption process, therefore, results in a decrease in the radiation of such small magnitude that it can be ignored in this study.

E. Brightness of the Outer Radiation Belt as a Function of K_p

The brightness observed along ray paths passing through the magnetosphere is derived from Equation (1.16). This equation, however, can be simplified on two accounts. First, the results of the last section showed that the absorption coefficient could be neglected (i.e., the optical depth (τ) is equal to zero). Second, the emission coefficient is appreciable only for L shells given by $L > L_p + 0.125$, where calculations give $0.1 \leq n_{\pm} \leq 1.0$ and $n_{r_{\pm}}^2 \approx n_{\pm}^2$. Thus Equation (1.16) reduces to

$$I(f) = \int_{\ell_o}^{\infty} \frac{J(f,\ell)}{n_{\pm}^2(f,\ell)}\, d\ell = \sum_{L_{min}}^{L_{max}} \frac{J(f,\ell)}{n_{\pm}^2(f,\ell)}\, \Delta L \qquad (3.2)$$

This expression was evaluated as a function of look angle (ε); the results for f = 30 kHz, 92 kHz and 300 kHz are given in Figures 3.4 a-c. These figures illustrate the following general characteristics for I(f).

1. A peak in the calculated brightness occurs for the path passing tangential to the L shell given by $L_1 = L_p + 0.0625$ (i.e., this path is defined by $\varepsilon_1 = \sin^{-1}[L_1/D_o]$), and the maximum is at least 6 dB greater than the brightness observed along the paths defined

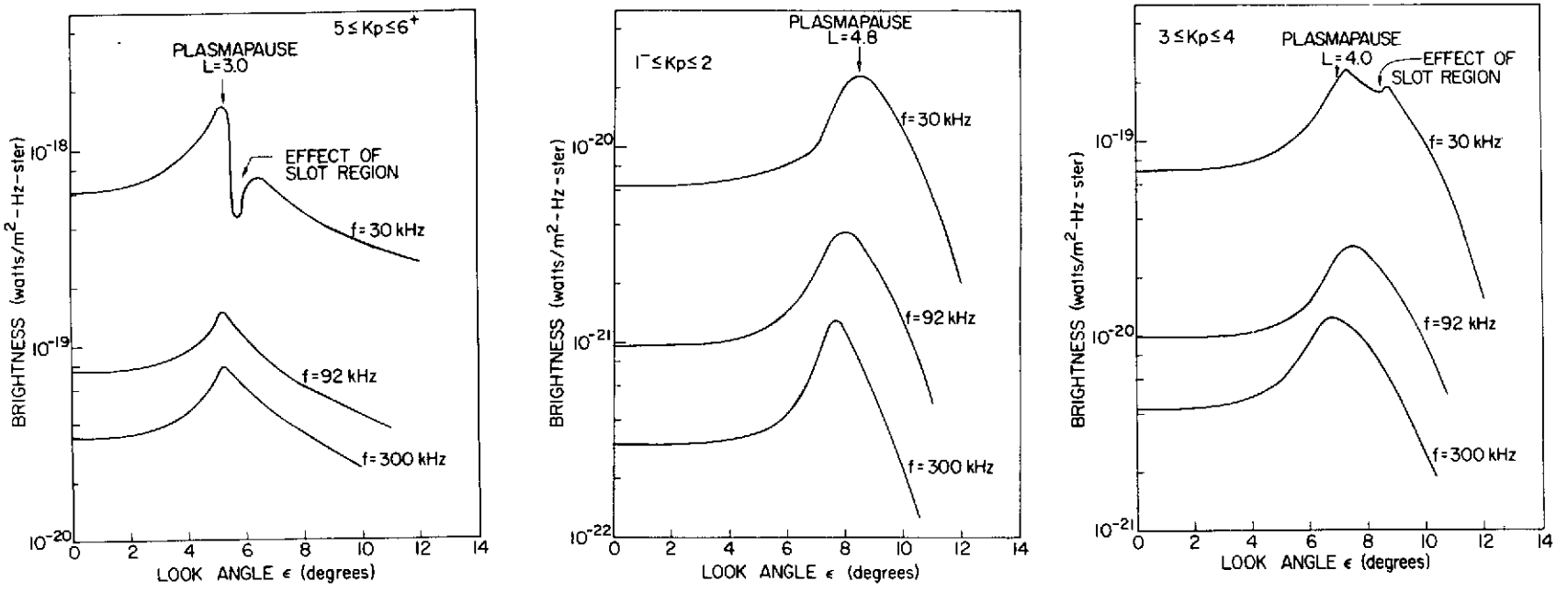

(a) (b) (c)

Figure 3.4 a-c BRIGHTNESS OBSERVED ALONG RAY PATHS PASSING THROUGH THE EARTH'S MAGNETOSPHERE, IN THE GEOMAGNETIC EQUATORIAL PLANE. EACH VALUE OF ϵ SPECIFIES A PARTICULAR RAY PATH IN THIS PLANE.

by $\epsilon = 0^{o}$. This maximum in I(f) is a result of the following. For $\epsilon < \epsilon_1$, the ray lengths within each L shell are less than the corresponding lengths for the path given by ϵ_1. For paths given by $\epsilon > \epsilon_1$, the number of shells traversed by these rays is less than that traversed by the path given by $\epsilon = \epsilon_1$. Thus, the path defined by $\epsilon = \epsilon_1$ has the longest lengths within each shell while still traversing the maximum number of L shells, and the maximum brightness is consequently observed in its direction.

2. For the lower frequencies and $K_p \geq 3$, there exists a dip in the calculated brightness at $L \approx L_p + 0.25$. This decrease in I(f) can be explained by considering the trapped electron model of Section II.B.3. In this model, the particle fluxes for 100 kev $\leq E \leq$ 700 kev within the slot region, are three to four times less than the corresponding fluxes at $L \approx 5.0$, while the higher energy fluxes are the same in both regions. Now, as shown in the next section, low frequency noise is generated predominantly by low energy electrons, and the high frequency noise ($f > 92$ kHz) is generated by high energy electrons ($E > 600$ kev). Thus, consider two ray paths, one passing through the slot region ($L \approx 4.5$), the second passing through the heart of the outer electron belt ($L \approx 5.0$). From the above discussion it is apparent that the second path will have a greater brightness at low frequencies than the first, but both will be of comparable brightness at the higher frequencies (i.e., the dip does not appear for these frequencies). The decrease and subsequent increase (as L increases) in the brightness curves for f = 30 kHz is a consequence of the electron fluxes in the slot region, which emit detectable radiation when $K_p > 3$. (Note

that this effect is not observed for $1^- \leq K_p \leq 2$ since for this case the slot region is located within the plasmasphere.) The relative size of the dip is also positively correlated to K_p, which is due to a larger portion of the slot region being exposed as K_p increases.

3. Define the half power angular extent of the emission region, at a frequency f, by $\epsilon_{max}(f)$, where $I(\epsilon_{max},f) = 0.5[I(\epsilon = 0^o,f)]$. Assume also that for $\epsilon > \epsilon_{max}$, $I(\epsilon,f) = 0.0$. (The definition and the assumption simplify the analysis to follow and introduce no more than 10% error in the final results.) Then, Figures 3.4 a-c show that $\epsilon_{max}(f)$ decreases slightly as f increases. That is, the emission regions are confined to segments of the magnetosphere whose outer boundary is progressively closer to the earth as the observation frequency increases.

This relationship between $\epsilon_{max}(f)$ and f is due to a monotonic increase in $|d[\log I(f)]/d[\log f]|$ as both f and L increase. The increase in $|d[\log I(f)]/d[\log f]|$, in turn, is a consequence of the decrease in the magnetic flux density and the softening of the electron flux spectrums as one moves away from the earth (see Figure 2.2b).

F. The Range of Electron Energies and Harmonic Numbers which Contribute Radiation at a Given Observation Frequency

Equation (1.56) shows that, within a given L shell, the emission coefficient J(f) is obtained by performing a summation over harmonic numbers (s). That is, to calculate J(f), s is stepped from unity to 'infinity', and the radiation from electrons, whose energies are determined by the harmonic number and frequency of observation, is

summed. (Recall the discussion in Section I.E on the Dirac delta function in this equation. This function implicitly gives the energy of the electrons which radiate at a frequency f once s, the positional geometry of the observer relative to the earth, and an L shell are specified.) It is therefore possible to calculate the ratio, for each L shell, of the power radiated at a frequency (f) and harmonic (s) (and hence from electrons of discrete energy (E)) to the total emission coefficient J(f) for that shell. The results of these calculations, expressed as a percentage of J(f), are given in Figures 3.5 a-c and 3.6 a-c for $3 \leq K_p \leq 4$.

From the discussion of the preceding paragraph, it is evident that the plots given in these figures should not be continuous, but should have data only at integral values of s and discrete values of E. The intention of this section, however, is to show clearly the relationship between J(f) and these two quantities. Therefore, the envelopes of these discrete plots are given.

These figures illustrate that within each L shell the emission coefficient at low frequencies results from low harmonic numbers and electron energies. Furthermore, as the frequency of observation (f) increases, both the range of harmonic numbers and electron energies which account for the radiation at f also increase.

Thus, consider the ray path defined by $\epsilon = 0^{o}$ in the geomagnetic equatorial plane. The brightness I(f) observed along this path is obtained by summing J(f) for each L shell the ray traverses and multiplying the total by a constant. From the results given in Figures 3.5a and 3.6a it can be concluded that for f = 30 kHz, 70% of the brightness observed along this path is generated by electrons

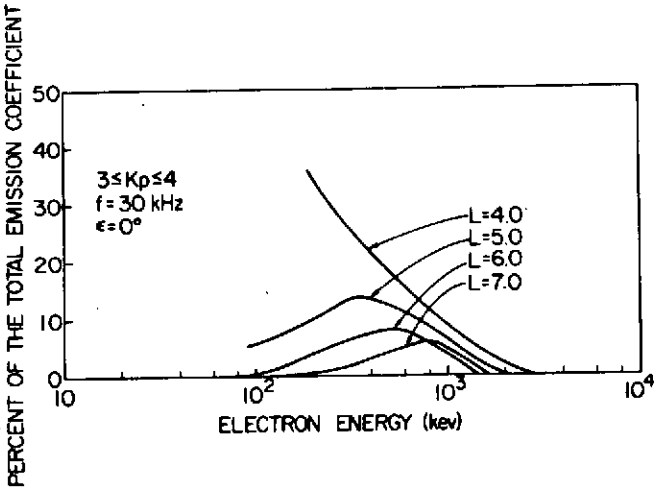

(a)

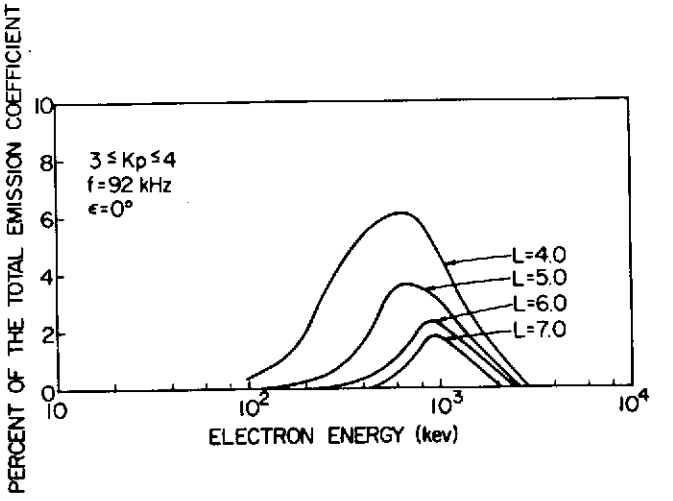

(b)

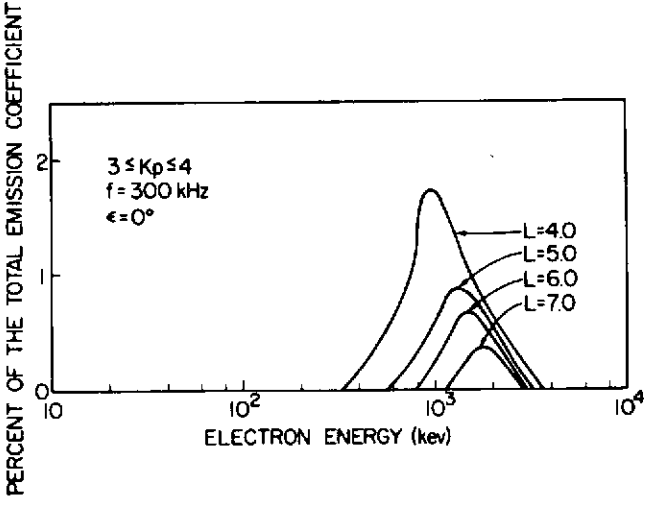

(c)

Figure 3.5 a-c PERCENT OF THE TOTAL EMISSION COEFFICIENT J(f) (FOR GIVEN FREQUENCIES) AS A FUNCTION OF ELECTRON ENERGY FOR VARIOUS L VALUES.

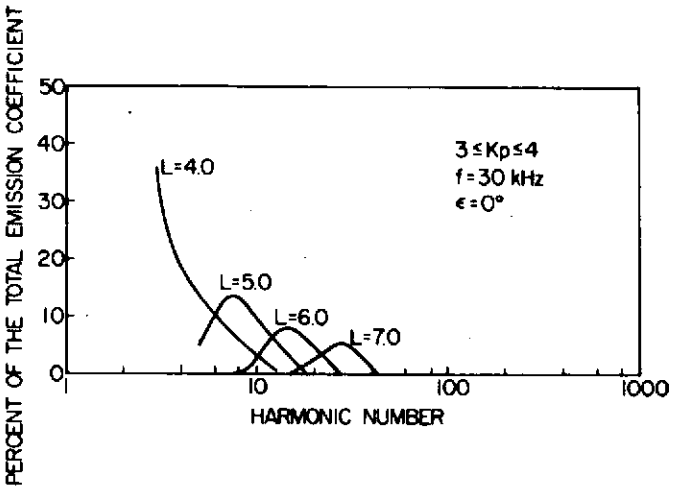

(a)

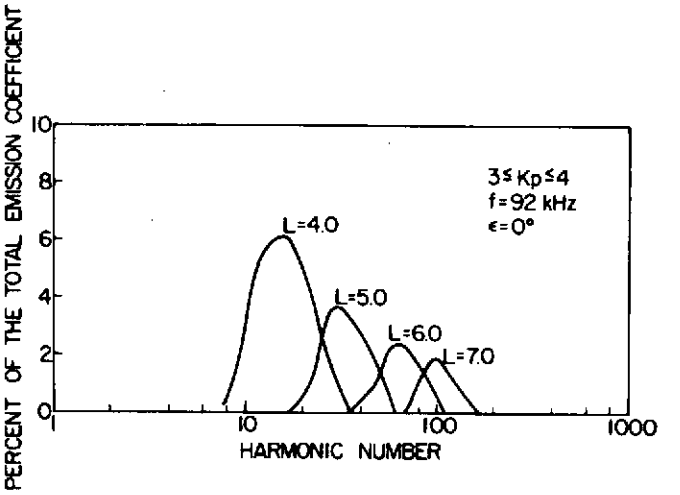

(b)

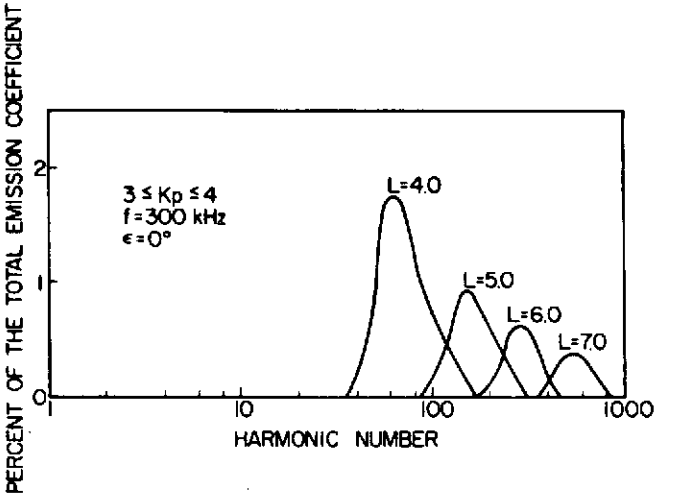

(c)

Figure 3.6 a-c PERCENT OF THE TOTAL EMISSION COEFFICIENT J(f) (FOR GIVEN FREQUENCIES) AS A FUNCTION OF HARMONIC NUMBER FOR VARIOUS L VALUES.

with 100 kev $\lesssim$ E $\lesssim$ 500 kev and from harmonic numbers $3 \lesssim s \lesssim 20$. For f = 300 kHz, 70% to 80% of the brightness is accounted for by electrons with 600 kev $\lesssim$ E $\lesssim$ 3 Mev and $50 \lesssim s \lesssim 600$.

This qualitative relationship between the electron energies, harmonic numbers, and frequency of observation was found to hold for each K_p range over the entire emission region. Consequently, if the gyro-synchrotron noise from the outer radiation belt can be observed, appropriate calculations should give an estimate of the density and energy spectrum (integrated over the emission region) of the electrons which radiate the power. For a study of this nature to be feasible, however, it must first be determined if the noise is sufficiently intense to be detected. Since this question is considered in Chapter V, further discussion of the results of this section will be postponed until that time.

G. The Brightness Observed along Ray Paths off the Geomagnetic Equatorial Plane

The calculations for the brightness observed along ray paths off the geomagnetic equatorial plane are more complicated than those of the preceding sections. The difficulties arise from the variation of the magnetic flux density (B), observation angle (θ), and the particle fluxes along segments of a ray path within a given L shell. (In the geomagnetic equatorial plane these quantities are constant within each L shell.) The analysis of this section can be simplified, however, by considering ray paths in the plane defined by the earth-observer line and the geomagnetic dipole axis (henceforth referred to as the O-A

plane). Limiting the rays to this plane reduces the problem from three dimensions to two dimensions, but still allows an accurate value for the average brightness of the magnetosphere (defined in Section III.G.3) to be calculated.

1. Before calculating the average brightness $I_{av}(f)$ it is necessary to obtain the angular extent of the emission region as a function of frequency and K_p in the O-A plane. This bound is determined in a manner similar to that used for deriving $\epsilon_{max}(f)$ in Section III.E.3. In this case, define $\sigma_{max}(f)$ as the angle which gives the ray path in the O-A plane where $I(\sigma_{max},f) = 0.5[I(\sigma = 0^{o},f)]$. (Note that the path given by $\sigma = 0^{o}$ in this plane is the same as the one defined by $\epsilon = 0^{o}$ in the geomagnetic equatorial plane.) Using this definition, the values of $\sigma_{max}(f)$ were calculated as a function of K_p and are given in Table 2 of Section III.G.

The results for $\sigma_{max}(f)$ show that, as f increases, there is a substantial decrease in the angular extent of the emission region in the O-A plane, contrary to the results obtained for $\epsilon_{max}(f)$. (Compare $\sigma_{max}(f)$ and $\epsilon_{max}(f)$ in Table 2.) This characteristic of $\sigma_{max}(f)$ is explained by recalling the relationship established between the frequency of observation (f) and the range of harmonic numbers and electron energies which account for the radiation at f. To be more precise, Figure 1.10 illustrates that at low harmonic numbers, the power radiated by electrons with small pitch angles is appreciable (i.e., within a factor of one-half) compared to the power radiated by an electron of the same energy with $\alpha = 90^{o}$. Furthermore, the magnetic flux density (B) increases (Equation 2.7) as $|\lambda_m|$ increases from zero.

Thus, the radio noise observed at low frequencies along ray paths in the O-A plane comes from harmonic numbers lower than those which account for the noise emanating from the geomagnetic equatorial plane. (The radiation observed at low frequencies along ray paths in the O-A plane results from very low harmonic numbers ($1 \leq s < 10$) and hence is generated predominantly by the cyclotron emission process.)

For these low harmonic numbers, Figures 1.10 and 1.7-1.9 show that appreciable power can be radiated by electrons with $10^{o} \leq \alpha \leq 90^{o}$ at angles θ close to zero degrees. Thus, because low frequencies are generated at low harmonic numbers, appreciable power at these frequencies will be radiated along ray paths which pass nearly tangential to the field lines $5 \leq L \leq 7$ in the O-A plane. In particular, the brightness observed at f = 30 kHz along ray paths passing tangential to the shells $6.5 < L < 7$ (i.e., $\sigma_{max}(f=30 \text{ kHz}) \approx 7^{o}$) is within 50% of the brightness observed along the path $\sigma = \epsilon = 0^{o}$ at this frequency.

For the higher frequencies, however, the situation changes drastically. If we consider radiation at f = 300 kHz, the noise is emitted from high energy electrons, $E \gtrsim 600$ kev, at harmonic numbers close to s_{pk} (i.e., mainly by a synchrotron emission process), where s_{pk} is defined in Section I.D.1. As illustrated in Figure 1.10, the power radiated by a particle with $\alpha = 90^{o}$, at $s = s_{pk}(\alpha = 90^{o})$, is much greater than that radiated by a particle of the same energy at the same harmonic number (and hence frequency), but with $\alpha < 70^{o}$. Furthermore, the beamwidth of the radiation at the higher frequencies is much less than that of the lower harmonics (see Figures 1.7 - 1.16). Therefore, contrary to the results for f = 30 kHz, appreciable power at f = 300 kHz

is obtained only along ray paths which make angles less than 30^{o} with the normals to the field line L = 5.0 in the O-A plane. (This geometry results in electrons, with $70^{o} < \alpha < 90^{o}$, emitting radiation directly toward the observer along these paths.) For a spacecraft located at 2.04×10^{5} km from earth in the geomagnetic equatorial plane this gives a σ_{max}(f = 300 kHz) of 2.0^{o}. The consistent decrease in σ_{max}(f) as f increases is, then, a result of the emission process going from cyclotron at low frequencies to gyro-synchrotron at intermediate frequencies and, finally, to synchrotron at high frequencies.

2. The calculations for σ_{max}(f) and for I(f) observed along ray paths in the O-A plane showed that the line integral of Equation (3.2) could be limited to segments of the ray paths located in the portion of the magnetosphere bounded by $|\lambda| \leq 40^{o}$. Truncating the paths in this manner simplified the analysis of this section, while introducing at most a 10% decrease in the results obtained for I_{av}(f) in III.G.3, an error which was felt to be insignificant.

3. Using the results of preceding sections, it is now possible to consider the effects of the bulge in the plasmapause on the observed brightness. To this end, define the average brightness of the magnetosphere I_{av}(f) as [Kraus, 1966]

$$I_{av}(f) = \frac{1}{\Omega_{s}(f, K_{p})} \iint I(\sigma, \varepsilon)\, d\Omega \qquad (3.3)$$

and

$$\Omega_s(f,K_p) = \frac{(2\sigma)(2\epsilon)}{3282} \tag{3.4}$$

where

$I(\sigma,\epsilon)$ = brightness observed along the ray path given by angles σ and ϵ.

$d\Omega$ = element of solid angle subtended by the source at the observer.

$\Omega_s(f,K_p)$ = solid angle subtended by the source at the observer.

The quantity, 3282, converts degrees squared to steradians. The factors of two included with ϵ and σ account for the symmetry of the source region (when the bulge is neglected) in both the O-A plane and the geomagnetic equatorial plane. Using these equations, $I_{av}(f)$ was calculated as a function of K_p, and the results are given in Table 2.

Since the bulge in the plasmapause is much more evident during geomagnetically disturbed periods (i.e., when the plasmapause, in the local time zone 2100 to 1800 hr, is compressed to $L < 5$), the discussion in this section shall be focused primarily on times when $5 \leq K_p \leq 6^+$. For this K_p range, the bulge will have its maximum effect on the observed brightness when it is located on the earth's limb (as seen by the observer in the interplanetary medium). That is, at this location the bulge will shield the largest fraction of the emission region from the observer.

To determine the fraction which cannot emit radiation toward the

Table 2

SUMMARY OF RESULTS OBTAINED IN SECTIONS III.E.3, G.1, AND G.2

Frequency (kHz)	K_p Range	ϵ_{max} (f) (deg)	σ_{max} (f) (deg)	Ω_s (f,K_p) (ster)	I_{ay} (f) (watts/m^2-Hz-ster)
30	$1^- \leq K_p \leq 2$	11.8	7.0	0.100	5.5×10^{-21}
	$3 \leq K_p \leq 4$	11.4	6.9	1.096	6.5×10^{-20}
	$5 \leq K_p \leq 6^+$	10.8	6.7	0.090	5.3×10^{-19}
44	$1^- \leq K_p \leq 2$	11.6	4.5	0.064	2.6×10^{-21}
	$3 \leq K_p \leq 4$	11.3	4.4	0.061	3.1×10^{-20}
	$5 \leq K_p \leq 6^+$	10.7	4.3	0.056	2.5×10^{-19}
55	$1^- \leq K_p \leq 2$	11.4	3.5	0.049	2.2×10^{-21}
	$3 \leq K_p \leq 4$	11.2	3.5	0.049	2.3×10^{-20}
	$5 \leq K_p \leq 6^+$	10.7	3.2	0.042	2.1×10^{-19}
67	$1^- \leq K_p \leq 2$	11.3	3.3	0.045	1.6×10^{-21}
	$3 \leq K_p \leq 4$	11.0	3.2	0.043	1.8×10^{-20}
	$5 \leq K_p \leq 6^+$	10.7	3.1	0.041	1.3×10^{-19}
83	$1^- \leq K_p \leq 2$	11.1	2.9	0.039	9.4×10^{-22}
	$3 \leq K_p \leq 4$	10.9	2.7	0.036	1.1×10^{-20}
	$5 \leq K_p \leq 6^+$	10.8	2.5	0.033	7.7×10^{-20}
92	$1^- \leq K_p \leq 2$	11.0	2.7	0.036	8.3×10^{-22}
	$3 \leq K_p \leq 4$	10.8	2.5	0.033	1.0×10^{-20}
	$5 \leq K_p \leq 6^+$	10.8	2.4	0.032	6.6×10^{-20}
110	$1^- \leq K_p \leq 2$	10.8	2.5	0.033	6.5×10^{-22}
	$3 \leq K_p \leq 4$	10.6	2.3	0.030	8.3×10^{-21}
	$5 \leq K_p \leq 6^+$	10.7	2.2	0.029	5.4×10^{-20}

Table 2

CONTINUED

Frequency	K_p Range	ϵ	σ	Ω_s	I_{av}
150	$1^- \leq K_p \leq 2$	10.7	2.3	0.030	4.6×10^{-22}
	$3 \leq K_p \leq 4$	10.5	2.2	0.028	5.5×10^{-21}
	$5 \leq K_p \leq 6^+$	10.6	2.1	0.027	3.8×10^{-20}
200	$1 \leq K_p \leq 2$	10.5	2.1	0.028	3.2×10^{-22}
	$3 \leq K_p \leq 4$	10.4	2.0	0.025	4.0×10^{-21}
	$5 \leq K_p \leq 6^+$	10.7	1.8	0.023	3.1×10^{-20}
250	$1^- \leq K_p \leq 2$	10.5	2.1	0.027	2.9×10^{-22}
	$3 \leq K_p \leq 4$	10.3	1.9	0.024	3.7×10^{-21}
	$5 \leq K_p \leq 6^+$	10.6	1.8	0.023	2.6×10^{-20}
300	$1^- \leq K_p \leq 2$	10.5	2.1	0.027	2.6×10^{-22}
	$3 \leq K_p \leq 4$	10.3	2.0	0.025	3.0×10^{-21}
	$5 \leq K_p \leq 6^+$	10.6	1.8	0.023	2.5×10^{-20}

observer, we note that the bulge extends to $L \approx 5.0$ in the 1800 to 2100 hr local time zone (see Section II.C). However, if we assume as a first approximation that it extends to $L = 7.0$ in this time zone, it is evident that the power radiated in one-half of the solid angle $\Omega_s(f,K_p)$ would be reduced to zero. Consequently, the average brightness would be decreased by 50%.

To improve on this first estimate for the decrease in $I_{av}(f)$, it should be noted that at least 30% of the power radiated in the geomagnetic equatorial plane (when $5 \leq K_p \leq 6^+$) comes from the region $5 \leq L \leq 7$ (see Figures 3.4 a-c). Thus the decrease in $I_{av}(f)$ will, in reality, be no more than 35% (i.e., 1.9 dB). Since this decrease in

the average brightness is well within the approximations used throughout the analysis presented thus far, it is concluded that the bulge in the plasmapause can be neglected in this study.

H. The Average Calculated Spectrums of the Radio Noise Generated in the Earth's Outer Radiation Belt

The values for $I_{av}(f)$ given in the last column of Table 2 have been plotted in Figures 3.7 a-c to illustrate the spectrums calculated for the gyro-synchrotron radio noise. Two important aspects of these figures are discussed below.

1. Each spectrum can be approximated by two straight lines, one for 30 kHz $\leq$ f $\leq$ 92 kHz and one for 110 kHz $\leq$ f $\leq$ 300 kHz, which differ by a factor of approximately two in their slopes. In Section III.G.1, we showed that, for a frequency (f), the noise is emitted by electrons with $\alpha_1 \leq \alpha \leq 90^\circ$, where α_1 decreases monotonically as f increases. (Recall that $\alpha_1 \approx 10^\circ$ for f = 30 kHz and increases to $\alpha_1 \gtrsim 70^\circ$ for f > 110 kHz.) Since the number of particles of energy E radiating at a given frequency along the direction of observation is given approximately by (Section I.F)

$$N(E) = 2\pi \int_{\alpha_1}^{90^\circ} N(E,\alpha) \sin \alpha \; d\alpha \qquad (3.5)$$

N(E) also decreases as (f) increases. The magnitude of $|d[\log N(E)]/d[\log f]|$, however, is less for f $\geq$ 110 kHz than for 30 kHz $\leq$ f $\leq$ 110 kHz (i.e., the emission process changes rapidly from cyclotron

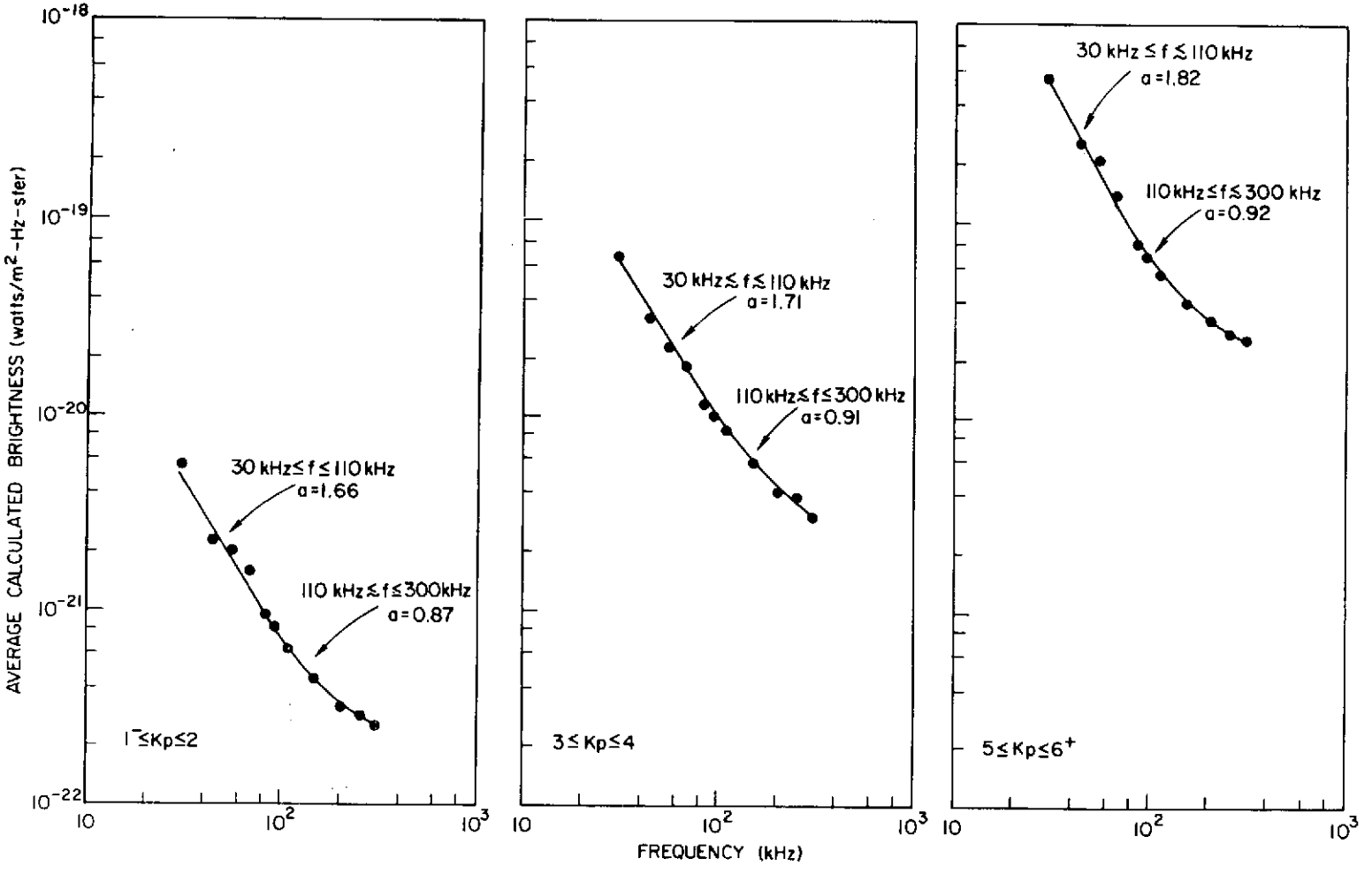

Figure 3.7 a-c THEORETICAL SPECTRUMS FOR THE GYRO-SYNCHROTRON RADIO NOISE GENERATED IN THE EARTH'S OUTER RADIATION BELT. In this figure (a) is the exponent in $I(f) \propto f^{-a}$.

($f < 40$ kHz) to gyro-synchrotron (44 kHz $< f <$ 92 kHz) but becomes, and remains, synchrotron for $f > 110$ kHz.) Hence, for 30 kHz $\leq f \leq$ 92 kHz, $|d[\log I_{av}(f)]/d[\log f]|$ is necessarily greater than for $f > 150$ kHz. (The value 0.9 obtained for $|d[\log I_{av}(f)]/d[\log f]|$ when 110 kHz $< f <$ 300 kHz agrees very well with the value calculated by Vesecky [1969], ~1.0, which he obtained for the synchrotron noise spectrum, 5 MHz $< f <$ 20 MHz, generated by electrons trapped above the earth's auroral zones.)

2. The spectrums in these figures are also characterized by only a slight increase in $|d[\log I_{av}(f)]/d[\log f]|$ as K_p increases from $1^- \leq K_p \leq 2$ to $5 < K_p < 6^+$, even though the average brightness for 30 kHz $< f <$ 300 kHz increases by almost two orders of magnitude. This feature of the data is to be expected, since the electron fluxes in the outer radiation belt are enhanced nearly uniformly over all energies during sustained geomagnetic activity or during the early recovery phase of large geomagnetic storms (Section II.B). (The slight increase in $|d[\log I_{av}(f)]/d[\log f]|$ is accounted for by more low energy electrons radiating appreciable power at low frequencies when K_p increases. That is, regions of higher magnetic flux density, and hence f_e, are exposed as the geomagnetic activity increases. Consequently, noise at low frequencies (f_ℓ) is augmented by radiation from electrons for which $f_\ell \approx s_{pk}(f_e)$. These particles do not radiate appreciable energy at f_ℓ for lower K_p values, since then $f_\ell = sf_e$ where $s > s_{pk}$; see Figure 1.6).

There exists one possibility (neglected to this point) which could affect the constancy of $|d[\log I_{av}(f)]/d[\log f]|$: deformation of the

dipole field geometry due to the compression of the magnetosphere by the solar wind. During severe disturbances, the dipole field lines are compressed at the subsolar point to $L \approx 6$ [Roederer, 1970]. This study, however, has considered the portion of the magnetosphere within the $L \approx 7.0$ shell and moderate geomagnetic disturbances resulting in $5 \leq K_p \leq 6^+$. It is therefore expected that the dipole field 'geometry', assumed for $L < 7$, is a valid representation of the earth's magnetic field. Thus, the slight increase in $\left|d[\log I_{av}(f)]/d[\log f]\right|$ for increasing K_p is felt to be a valid characteristic of the gyro-synchrotron radio noise spectrums.

CHAPTER IV

EXPERIMENTAL DATA

A. The Spacecraft

The IMP-6 (Explorer 43) was launched March 13, 1971 into a highly elliptical orbit defined by an eccentricity of 0.94, an initial perigee of 354 km, and an initial apogee of 206,000 km. (32 earth radii). The duration of this orbit was 4.18 days and it was given an inclination of 28.7 degrees.

The spacecraft is a sixteen-sided drum which is spin stabilized about the drum axis at a rate of 5.4 revolutions per minute. The spin axis is perpendicular to the ecliptic plane and points toward the southern ecliptic pole.

B. The Radio Astronomy Experiment

The GSFC radio astronomy experiment aboard the IMP-6 is composed of two total power, stepped frequency radiometers. Each receiver has thirty-two discrete frequency channels which are sampled over a 5.11 second interval. They are not, however, entirely similar. One covers the frequency range 30 kHz to 9900 kHz, has a bandwidth of 10 kHz, and a time constant of 6 milliseconds. The second has a frequency range from 30 kHz to 4900 kHz, a bandwidth of 3 kHz, and a time constant of 40 milliseconds.

Both receivers are connected to the same 300 foot dipole antenna, which is situated in the spacecraft spin plane. Due to this location and the satellite spin, any source of radio emission not located at

one of the ecliptic poles will have the maximum or minimum of the dipole antenna pattern swept past it, resulting in a modulation of the received signal. By analyzing the depth and phase of this modulation, the apparent size and location of the source can be determined [Brown, 1972].

To measure the temporal stability of the radio receivers, an automatic internal calibrating system was included in the radio astronomy package. The data returned from this system are used to compensate for time variations in the radio noise measurements due to short and long term drifts in receiver gains.

C. Initial Data Reduction

Dr. Larry Brown [1972] has analyzed the raw data from the tenth through the fortieth orbits of the IMP-6 to determine the steady underlying radiation observed by the spacecraft. His data reduction technique was specifically intended to reduce the contamination of the background radio spectrum by sporadic emissions from the sun, earth and the spacecraft itself. His results showed that three distinct forms of background radiation could be identified.

The first form of emission was that generated by galactic and extragalactic sources. This component, termed the radio background spectrum, was studied in detail by Brown [1972] for frequencies between 200 kHz and 1700 kHz.

The second form of radiation, found to emanate from the earth, was sporadic in nature and showed a peak in its brightness spectrum at about 250 kHz. This spectrum showed a decrease by two orders of magnitude within tens of kilohertz on either side of the maximum.

The third was a continuous, highly variable low frequency component, observed between 30 kHz and 110 kHz. Over this frequency range, the average spectrum for this radiation satisfied an expression of the form

$$I_m(f) = 3.3 \times 10^{-8} \quad f^{-2.8} \tag{4.1}$$

where

I_m = measured source brightness in watts m^{-2} Hz^{-1} $ster^{-1}$

f = frequency in Hz.

This result for I_m was obtained by assuming the source filled the IMP-6 dipole antenna pattern [Brown, personal communication]. Furthermore, the direction finding capabilities of the radio astronomy experiment showed this radio noise also to come from the earth. Spectrums representative of these three forms of background radiation are shown in Figure 4.1.

In this chapter we shall derive a number of important features of this third type of emission. These characteristics were determined by analyzing hourly plots of the background radiation observed by the IMP-6 during May through October 1971 (for which the author expresses his gratitude to Dr. Brown who supplied the data in this reduced form). However, the choice of plots used in this paper was restricted to times when the spacecraft was at least 194,000 km from the earth. This restriction was to provide an observer geometry similar to the one used in the theoretical analysis of the previous chapters. The amount of IMP-6 data left out is not large, as the spacecraft spends a large fraction of its time in each orbit at these distances from the earth.

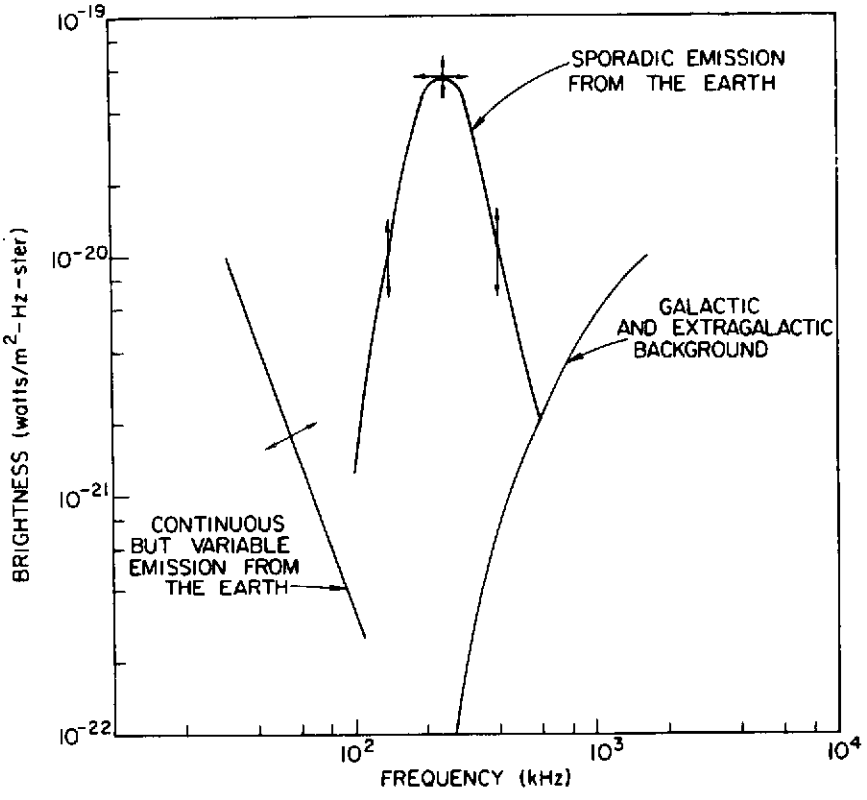

Figure 4.1 BACKGROUND RADIATION OBSERVED BY THE IMP-6 DURING APRIL-AUGUST 1971. (THESE DATA WERE CALCULATED FROM IMP-6 TEMPERATURE MEASUREMENTS ASSUMING THE GALACTIC SOURCES AND THE SOURCES LOCATED AT THE EARTH FILLED THE SPACECRAFT DIPOLE ANTENNA PATTERN.) [This figure was supplied by R. G. Stone, personal communication, 1972.]

(This can be proven by using Kepler's law of planetary motion [Bate et al., 1971] and the orbit described in Section IV.A).

D. Correlation between the Radio Noise Generated at the Earth and Geomagnetic Activity

The most salient feature evident in the data gathered by the IMP-6 was a two order of magnitude variation in the brightness for the radiation between 30 kHz and 110 kHz. To determine the cause for this variation in noise intensity, the IMP-6 data were correlated with geophysical and solar phenomena. It was found that an increase in the intensity of the radiation generally followed the onset of geomagnetic activity, and as the disturbance subsided the radiation returned to its unperturbed value. To put this observation into more precise terms, average spectrums for the noise as a function of K_p were calculated by subdividing the data into three groups. The first and second contained data for periods of sustained geomagnetic activity given by $1^- \leq K_p \leq 2$ and $3 \leq K_p \leq 4$ respectively. The third group comprise, data taken during the early recovery phase of the 16 - 18 May and 24 - 28 September 1971 geomagnetic storms. (The storm characteristics for the first case are shown in Figure 4.2). During this phase of the storms, the K_p index was bounded by $5 \leq K_p \leq 6^+$. (For the May storm, K_p reached values as high as 7 for a very short period of time. The radio noise data for this high value of K_p are, therefore, rather sparse and will be used only for argumentative purposes in the next chapter.) The resulting average brightness spectrums (as functions of K_p) are given in Figures 4.3 a-c.

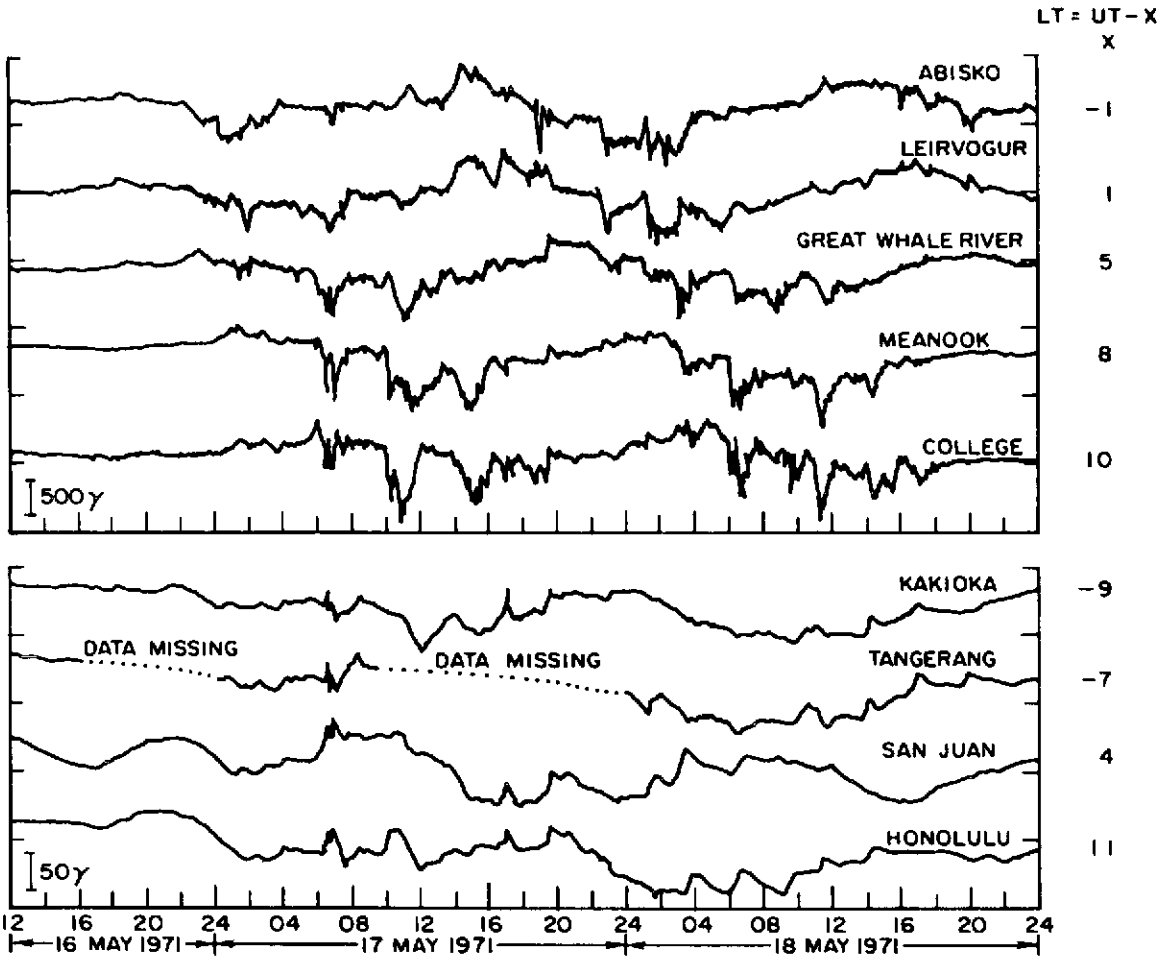

Figure 4.2 MORPHOLOGY OF THE GEOMAGNETIC STORM OCCURRING ON 16-18 MAY 1971 [From Solar Geophysical Data].

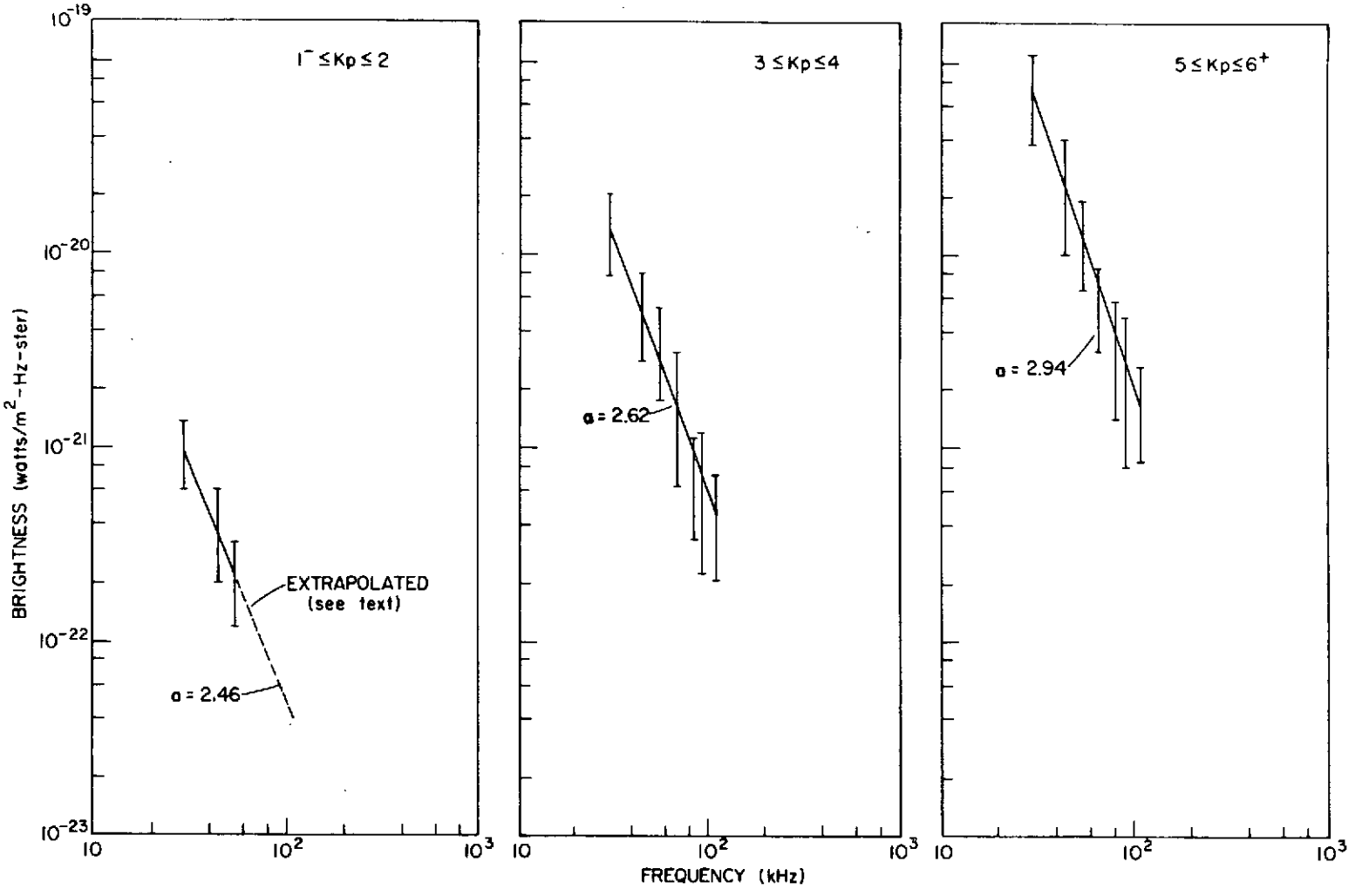

Figure 4.3 a-c BRIGHTNESS SPECTRUMS FOR THE SOURCE LOCATED AT THE EARTH. (THESE DATA WERE CALCULATED FROM IMP-6 TEMPERATURE MEASUREMENTS ASSUMING THE SOURCE FILLED THE SPACECRAFT DIPOLE ANTENNA PATTERN.) In this figure (a) is the exponent $I(f) \propto f^{-a}$.

It should be noted that in Figure 4.3a, the experimental data were extrapolated for $f > 55$ kHz. This was necessary as the radio noise power for frequencies above 55 kHz was of such small amplitude that the receivers were operating near the lower limit of their dynamic range. At these power levels, the linearity of the receivers is in question [Brown, personal communication]; therefore, the data for $f \rightarrow 55$ kHz were not used. Nevertheless, there were sufficient data for f = 30 kHz to 55 kHz to obtain the curve shown in Figure 4.3a.

These figures illustrate that the spectrums for each K_p range follow a law of the form

$$I_{av}(f) = I_c \, f^{-a} \qquad (4.2)$$

where (a) increases as the K_p value increases. If the entire set of orbital data covering April through August is averaged, the resulting spectrum is indeed given by Equation (4.1).

The error bars in these figures represent one standard deviation in the data about the average points plotted. Thus, even though the spectrums correlate with changes in K_p values, there still exists a large variation within each K_p range. These variations can be attributed to fluctuations of the trapped particle populations due to changes in the solar wind density and velocity as well as other geomagnetic related phenomena [Vette, 1971].

For the lower K_p range, the fluctuations in brightness due to these mechanisms should be a minimum. The error bars in Figure 4.3a, show however, that changes by a factor of 2.5 in the observed brightness are common. Even though this factor is less than those obtained for the

other two K_p ranges, it is still appreciable. Therefore, the spectrum for $1^- \leq K_p \leq 2$ will be reconsidered in Chapter V.

E. Determination of the Solid Angle Subtended by the Source Observed by the IMP-6

In the next chapter, we shall compare the average theoretical brightness of the magnetosphere $I_{av}(f)$, as calculated in Chapter III, to the average brightness of the earth (between 30 kHz and 110 kHz) measured on IMP-6. It must therefore be determined if the source observed by the spacecraft fills the satellite dipole antenna pattern, as assumed by Dr. Brown. This is necessary since the actual average brightness of the source $I_{act}(\text{source})$ is given by [Kraus, 1966]

$$I_{act}(\text{source}) = \frac{\Omega(f)}{\Omega_s(f,K_p)} I_m(\text{source}) \qquad \Omega_s(f,K_p) < \Omega_A(f) \qquad (4.3)$$

or

$$I_{act}(\text{source}) = I_m(\text{source}) \qquad \Omega_s(f,K_p) > \Omega_A(f) \qquad (4.4)$$

where

$I_{act}(\text{source})$ = actual measured brightness of the source obtained from IMP-6 experiment.

$I_m(\text{source})$ = average source brightness calculated by assuming the source fills the spacecraft antenna beam.

$\Omega_s(f,K_p)$ = the solid angle subtended by the source at the observation point for a frequency (f) and given K_p value.

$\Omega_A(f)$ = the solid angle of the spacecraft antenna pattern

This question was resolved by plotting the IMP-6 data for f = 30 kHz, 44 kHz, and 55 kHz (when $K_p \leq 3$) as a function of distance from the earth to the satellite. (A lower limit of ten earth radii was used in this analysis to avoid problems related to the spacecraft being within the earth's magnetoplasma.) The results are shown in Figures 4.4 a-c.

If the source subtends a solid angle less than that of the antenna pattern, the brightness should decrease by about an order of magnitude as the distance increases from ten to thirty-two earth radii (i.e., the R^{-2} decrease in the radio flux density should be observable). The results for f = 30 kHz (Figure 4.4a) are inconclusive due to the scattered nature of the IMP-6 data. (The fluctuation in these data will be discussed in the next chapter.) For f = 44 kHz and 55 kHz, however, the corresponding figures do show a decrease in the measured brightness by approximately one order of magnitude as the spacecraft distance from the earth increases by a factor of 3.2. Since the same results were also obtained at the higher frequencies, it must be concluded that the source actually does not fill the satellite antenna pattern when the spacecraft is located more than 6.4×10^4 km from earth. Thus, if a valid comparison between the IMP-6 data and the theoretical calculations is to be made, either set of data must be corrected.

Since the calculated data give the actual brightness of the earth's magnetosphere, while the IMP-6 data were calculated on an assumption, this latter set of data shall be corrected. The correction factor,

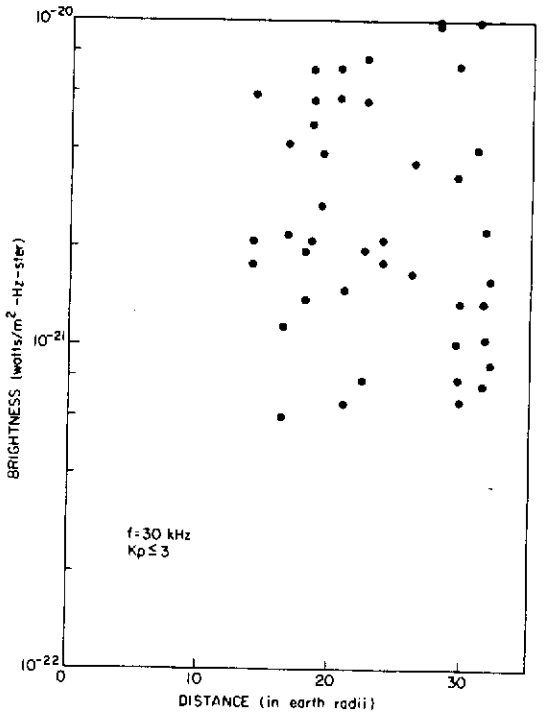

(a)

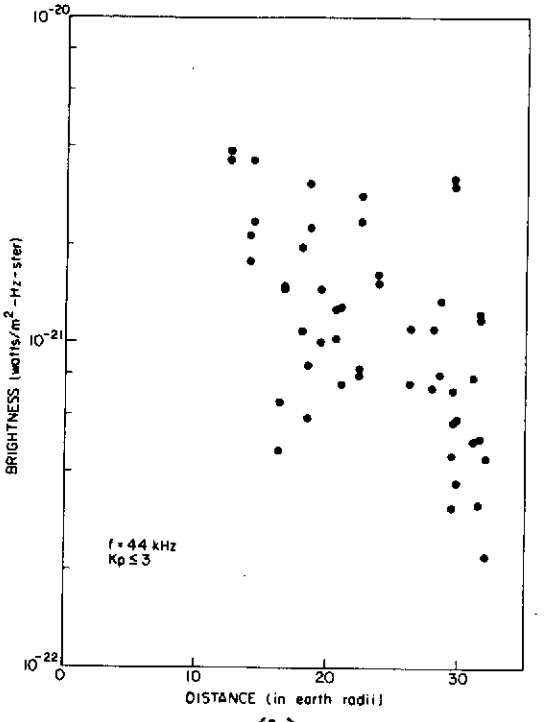

(b)

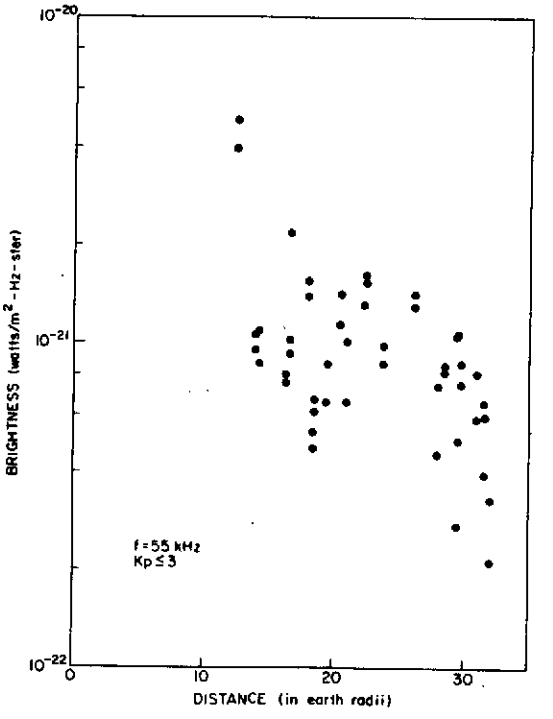

(c)

Figure 4.4 a-c SCATTER PLOT OF THE BRIGHTNESS OF THE EARTH (CALCULATED FROM IMP-6 DATA UNDER THE ASSUMPTION STATED IN THE CAPTION OF FIGURE 4.3) AS A FUNCTION OF THE SPACECRAFT GEOCENTRIC DISTANCE.

$\Omega_A(f)/\Omega_s(f,K_p)$ is obtained by assuming that the IMP-6 data are in fact a measure of the gyro-synchrotron radiation emanating from the earth's outer radiation belt (i.e., $\Omega_s(f,K_p)$ will be taken from Table 2). Then, if the corrected data agree with the theoretical calculations, the correction is justified and the recalculated spacecraft data will also give the actual brightness of the earth's magnetosphere. To this end, the theoretical results of Figures 3.7 a-c will be compared to Figures 4.5 a-c, which show the corrected IMP-6 data.

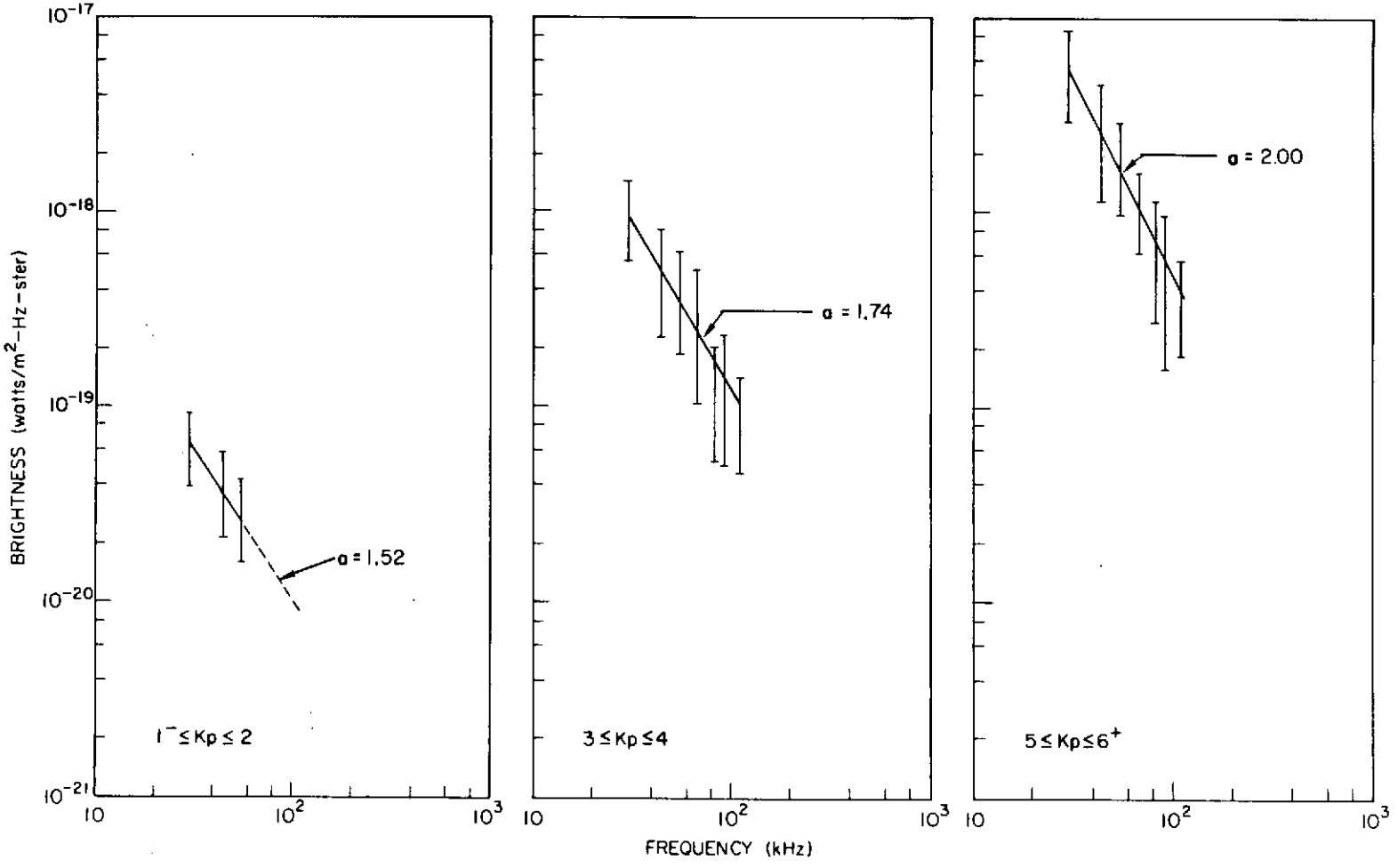

Figure 4.5 a-c CORRECTED IMP-6 BRIGHTNESS SPECTRUMS (COMPARE TO FIGURES 4.3 a-c) WHEN THE SOURCE SOLID ANGLE, $\Omega_s(f,K_p)$ IS ACCOUNTED FOR. In this figure (a) is the exponent in $I(f) \propto f^{-a}$.

CHAPTER V

COMPARISONS OF THEORETICAL AND EXPERIMENTAL RESULTS, FINAL CONCLUSIONS AND APPLICATIONS

A. Comparisons of Results

Equation (1.15) indicates that the brightness observed along ray paths passing through the earth's magnetosphere is a result of the radiation emanating from within this region and from galactic and extragalactic sources. The IMP-6 data (Figure 4.1) show, however, that the emission from the latter sources for 30 kHz $\leq$ f $\leq$ 110 kHz is orders of magnitude below that from the earth's environment; consequently, the galactic and extragalactic radio noise can be neglected in the discussion to follow.

There exists one problem pertaining to observer locations which must be considered before a comparison can be made between the theoretical results and the experimental data. In Chapter III the calculations were based on an observer situated in the geomagnetic equatorial plane. The IMP-6 orbit, however, is inclined nearly 30° to the earth's geographic equatorial plane. Consequently, the spacecraft's inclination angle (θ_{inc}) to the geomagnetic equatorial plane varies diurnally from $\approx 20^{\circ}$ to $\approx 40^{\circ}$.

Thorne [1963] conducted a detailed study on the variation expected in the synchrotron radiation from stars as a function of an observer's inclination angle to their magnetic equatorial planes. His results show that, for a magnetic field geometry identical to the one considered in the paper, the noise intensity is maximum in the equatorial plane ($\theta_{inc} = 0^{\circ}$) and decreases monotonically to a minimum value for $\theta_{inc} = 90^{\circ}$.

PRECEDING PAGE BLANK NOT FILMED

He found, furthermore, that $|I_{av}\theta_{inc} = 90^{o})/I_{av}(\theta_{inc} = 0^{o})|$ is a function of the exponent (q) in the $\sin^{q}\alpha$ pitch angle distribution he assumed for the star's stably trapped electrons. In particular, when θ_{inc} increased from zero to forty degrees, the noise intensity decreased by a factor of two for q = 6.0 but only by a factor of 1.1 for q = 2.5.

In this study, a $\sin^{2}\alpha$ pitch angle distribution was found appropriate for the particles trapped in the earth's magnetosphere (when $3 < L < 7$). Furthermore, $|dI_{av}(f)/d\theta_{inc}|$ is expected to be greater for synchrotron radiation than for cyclotron radiation. (For cyclotron emission the particles radiate nearly isotropically, while for synchrotron emission they radiate predominantly along the normals to the magnetic field lines, see Sections I.D and III.G.) Therefore, Thorne's factor of 1.1 can be considered an upper bound for the discrepancy expected between the theoretical results and the experimental data due to the different observer locations. Since this factor is insignificant, a direct comparison of Figures 3.7 a-c and 4.5 a-c (which are redrawn in Figure 5.1 for convenience) can be made. A summary and discussion of the results obtained from this analysis are given below.

1. For 30 kHz ≤ f ≤ 110 kHz the slopes for the theoretical noise spectrums in Figures 3.7 a-c were averaged for the three K_p ranges, and the value $|d[\log I_{av}(f)]/d[\log f]|^{theo}_{av}$ was then compared to a similar average obtained for the corrected IMP-6 spectrums in Figures 4.5 a-c. The result obtained was

$$|d[\log I_{av}(f)]/d[\log f]|^{IMP-6}_{av} = (1.05)\ |d[\log I_{av}(f)]/d[\log f]\ |^{theo}_{av}$$

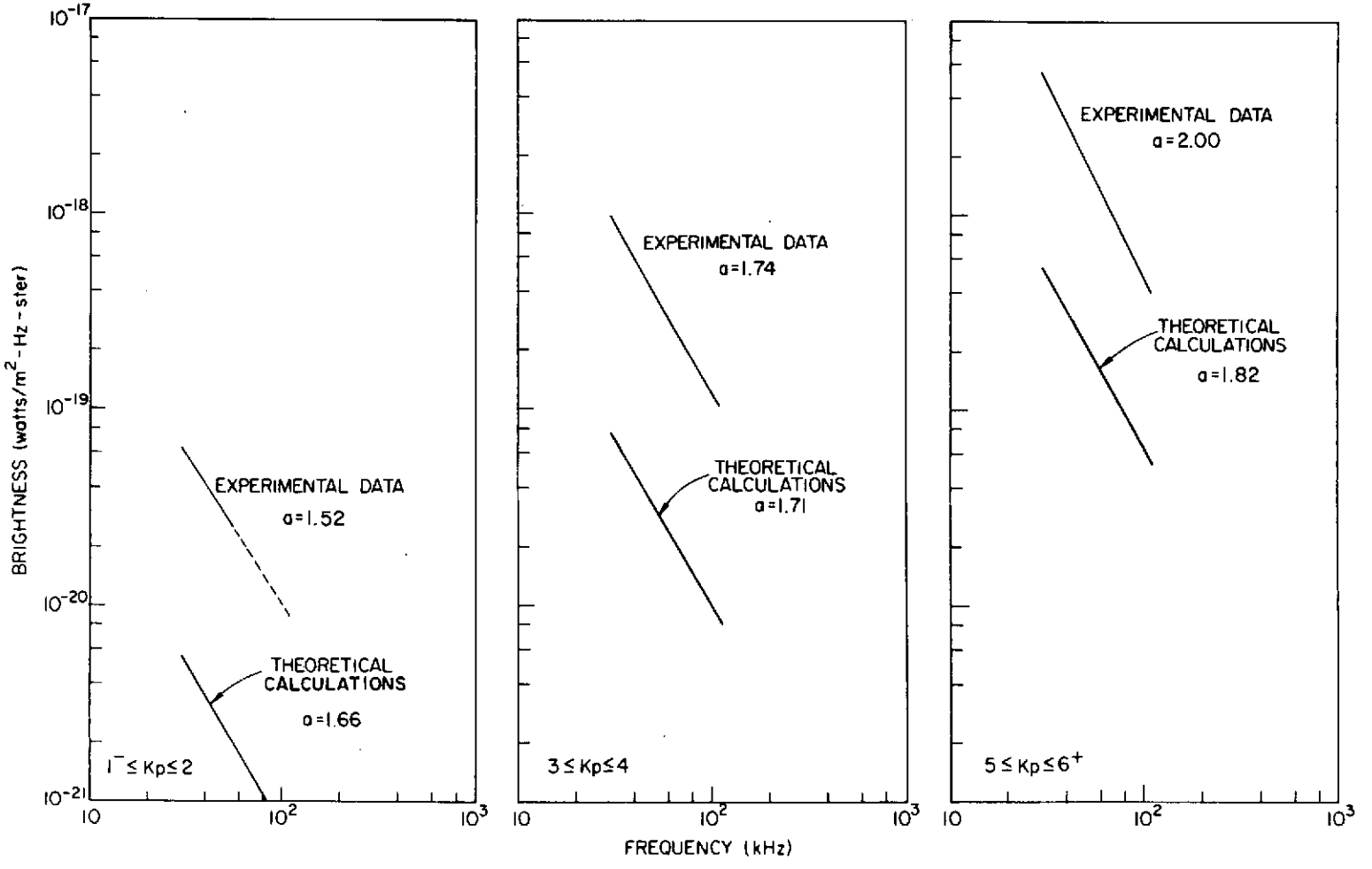

Figure 5.1 a-c AVERAGE THEORETICAL AND EXPERIMENTAL SPECTRUMS FOR THE RADIO NOISE EMANATING FROM THE EARTH'S OUTER RADIATION BELT. In this figure (a) is the exponent in $I(f) \propto f^{-a}$.

Furthermore, when the slopes for each K_p range were compared separately, the largest discrepancy occurred for $5 \leq K_p \leq 6^+$ where

$$\left|d[\log I_{av}(f)]/d[\log f]\right|_{av}^{IMP-6} = (1.09)\ \left|d[\log I_{av}(f)]/d[\log f]\right|_{av}^{theo}$$

2. Both sets of data show a slight, but discernable, increase in $\left|d[\log I_{av}(f)]/d[\log f]\right|$ as K_p increases.

3. The increase in the magnitude of $I_{av}(f)$ in the IMP-6 data (which was correlated with increases in K_p) also exists in the theoretical calculations. In addition, $\left|dI_{av}(f)/dK_p\right|^{IMP-6}$ is within 5% of $\left|dI_{av}(f)/dK_p\right|^{theo}$ for each K_p range. Thus, the average enhancement of the stably trapped electrons due to geomagnetic disturbances satisfactorily accounts for the increase in the radio noise observed by the IMP-6 during such activity.

4. In the worst case, $I_{av}(f,K_p)_{IMP-6} = (15.0)\ I_{av}(f,K_p)_{theo}$. This constant discrepancy, however, is not felt to be critical for the following reasons.

i) Throughout this paper, approximations, worst case conditions, and assumptions have been used to simplify the analysis which led to an underestimation of $I_{av}(f)$. Individually, each of these simplifications results is no more than 10% decreases in $I_{av}(f)$. Their combined effect, however, results in a total reduction of $I_{av}(f)$ by approximately a factor of two (due to the number of simplifications made).

ii) In Chapter III, calculations for the ordinary mode were not presented since the power radiated into it is generally less than or equal to that radiated into the extraordinary mode. However, calculations for free-space showed that the power radiated into the ordinary mode is comparable to that radiated into the extraordinary mode

when $|\theta| \geq |\alpha - 10^{o}|$. Since the emission region is nearly free-space for 30 kHz $\leq$ f $\leq$ 110 kHz, the power radiated into the ordinary mode will increase the values calculated for $I_{av}(f,K_p)$ by about 1.5.

iii) In this study, superthermal electrons in the pseudo-trapping regions [Vette, 1971] have been entirely neglected due to the lack of sufficient data on the particle distributions throughout this segment of the magnetosphere. However, measurements have been made for the fluxes in the portion of the pseudo-trapping region given by 8 $\leq$ L $\leq$ 10 in the morning magnetosphere [Hess, 1968; Williams and Palmer, 1964]. The data show that at high geomagnetic latitudes (and hence regions of high magnetic flux density) the integrated electron fluxes in this region (for E $\geq$ 40 kev and E $\geq$ 280 kev) are two orders of magnitude greater than the fluxes in the corresponding segment of the nighttime magnetosphere. Thus, fluxes in the former region are comparable to those which exist at much lower L shells in the latter (i.e., 6 < L < 7). The pseudo-trapping region in the morning magnetosphere should therefore affect the results of this study in two ways. First, the radiation from electrons in this region will increase the values calculated for $I_{av}(f,K_p)$. Second, the symmetry of the emission region will be destroyed (see Section III.G.2) since a larger segment of the morning magnetosphere will contribute detectable radiation, and the electron fluxes in 8 $\leq$ L < 10 will make its overall (spatially integrated) brightness considerably greater than that of the nighttime magnetosphere. Due to lack of data, however, quantitative values for these effects can not be calculated.

From the above discussion, it is evident that the calculations for

$I_{av}(f,K_p)$ can be below the actual brightness of the magnetosphere by over a factor of three. Hence, the noise detected by the IMP-6 and the intensity of the radiation emanating from the earth's magnetosphere differ not by a factor of 15, but more likely by a factor of less than five, i.e., a discrepancy of at most 7 dB in the noise power.

B Summary and Conclusions

In this study the problem of detecting gyro-synchrotron radio noise, from superthermal electrons trapped in the earth's magnetosphere, has been investigated for the frequency range 30 kHz to 300 kHz. The energy radiated by these electrons and propagated to an observer in the interplanetary medium was calculated using the equation of radiative transfer. To solve this equation, models for the thermal and superthermal electron densities as a function of geomagnetic activity were derived from in situ and indirect measurements of these particle populations.

The analysis shows that appreciable radio noise in the LF range is emitted by electrons in the earth's outer radiation belt. The inner belt, however, does not contribute power at these frequencies since it is located in the plasmasphere, a region of high thermal electron density which inhibits radiation at these low frequencies. The intensity of the radio noise from the outer belt was found to be positively correlated with K_p. This correlation is due to the enhancement of stably trapped electrons during periods of sustained geomagnetic activity. For a frequency f in Hz (30 kHz $\leq$ f $\leq$ 150 kHz), the average brightness $I_{av}(f)$ is given by (see Figure 5.1)

$$I_{av}(f) = M f^{-a} \qquad \text{watts m}^{-2}\ \text{Hz}^{-1}\ \text{ster}^{-1} \qquad (5.1)$$

where both M and (a) vary with K_p as follows:

$$\begin{cases} 1^- \leq K_p \leq 2 & M = 1.51 \times 10^{-13} \quad a = 1.66 \\ 3 \leq K_p \leq 4 & M = 3.16 \times 10^{-12} \quad a = 1.71 \\ 5 \leq K_p \leq 6^+ & M = 7.41 \times 10^{-11} \quad a = 1.82 \end{cases}$$

The theoretical results were compared to data obtained from the GSFC experiment aboard the IMP-6 (as shown in Figure 5.1 and discussed in the preceding section). The models were found to accurately predict the spectral shape, temporal variations and magnitude of the radio noise observed by the radio astronomy experiment. This author, therefore, concludes that the electrons, which are injected and trapped by natural process in the earth's outer radiation belt, generate detectable gyro-synchrotron radio noise in the LF range. The intensity of this noise is a function of geomagnetic activity, increasing as K_p increases. Furthermore, this noise is observed only in the LF range since for $f \geq 2$ MHz its intensity is below the cosmic noise level (compare Figure 4.1 with Figure 5.1).

C. Applications

The gyro-synchrotron radiation at 110 kHz $\leq f \leq$ 300 kHz was shown to come from high energy electrons, while the radiation at low frequencies, 50 kHz $\leq f \leq$ 53 kHz, results from low energy electrons (Section III.F). During the main phase of a geomagnetic storm, the low energy electron fluxes, 40 kev $\leq E \leq$ 200 kev, are enhanced over quiet time

values, while the high energy electron fluxes, E > 800 kev, are depleted (Section II.B). Consequently, during this phase of a geomagnetic disturbance the gyro-synchrotron noise should have a spectrum whose slope is greater than those obtained in Figures 4.5 a-c. This is the case, as illustrated in Figure 5.2, which shows IMP-6 data taken during the main phase of the 16 - 18 May 1971 geomagnetic storm.

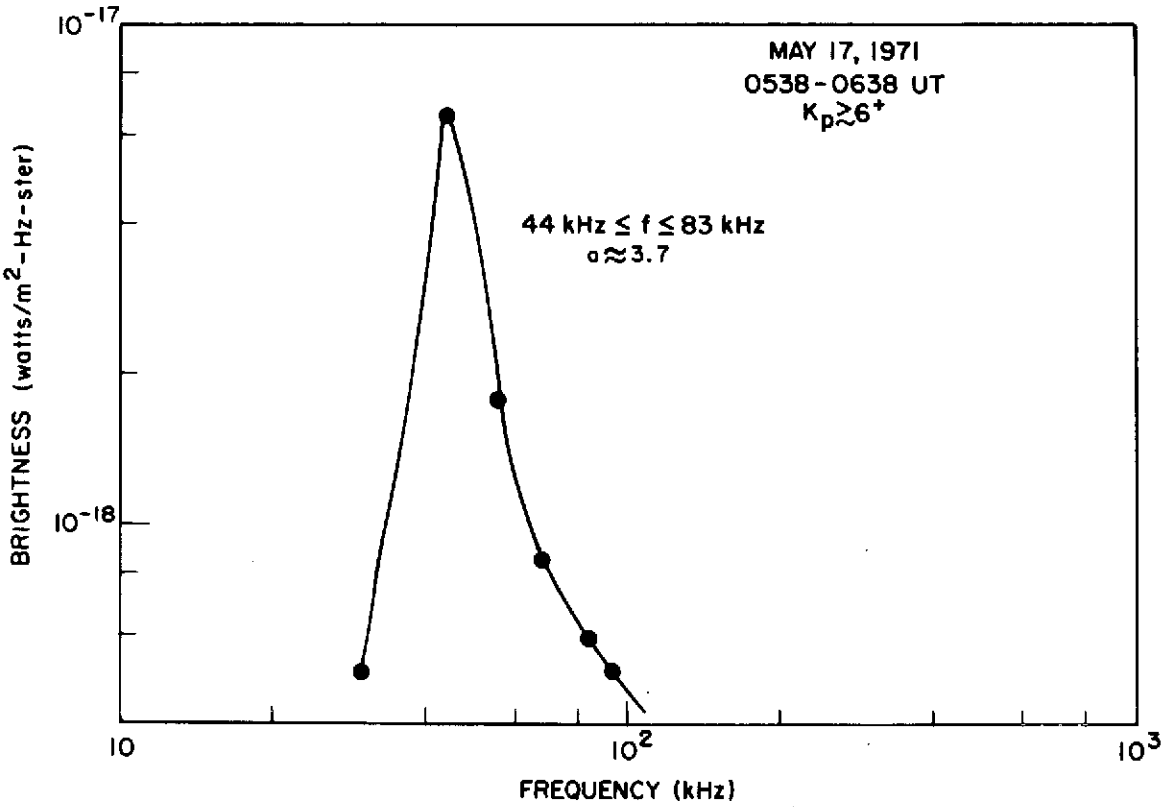

Figure 5.2 CORRECT IMP-6 BRIGHTNESS SPECTRUM FOR THE NOISE EMANATING FROM THE EARTH'S OUTER RADIATION BELT DURING THE MAIN PHASE OF THE 16-18 MAY 1971 GEOMAGNETIC STORM. In this figure (a) is the exponent in $I(f) \propto f^{-a}$.

Based on the discussion of the last paragraph, which summarizes an important result of this study, it is evident that the IMP-6 noise data can be used to obtain the average (spatially integrated) flux spectrum of the energetic electrons trapped in the earth's outer radiation belt. A study of this nature would be conducted by first averaging noise data over long periods of time, then reversing the analysis presented in this paper to obtain electron flux spectrums similar to those given in Figures 2.1 and 2.2b. Furthermore, this type of study would allow the average temporal variations in the electron fluxes to be determined. For example, temporal variations in the radio noise data are evident in Figures 4.3a and 4.4a. During geomagnetically quiet days, these figures show large fluctuations in the low frequency radio noise, f = 30 kHz, compared to the variations in the high frequency noise. This difference between the magnitude of the fluctuations is expected, as satellite measurements of the electron fluxes show consistent, large temporal variations in the low energy electron fluxes in contrast to stable, non-varying high energy fluxes [Freeman, 1964].

A second application of the results of this study is the use of the gyro-synchrotron radio noise to monitor the interplanetary solar wind density in the vicinity of the earth. This type of study is possible, since noise generated by this process should extend to frequencies below 15 kHz, and the interplanetary electron density at 1.0 AU is an average of ≈ 5 electrons-cm^{-3} (i.e., $f_p \approx 20.1$ kHz) [Brandt, 1970]. Thus, the medium will inhibit the propagation of the low frequency gyro-synchrotron radiation; the cutoff frequency of the noise will then determine f_p, from which the electron density can be

calculated. (In this calculation, the observer must be located near the earth in order to detect the radio noise. Therefore, the effects of the interplanetary plasma on the receiving antenna must be considered. Nevertheless, appropriate calculations should give an acceptable estimate of the electron density.)

The above line of reasoning is supported empirically by the radio noise data, given in Figure 5.2, which show an unexpected roll-over in the spectrum at $f_{rl} \approx 47$ kHz. For the day in which these data were taken (17 May 1971), the interplanetary electron density showed the following temporal variation (as measured by experiments aboard the IMP-6). Early on the 17th, the density was 10 electrons-cm^{-3}, which increased to 25 electrons-cm^{-3} near noon, and subsequently returned to $\approx$ 10 electrons-cm^{-3} later in the day. Furthermore, for the period of time during which the data of Figure 5.2 were taken (0538-0638 UT), the electron density was $\approx$ 18 electrons-cm^{-3} [Dr. S. J. Bame, personal communication, 1973], resulting in $f_p \approx 38$ kHz. Consequently, as $f_{rl} \approx f_p$, the decrease in noise intensity for $f \leq 47$ kHz was probably due to propagation limitations (and, in this case, effects on the spacecraft antenna) created by the interplanetary plasma. (This application, and the one given below, can be implemented independent of the mechanism generating the noise detected by the IMP-6 experiments.)

A final application involves the ray paths calculated in Section II.H. These paths, for 30 kHz $\leq f \leq$ 300 kHz, do not penetrate the plasmasphere. Thus, through an occultation experiment, two satellites could be used to determine the location of the plasmapause. In such an experiment, one spacecraft transmits signals at $f \approx 30$ kHz to the IMP-6

spacecraft. Then by choosing an orbit for the former spacecraft which allows it to be intermittently occulted from the IMP-6 by the earth's magnetosphere, the positions of the spacecrafts at occultation and ray path geometry can be used to determine the location of the plasmapause.

The details of these applications have not been presented, as they would constitute another entire study. The point is, the gyro-synchrotron emission mechanism does satisfactorily account for the radio noise detected by the IMP-6 in the frequency range kHz $\leq f \leq$ 110 kHz. Furthermore, observations of this radiation and the results obtained in this paper are useful in the study of the electrons trapped in the earth's outer radiation belt, as well as in the study of other geophysical phenomena.

REFERENCES

Angerami, J. J., and D. L. Carpenter, Whistler Studies of the Plasmapause in the Magnetosphere, 2, Electron Density and Total Tube Electron Content Near the Knee in Magnetospheric Ionization, J. Geophy. Res., 71, 711, 1966.

Bate, R. B., D. D. Mueller, and J. E. White, Fundamentals of Astrodynamics, Dover Publications, New York, 454, 1971.

Bauer, S. J., Constitution of the Atmosphere at Magnetospheric Levels, Radio Science, 680, 597, 1964.

Bekefi, G., Radiation Processes in Plasmas, Wiley, New York, 377, 1966.

Brandt, J. C., Introduction to the Solar Wind, W.H. Freeman and Company, San Francisco, 199, 1970.

Brown, L. W., The Galactic Radio Spectrum Between 130 kHz and 2600 kHz, Laboratory for Extraterrestrial Physics, Goddard Space Flight Center, Greenbelt, Maryland, to be published.

Budden, K. G., Radio Waves in the Ionosphere, 542, Cambridge University Press, Cambridge, 1961.

Carpenter, D. L., Whistler Studies of the Plasmapause in the Magnetosphere, 1, Temporal Variations in the Position of the Knee and Some Evidence on Plasma Motions Near the Knee, J. Geophys. Res., 71, 693, 1966.

Carpenter, D. L., Whistler Evidence of the Dynamic Behavior of the Duskside Bulge in the Plasmasphere, J. Geophys. Res., 75, 3837, 1970.

Carpenter, D. L., OGO 2 and 4 VLF Observations of the Asymmetric Plasmapause Near the Time of SAR Arc Events, J. Geophys. Res., 76, 3644, 1971.

Carpenter, D. L., C. G. Park, J. F. Arens, and D. J. Williams, Brief Reports, Position of the Plasmapause During a Stormtime Increase in Trapped Energetic ($E > 280$ kev) Electrons, J. Geophys. Res., 76, 4669, 1971.

Chang, D. B., and L. Davis Jr., Synchrotron Radiation as the Source of Jupiter's Polarized Decimeter Radiation, Astrophys. J., 136, 567, 1962.

Chapman, S., The Earth and Its Environment, Proc. IRE, 47, 137, 1959.

Chappell, C. R., Recent Satellite Measurements of the Morphology and Dynamics of the Plasmasphere, Reviews of Geophysics, 10, 4, p. 951, 1972.

Chappell, C. R., K. K. Harris, and G. W. Sharp, A Study of the Influence of Magnetic Activity on the Location of the Plasmapause as Measured by OGO 5, J. Geophys. Res., 75, 50, 1970.

Craven, J. D., Temporal Variations of Electron Intensities at Low Altitudes in the Outer Radiation Zone as Observed With Satellite Injun 3, J. Geophys. Res., 71, 5643, 1966.

Dyce, R. B., and M. P. Nakada, On the Possibility of Detecting Synchrotron Radiation From Electrons in the Van Allen Belts, J. Geophys. Res., 64, 1163, 1959.

Eidman, V. I., The Radiation From an Electron Moving in a Magnetoactive Plasma, Sov. Phys. JETP, 34, 91, 1958.

Frank, L. A., Inward Radial Diffusion of Electrons of Greater Than 1.6 Million Electron Volts in the Outer Radiation Zone, J. Geophys. Res., 70, 3533, 1965.

Frank, L. A., Initial Observations of Low-Energy Electrons in the Earth's Magnetosphere With OGO 3, J. Geophys. Res., 72, 185, 1967.

Frank, L. A., J. A. Van Allen, and H. K. Hills, A Study of Charged Particles in the Earth's Outer Radiation Zone With Explorer 14, J. Geophys. Res., 69, 2171, 1964.

Freeman, J. W. Jr., The Morphology of the Electron Distribution in the Outer Radiation Zone and Near the Magnetospheric Boundary as Observed by Explorer 12, J. Geophys. Res., 69, 1691, 1964.

Fung, P. C. W., Excitation of Cyclotron Radiation in the Forward Subliminous Mode and Its Application to Jupiter's Decametric Emissions, Planet Space Science, 14, 469, 1966.

Ginzburg, V. L., Propagation of Electromagnetic Waves in Plasma, 822, Gordon and Breach, New York, 1961.

Helliwell, R. A., The Structure of the Plasmasphere on the Basis of Indirect Measurements, Solar-Terrestrial Physics: Part IV, 165, 1970.

Hess, W. N., The Radiation Belt and Magnetosphere, 548, Blaisdell, Waltham, 1968.

Hower, G. L., and A. M. Peterson, Synchrotron Radiation From Auroral Electrons, J. Geophys. Res., 69, 3995, 1964.

Katz, L., "Electron and Proton Observations", in Radiation Trapped in the Earth's Magnetic Field, ed. by Billy M. McCormac, D. Reidel, Dordrecht, Holland, 1966.

Kelso, J. M., Radio Ray Propagation in the Ionosphere, 408, McGraw-Hill, New York, 1964.

Kraus, J. D., Radio Astronomy, 481, McGraw-Hill, New York, 1966.

McIlwain, C. E., Magnetic Coordinates, in Radiation Trapped in the Earth's Magnetic Field, ed. by Billy M. McCormac, D. Reidel, Dardrecht, Holland, 1966.

McKenzie, J. F., Radiation Losses From a Test Particle in a Plasma, Phys. Fluids, 10, 2680, 1967.

Melrose, D. B., The Emission and Absorption of Waves by Charged Particles in Magnetized Plasmas, Astrophysics and Space Science 2, 171-235, D. Reidel, Dordrecht, Holland, 1968.

Owens, H. D., and L. A. Frank, Electron Omnidirectional Contours in the Earth's Outer Radiation Zone at the Magnetic Equator, J. Geophys. Res., 73, 199, 1968.

Pacholczy, A. G., Radio Astrophysics, 269, W. H. Freeman and Company, San Francisco, California 1970.

Panofsky, W. K. H., and M. Phillips, Classical Electricity and Magnetism, 2nd ed., Addison-Wesley, Reading, Mass., 1962.

Park, C. G., Whistler Observations of the Interchange of Ionization between the Ionosphere and the Protonosphere, J. Geophys. Res., 75, 4249, 1970.

Peterson, A. M., and G. L. Hower, "Theoretical Model of Synchrotron Radiation and Comparison With Observations", in Radiation Trapped in the Earth's Magnetic Field, ed. by Billy M. McCormac, D. Reidel, Dordrecht, Holland, 1966.

Pfitzer, K., S. Kane, and J. R. Winckler, The Spectra and Intensity of Electrons in the Radiation Belts, Space Res., 6, 702, 1966.

Ratcliffe, J. A., The Magneto-Ionic Theory and Its Applications to the Ionosphere, A Monograph, 206, Cambridge University Press, Cambridge, 1962.

Razin, V. A., "Contribution to the Theory of Spectra of Radio Emission From Discrete Sources Below 30 Mc/s", News of Higher Education Institutions, Ministry of Higher Education (USSR), Radio Physics Series 3, 73, 1960.

Roederer, J. G., On the Adiabatic Motion of Energetic Particles in a Model Magnetosphere, J. Geophys. Res., 72, 981, 1967.

Roederer, J. G., Dynamics of Geomagnetically Trapped Radiation, 116, Springer-Verlag, New York, 1970.

Rose, D. C., The Alouette Satellite Results, in Radiation Trapped in the Earth's Magnetic Field, ed. by Billy M. McCormac, D. Reidel, Dordrecht, Holland, 1966.

Rossi, B., and S. Olbert, Introduction to the Physics of Space, 454, McGraw-Hill, New York, 1970.

Stix, T. H., The Theory of Plasma Waves, 283, McGraw-Hill, New York, 1962.

Tanenbaum, B. S., Plasma Physics, 361, McGraw-Hill, New York, 1967.

Taylor, H. A., Jr., H. C. Brinton, and M. W. Pharo III, Contraction of the Plasmasphere During Geomagnetically Disturbed Periods, J. Geophys. Res., 73, 961, 1968.

Thorne, K. S., The Theory of Synchrotron Radiation From Stars With Dipole Magnetic Fields, Astrophys. J. Suppl., 8, 1, 1963.

Trulsen, J., Cyclotron Radiation in Hot Magnetoplasmas, J. Plasma Phys., 6, 367, 1971.

Trulsen, J., and J. A. Fejer, Radiation From a Charged Particle in a Magnetoplasma, J. Plasma Phys., 4, 825, 1970.

Vesecky, J. F., Radio Frequency Synchrotron Radiation From Electrons Trapped in the Earth's Magnetic Field, Technical Report No. 3606-2, Stanford Electronics Laboratories, 1967.

Vesecky, J. F., Radio-Frequency Synchrotron Radiation From Trapped Electrons Above the Auroral Zones, Planet. Space Sci., 17, 389, 1969.

Vette, J. I., Trapped Radiation Population, Section 4, Page 1, Trapped Radiation Handbook, General Electric Company, Santa Barbara, 1971.

Vette, J. I., A. B. Lucero, and J. A. Wright, Models of the Trapped Radiation Environment, Volume II: Inner and Outer Zone Electrons, NASA-SP-3024, 1966.

Vette, J. I., A. B. Lucero, and J. A. Wright, Models of the Trapped Radiation Environment, Volume III: Electrons at Synchronous Altitudes, NASA SP-3024, 1967.

West, H. I., Jr., J. H. Wujeck, J. H. McQuaid, N. C. Jenson, R. G. D'Arcy, Jr., R. W. Hill, and R. M. Bogdanowicz, The LRL Electron and Proton Spectrometer on NASA's Orbiting Geophysical Observatory V(E) (Instrumentation and Calibration) University of California, Lawrence Radiation Laboratory Report,UCRL-50572, June 2, 1969b.

West, H. I., Jr., R. M. Buck, and J. R. Walton, Electron Spectra in the Slot and the Outer Radiation Belt, Trans. Amer. Geophys. Union, 51, 806, 1970.

West, H. I., Jr., R. M. Buck, and J. R. Walton, A Brief Survey of Electron Pitch Angle Distributions Throughout the Magnetosphere as Observed by OGO-5, Lawrence Livermore Laboratory, University of California, 1972, to be published.

Williams, D. J., "Outer Zone Electrons, in Radiation Trapped in the Earth's Magnetic Field, ed. by Billy M. McCormac, D. Reidel, Dordrecht, Holland, 1966.

Williams, D. J., and W. F. Palmer, Distortions in the Radiation Cavity as Measured by an 1100-Kilometer Polar Orbiting Satellite, J. Geophys. Res., 70, 557, 1965.

Williams, D. J., and A. M. Smith, Daytime Trapped Electron Intensities at High Latitudes at 1100 Kilometers, J. Geophys. Res., 70, 13, 541, 1965.

Yeh, K. C., and C. H. Liu, Propagation and Application of Waves in the Ionosphere, Rev. Geophys. Space Phys., 10, 631, 1972.

Zheleznyakov, V. V., A Coherent Synchrotron Mechanism for Radio Emission From Cosmic Sources, Sov. Astron.-AJ, English Translation, 11, 33, 1967.